2010-08-29

Magnetic Resonance Imaging of Neural and Pulmonary Vascular Function

Ronn P. Walvick
Worcester Polytechnic Institute

MAGNETIC RESONANCE IMAGING OF NEURAL AND PULMONARY VASCULAR FUNCTION

A Dissertation Presented

By

Ronn P. Walvick

Submitted to the Faculty of the
University of Massachusetts Graduate School of Biomedical Sciences, Worcester and
Worcester Polytechnic Institute
in partial fulfillment of the requirements for the degree of

DOCTOR OF PHILOSOPHY

SEPTEMBER, 1 2010

BIOMEDICAL ENGINEERING AND MEDICAL PHYSICS

MAGNETIC RESONANCE IMAGING OF NEURAL AND PULMONARY VASCULAR FUNCTION

A Dissertation Presented
By

Ronn P. Walvick

The signatures of the Dissertation Defense Committee signifies
completion and approval as to style and content of the Dissertation

Mitchell S. Albert, Ph.D., Thesis Advisor

Glenn R. Gaudette, Ph.D., Member of Committee

Mathew J. Gounis, Ph.D., Member of Committee

Alexei A. Bogdanov, Ph.D., Member of Committee

Karl G. Helmer, Ph.D., Member of Committee

The signature of the Chair of the Committee signifies that the written dissertation meets
the requirements of the Dissertation Committee

Christopher H. Sotak, Ph.D., Chair of Committee

The signature of the Dean of the Graduate School of Biomedical Sciences signifies
that the student has met all graduation requirements of the school.

Anthony Carruthers, Ph.D.,
Dean of the Graduate School of Biomedical Sciences

Biomedical Engineering and Medical Physics

September 1, 2010

Dedicated to my wife Ellen and my daughter Shelby

Acknowledgements

I would like to thank both Bernt Bratane and Austin Reno for their help and collaboration on these projects. Bernt and I collaborated on the experimental work involving cerebral ischemia. Bernt, I have been impressed by your skills as a scientist and I hope we can renew our collaborations in the future. Austin was instrumental in helping to optimize the disease models used in the pulmonary projects. Austin, you are going to make a great doctor and I wish you all the best.

My development as an engineer and scientist was greatly facilitated by my advisor, Mitch Albert, and the other Radiology and Biomedical Engineering faculty at UMASS and WPI. Mitch, I appreciate the opportunities you gave me to advance my knowledge of MRI and develop professionally. I want to thank both Dr. Mathew Gounis and Dr. Alexei Bogdanov who were very kind to share their skills, knowledge, and resources with me. You have both went above and beyond in your support of my success and professional development. Also, I would like to acknowledge Dr. Karl Helmer who was the first person I met with when I interviewed for admission to WPI. It was discussions with him that initially got me excited about MRI research. I am thankful for the support and advice of Dr. Michael King who has been a mentor and a friend. I want to thank Dr. Glenn Gaudette for helping me organize my defense and helping me through the dissertation writing process. I would also like to thank Dr. Marc Fisher for introducing me to the fascinating world of experimental stroke research and for his guidance in conducting the cerebral ischemia experimentation. Finally, I would like to

thank Dr. Christopher Sotak for all his valuable help and guidance. Chris, your knowledge of MRI physics is unparalleled and it was an honor to be your student.

I would also like to acknowledge my friends and colleagues at UMASS and WPI. I would like to thank Jaime, James, Paul, Ken, Manik, Dave, Joyoni, Mike, and Salman for the conversations, company, and assistance. I would also like to thank Dr. Katie Bush and Dr. Jenna Balestrini for their help and guidance in navigating the first years of the program.

Submission of my dissertation represents the cumulative effort of my family. My wife Ellen has been wonderfully supportive and understanding to an extent that was unbelievable. I love you so much. I certainly know that I would not be at this point in my life without my parents, Helene and Allan Walvick who stood behind me during bad times and who celebrated with me during good times. I want to also thank Marissa and Steve Cofsky, my sister and brother in-law, for their love and support. Finally, I want to tell my daughter Shelby that she will always be the light of my life and I am very proud of her.

Abstract

Magnetic resonance imaging (MRI) has emerged as the imaging modality of choice in a wide variety experimental and clinical applications. In this dissertation, I will describe novel MRI techniques for the characterization of neural and pulmonary vascular function in preclinical models of disease.

In the first part of this dissertation, experimental results will be presented comparing the identification of ischemic lesions in experimental stroke using dynamic susceptibility contrast (DSC) and a well validated arterial spin labeling (ASL). We show that DSC measurements of an index of cerebral blood flow are sensitive to ischemia, treatment, and stroke subregions. Further, we derived a threshold of cerebral blood flow for ischemia as measured by DSC. Finally, we show that ischemic lesion volumes as defined by DSC are comparable to those defined by ASL.

In the second part of this dissertation, a methodology of visualizing clots in experimental animal models of stroke is presented. Clots were rendered visible by MRI through the addition of a gadolinium based contrast agent during formation. Modified clots were used to induce an experimental embolic middle cerebral artery occlusion. Clots in the cerebral vasculature were visualized *in vivo* using MRI. Further, the efficacy of recombinant tissue plasminogen activator (r-tPA) and the combination of r-tPA and recombinant annexin-2 (rA2) was characterized by clot visualization during lysis.

In the third part of this dissertation, we present results of the application of hyperpolarized helium (HP-He) in the characterization of new model of experimental

pulmonary ischemia. The longitudinal relaxation time of HP-He is sensitive to the presence of paramagnetic oxygen. During ischemia, oxygen exchange from the airspaces of the lungs to the capillaries is hindered resulting in increased alveolar oxygen content which resulted in the shortening of the HP-He longitudinal relaxation time. Results of measurements of the HP-He relaxation time in both normal and ischemic animals are presented.

In the final part of this dissertation, I will present results of a new method to measure pulmonary blood volume (PBV) using proton based MRI. A T_1 weighted, inversion recovery spin echo sequence with cardiac and respiratory gating was developed to measure the changes in signal intensity of lung parenchyma before and after the injection of a long acting intravascular contrast agent. PBV is related to the signal change in the lung parenchyma and blood before and after contrast agent. We validate our method using a model of hypoxic pulmonary vasoconstriction in rats.

Table of Contents

Table of Figures

Table of Tables

Table of Abbreviations

°C	degrees Celsius
2DFT	two dimensional Fourier transform
ACA	anterior carotid artery
ADC	apparent diffusion coefficient
ANOVA	analysis of variance
ASL	arterial spin labeling
ATP	adenosine triphosphate
BE ecf	base excess of extracellular fluid
B.W.	body weight
$Bw_{receiver}$	Bandwidth of the receiver
BW_{RF}	bandwidth of the RF pulse
CASL	continuous arterial spin labeling
CBF	cerebral blood flow
CBV	cerebral blood volume
cm	Centimeter
CT	computed tomography
cTSE	centric order turbo spin echo
DCE	dynamic contrast enhancement
dL	deciliter
DOTA	1,4,7,10-tetraazacyclododecane-1,4,7,10-tetraacetic acid
DSC	dynamic susceptibility contrast
DTPA	diethylene triamine pentaacetic acid
DWI	diffusion weighted imaging
EM	electromagnetic
EPI	echo planar imaging
FID	free induction decay
FOV	field of view
Gd	gadolinium
Glu	glucose
h	hour
Hb	hemoglobin
HCO_3	bicarbonate
Hct	hematocrit
He	helium
HP	hyperpolarized gas
HP-He	hyperpolarized helium
HPV	hypoxic pulmonary vasoconstriction

i.v.	intravenously
ICA	internal carotid artery
iCa	ionized calcium
K	potassium
kg	kilogram
LMFG	linear magnetic field gradient
LSD	least significant difference
MABP	mean arterial blood pressure
MCA	middle cerebral artery
MCAO	middle cerebral artery occlusion
ml	milliliter
mM	millimolar
mm	millimeter
mmol	millimole
MRA	magnetic resonance angiography
MRI	magnetic resonance imaging
MTT	mean transit time
MTX	matrix size
n	group size
Na	sodium
nm	nanometer
NMR	nuclear magnetic resonance
NSA	number of signal averages
OP	optical pumping
PA	pulmonary artery
$PaCO_2$	arterial blood carbon dioxide pressure
PaO_2	arterial blood oxygen pressure
PBV	pulmonary blood volume
PE	pulmonary embolism
PE	polyethylene
pMCAO	permanent middle cerebral artery occlusion
PWI	perfusion weighted imaging
rA2	recombinant annexin II
Rb	rubidium
rCBF	relative cerebral blood flow
RF	radiofrequency
ROI	region of interest
ROS	reactive oxygen species
r-tPA	recombinant tissue plasminogen activator
SEOP	spin exchange optical pumping

SNR	signal to noise
sO_2	oxygen saturation
SPECT	single photon emission computed tomography
SR	sustained recovery
STP	standard temperature and pressure
T	tesla
T1WI	T_1 weighted imaging
TCO_2	total carbon dioxide content
TE	echo time
t_{max}	arterial input function corrected bolus time to maximum contrast concentration
tMCAO	temporary middle cerebral artery occlusion
TOF	time of flight
TR	transient recovery
TTC	2,3,5-triphenyltetrazoliumchloride
uL	microliters
Xe	xenon
µs	microsecond

Table of Nomenclature

$\mathbf{p}$	total nuclear angular momentum
$\boldsymbol{\mu}$	magnetic moment
γ	gyromagnetic ratio
I	net spin
$\hbar$	Planks constant/2π
m_I	-I,I+1…I-1,I
θ	angle of vector μ
B_0	main magnetic field
E	spin energy level
ΔE	difference between spin energy levels
h	Plank's constant
v	frequency of EM radiation
N	nuclei population in each spin state
ΔN	difference between population in each spin state
M_o	total net magnetization
L	torque
ω	Larmor frequency
$\mathbf{M}$	magnetization vector
$\mathbf{B_1}$	applied external magnetic field
M_x	magnetization in the x axis
M_y	magnetization in the y axis
M_z	magnetization in the z axis
M_{xy}	magnetization in the xy plane
T_1	longitudinal relaxation time
T_2	transverse relaxation time
α	inversion efficiency
T_2^*	transverse relaxation time due to diffusion, susceptibility, and main magnetic field inhomogeneity
G	gradient strength
ω_{eff}	effective precessional frequency
Δz	slice thickness
G_{freq}	frequency encoding gradient strength
G_{phase}	phase encoding gradient strength
Φ	phase
FOV_p	field of view in the phase axis
t	Time

$\Delta\Phi$	phase change
δ	gradient duration
r	position
b	diffusion weighting
t_{diff}	time between application of gradients
ρ	tissue density
T_1'	measured longitudinal relaxation rate
$\Delta\omega$	change of precessional frequency
B_{eff}	effective applied magnetic field
A	amplitude of RF pulse
P	polarization
$P_{thermal}$	thermal polarization
S_c	control image
S_L	labeled image
C(t)	bolus concentration
A	amplitude of change in bolus concentration (Chapter II)
α, β	scaling factors in gamma variate fit (Chapter II)
rCBV	relative cerebral blood volume
rMTT	relative mean transit time
$R_2^*\Delta$	change in the transverse relaxation rate
$T_{1,O2}$	longitudinal relaxation time due to oxygen
ζ	2.6 bar/s
pO_2	partial pressure of oxygen
S_m	signal intensity of the m^{th} image
S_0	signal intensity of the first image
τ	time between image acquisitions
p_o	initial partial pressure of oxygen
R	rate of oxygen uptake
S_{RF0}	signal intensity of the first RF calibration image
$\Delta\tau_{RF}$	time between RF calibration images
ε	RF correction factor
α	flip angle (chapter 4)
N	image number (chapter 4)
A_m	simulated signal intensity
M_m	noiseless signal intensity
μ, σ	parameters describing the Gaussian distribution (Chapter IV,V)
T_{1v}	blood longitudinal relaxation time

T_{1ev}	extravascular longitudinal relaxation time
T_{1ev}'	exchange affected extravascular longitudinal relaxation time
T_{1v}'	exchange affected blood longitudinal relaxation time
f_{ev}	extravascular water fraction
f_{ev}'	exchange affected extravascular water fraction
f_v	vascular water fraction
f_v'	exchange affected vascular water fraction
τ_{ev}	extravascular water residence time
τ_v	vascular water residence time
$S_{tissue,pre}$	precontrast administration tissue signal intensity
$S_{tissue,post}$	postcontrast administration tissue signal intensity
$S_{blood,pre}$	precontrast administration blood signal intensity
$S_{blood,post}$	postcontrast administration blood signal intensity
TI	inversion time
S_{blood}	signal intensity of blood
$S_{tissue,noise}$	simulated signal intensity of tissue with noise
S_{tissue}	simulated signal intensity of tissue without noise
n	simulations (Chapters IV,V)
S_{ROI}	signal intensity of the region of interest
$S_{phantom,\ pre}$	signal intensity of the phantom prior to contrast agent infusion
$S_{phantom,\ post}$	signal intensity of the phantom after contrast agent infusion

Copyright Notice

Parts of this thesis have appeared in the following publication

Bratane B.T., Walvick, R.P., Corot, C., Lancelot, E., Fisher, M., "Characterization of gadolinium-based dynamic susceptibility contrast perfusion measurements in permanent and transient MCAO models with volumetric based validation by CASL." Journal of Cerebral Blood Flow and Metabolism 30(2): 336-342 (2010) (Reproduced with permission).

Materials in **Figure 1.14** were adapted with permission from Hornak JP. The Basics of MRI. Volume 2010: Interactive Learning Software; 2010

Material in **Figure 1.15** were reproduced with permission from Bernstein MA, King KF, Zhou XJ. Advanced Pulse Sequence Techniques. Burlington: Academic Press; 2004. p. 802-954.

Chapter I: Introduction

1.1 Introduction to Magnetic Resonance Imaging

Magnetic Resonance Imaging (MRI) is a powerful tool useful in measuring the structural and functional properties of biological tissue. The following section will review the fundamentals of physics germane to MRI signal acquisition and describe the ability to exploit these phenomena for image acquisition and contrast generation. Several sources were utilized in the preparation of this section including works from Bernstein (1), McRobbie (2), Sotak (3), Haacke (4), and Hornak (5).

1.1.1 Spin Physics

An atom consists of negatively charged electrons, positively charged protons, and neutrally charged neutrons. The neutrons and protons comprise the atom's nucleus. Electrons orbit around the nucleus. The nucleus (as well as electrons) contains both orbital and spin angular momentum. The summation of the orbital and spin angular momentum is termed the total nuclear angular momentum and expressed as a vector, **p**. A charged particle or nucleus which possesses a nonzero angular momentum is associated with a magnetic moment, and can be expressed as a vector, **μ.** The relationship between **p** and **μ**

$$\boldsymbol{\mu} = \gamma \boldsymbol{p} \qquad [1.1]$$

where γ is known as the gyromagentic ratio and is specific to the nucleus. The parameter γ is a function of the ratio of the charge of the nucleus to its mass.

The magnitude of the vector **p** is based on the net spin, I, of the nucleus. The net spin is determined by the number of unpaired protons and neutrons. If, for example, there

exists one unpaired neutron or proton, the net spin is equal to ½. In another configuration, both an unpaired proton and an unpaired neutron exist within a nucleus which results in a net spin equal to 1. A nucleus has no net spin when both protons and neutrons are paired. The relationship between |p| and I is expressed as:

$$|p| = \hbar\sqrt{I(I+1)} \quad [1.2]$$

where $\hbar$ is Plank's constant (6.626068 * 10^{-34} m2 kg/s) divided by 2π. Equation 1.2 and 1.1indicates that if the net spin, I, of a nucleus equals 0, the magnitude of the vector **p** is 0 and the nucleus has no angular momentum and no magnetic moment. The magnitude of **μ**, can be expressed as

$$|\mu| = \gamma\hbar\sqrt{I(I+1)} \quad [1.3]$$

The direction of **p** is quantized in a finite number of directions. The longitudinal component of **p**, p_z, is limited to $\hbar m_I$ where m_I consists of –I, -I+1…,I-1, I. From this, the longitudinal component of the magnetic moment, u_z can be expressed as

$$\mu_z = \gamma\hbar m_I \quad [1.4]$$

and the angle, θ, of the vector **u** can be expressed as

$$\cos\theta = \frac{\mu_z}{|u|} \quad [1.5]$$

Figure 1.1 graphically displays the possible orientations of the magnetic dipole moment of a net spin-1/2 nucleus.

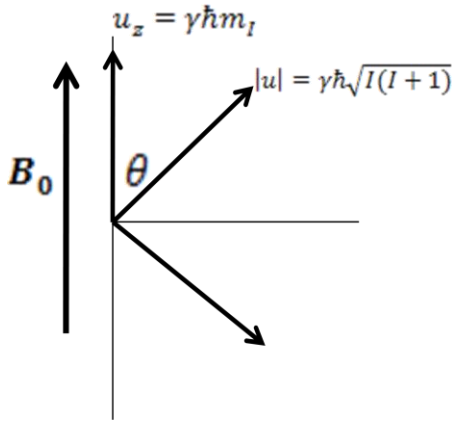

Figure 1.1 Possible orientations of the magnetic dipole moment of a spin-1/2 nucleus.

1.1.2 Establishing the Boltzmann Equilibrium

Considering a single nucleus with magnetic dipole moment, **μ**, placed inside an external magnetic field, $\mathbf{B_o}$, the energy of that nucleus is given by:

$$E = |\mu|\boldsymbol{B_0}\cos\theta \qquad [1.6]$$

Substituting equation 1.3, 1.4, and 1.5, equation 1.6 becomes

$$E = \pm\frac{\gamma\boldsymbol{h}}{2}\boldsymbol{B_0} \qquad [1.7]$$

for a spin-1/2 system. A spin-1/2 nucleus can have only two possible orientations of u_z and therefore, can have two possible energy levels. In this case the lower energy state (spin-up) is aligned with the external magnetic field, where as the higher energy state (spin-down) will be aligned anti-parallel. The difference in energy states of a spin-1/2 nucleus is

$$\Delta E = \hbar\gamma\boldsymbol{B_o} \qquad [1.8]$$

The magnitude of the difference in energy states is proportional to the magnetic field strength. Further, in the condition where the bulk spins are outside of an external

magnetic field, equation 1.8 indicates that the difference in energy levels in 0. Outside of an external magnetic field, the spins have no favored orientation. When considering bulk nuclei, the Nuclear Magnetic Resonance (NMR) signal results from a small population difference of nuclei between the two energy states. This will be discussed below. An energy level diagram is displayed in Figure 1.2.

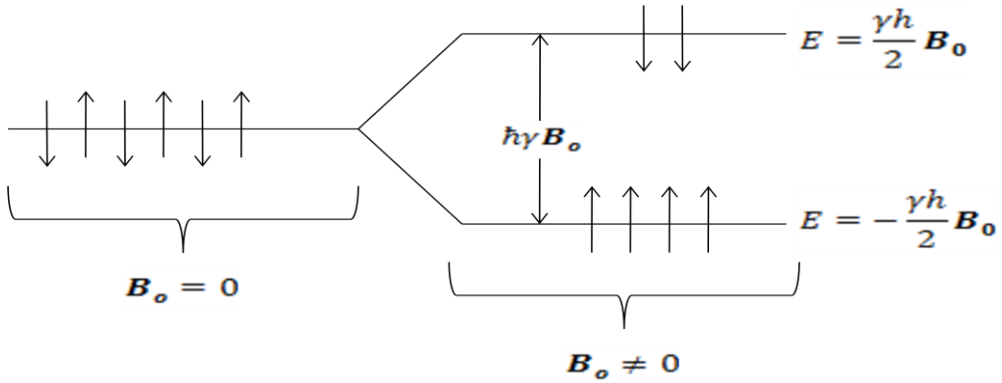

Figure 1.2 Energy Level Diagram of spin-1/2 nuclei inside and outside the main magnet field, B_0. Each arrow represents individual nuclei.

1.1.3 Energy Level Transitions

In order to transition from spin-up to spin-down, electromagnetic (EM) radiation in the radio frequency (RF) wavelength must be absorbed by the spin. Conversely, a transition from the spin-down state to spin-up requires a release of EM radiation in the RF wavelength. The energy of the EM radiation required to transition from spin-up to spin-down is equal to the difference between the two energy states as

$$\Delta E = h\nu \qquad [1.9]$$

where ν is the frequency of the EM radiation and h is Plank's constant. By conservation of energy, equations 1.8 and 1.9 can be equated. After rearranging terms, ν is defined by

$$v = \frac{\gamma}{2\pi} \boldsymbol{B_o} \quad [1.10]$$

The frequency ν is the frequency of the EM radiation required to transition a spin system with a specified γ and Bo. The NMR signal is derived by the energy released from a spin as it relaxes from the spin-down state to the spin-up state.

1.1.4 Boltzmann Equilibrium

The distribution of the spins at each energy level is dependent on the Boltzmann Equilibrium expressed (for net spin-1/2 nuclei) as

$$\frac{N^-}{N^+} = e^{\frac{\Delta E}{kT}} \quad [1.11]$$

where $N^{\pm}$ is the population of nuclei in each spin configuration state, k is the Boltzmann constant (1.38×10^{-23} Joules/°Kelvin) and T is the temperature in Kelvin. The difference in spin populations (ΔN) is expressed by

$$\Delta N = \frac{N \Delta E}{2KT} \quad [1.12]$$

where N is the total number of nuclei. The population difference is therefore dependent on the temperature, the energy differences (which is dependent on the main magnet field), and the total number of nuclei.

The total magnetization, $M_{o,}$ can be considered the sum total of the magnetic moments expressed as

$$M_o = \sum_{m=-I}^{I} N_m \mu_{z,m} \quad [1.13]$$

where N_m is the number of spins and $\mu_{z,m}$ is the z component of the vector $\boldsymbol{\mu}$ in the spin-I configuration. For the common spin-1/2 case, the magnetization is related directly to the population difference as

$$M_o = \frac{\gamma\hbar(\Delta n)}{2} \quad [1.14]$$

In the spin-1/2 system, M_o will face parallel to the magnetic field, B_o at thermal equilibrium. The NMR signal is proportional to M_o and therefore is dependent on the magnetic field strength, B_0 and the gyromagnetic ratio, γ.

1.1.5 Classical Description of NMR

It is instructive to explore the interaction of a single spin with a magnetic moment μ with the main magnetic field, B_0. The magnetic moment will experience a torque induced by B_0 expressed as:

$$L = \frac{dp}{dt} = \boldsymbol{\mu} \times \boldsymbol{B_0} \quad [1.15]$$

Thus, the torque of the system is equal to the change of angular momentum as a function of time. Considering the magnetic moment is equal to the angular momentum times the γ, equation 1.15 can be expressed as

$$\frac{d\boldsymbol{u}}{dt} = \gamma \frac{d\boldsymbol{p}}{dt} = \gamma\boldsymbol{\mu} \times \boldsymbol{B_0} \quad [1.16]$$

This equation indicates that the magnetic moment, **μ** will precessing around B_0. In the absence of any externally applied RF energy, the processional frequency of the μ can be described by the Larmor equation

$$\omega = \gamma \boldsymbol{B_0} \quad [1.17]$$

It is further useful to describe equation 1.16 in terms of the net magnetization, **M**. This vector represents the sum of all magnetization vectors. Equation 1.16 can be rewritten as

$$\frac{d\boldsymbol{M}}{dt} = \gamma \boldsymbol{M} \times B_0 \quad [1.18]$$

indicating that the net magnetization vector is precessing around B_0. Figure 1.3 is a representation of the formation of the net magnetization **M**. The magnetic dipole moment vector, **μ**, of each nuclei is precessing around $\mathbf{B_0}$ with a distribution in each configuration according to the Boltzmann equilibrium which is represented on the left of Figure 1.3. There is a net number of spins precessing in the spin-up orientation. Combining the spins, a net magnetization vector, **M** is also precessing with a spin-up orientation.

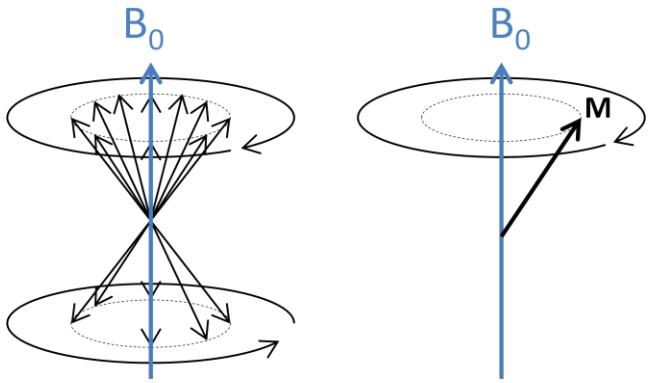

Figure 1.3 Left: Nuclei precess around B0 with a slight bias for the spin-up configuration. Right: The net magnetization vector precesses in a spin-up configuration around B_0

1.1.6 The Bloch Equations

As seen in previous sections, the net magnetization is influenced by the strength of the main magnetic field, B_o. It can also be influenced by the application of RF radiation, as previously described. The presence of RF energy creates an applied magnetic field, B_1. The response of the net magnetization to both B_0 and B_1 has been described by Bloch (6). The equations describe dynamically changing motion of the net magnetization vector, **M**, in each of the three axes as:

$$\frac{dM_x}{dt} = \gamma B_0 M_y + \gamma B_1 M_z \sin(\omega t) - \frac{M_x}{T_2} \qquad [1.19]$$

$$\frac{dM_Y}{dt} = -\gamma B_0 M_X + \gamma B_1 M_z \cos(\omega t) - \frac{M_y}{T_2} \quad [1.20]$$

$$\frac{dM_z}{dt} = -\gamma[\sin(wt)\, M_x + \cos(\omega t)\, M_y] - \frac{M_{z-M_o}}{T_1} \quad [1.21]$$

These equations assume that B_1 is oscillating and applied in the transverse (xy) plane and rotating with frequency ω and B_o is parallel with the z axis. When describing the Bloch equations, it is customary to describe the x-y plane as rotating at the Larmor frequency. In this treatment, the B_0 components of equation 1.19 and 1.20 can be set to 0. The terms T_2 and T_1 are relaxation terms that describe the time constant of the return of the system to thermal equilibrium. More specifically, T_2 describes the dephasing of magnetization in the x-y plane and T_1 describe the return of the magnetization to the Boltzmann equilibrium. Following the application of an applied RF field (B_1=0) and assuming the reference frame rotating at ω, the Bloch equations reduce to

$$\frac{dM_{xy}}{dt} = -\frac{M_{xy}}{T_2} \quad [1.22]$$

$$\frac{dM_z}{dt} = -\frac{M_{z-M_o}}{T_1} \quad [1.23]$$

Solving for the differential equations, the time course of the transverse and longitudinal magnetization following the application of B_1 can be described as:

$$M_{xy}(t) = M_o e^{\frac{-t}{T_2}} \quad [1.24]$$

$$M_z = M_o(1 - \alpha e^{\frac{-t}{T_1}}) \quad [1.25]$$

where α is either 1 or 2 depending if the magnetization was tipped into the transverse plane or inverted, respectively. The physical meaning of the time constants, T_1 and T_2 will be described below.

1.1.7 Free Induction Decay

In order to understand the mechanism of NMR signal generation and contrast weighting, it is necessary to understand the reaction of the net magnetization vector, **M** to the application of an RF pulse in the transverse plane. In MRI and NMR experiments, the RF pulse flip angle is defined by the amount of rotation into the transverse plane that it induces on the net magnetization. The amount of rotation, or flip angle, is defined by

$$\tau\gamma B_1 \qquad [1.26]$$

where τ is the pulse length in seconds. This process is depicted in Figure 1.4.

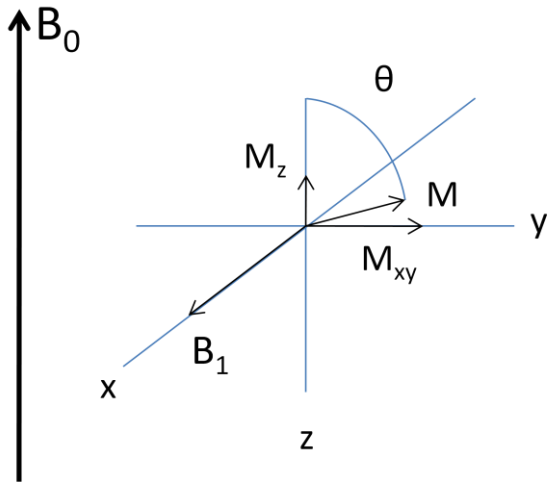

Figure 1.4 Depiction of the net magnetization vector responding to an applied RF field. The longitudinal component of **M** is reduced whiled the transverse component is increased.

The RF pulse is produced by a sinusoidal varying electrical current through a RF coil. The electrical current generates a magnetic field, B_1, perpendicular to B_0. The detection of the NMR signal occurs in the transverse plane to avoid the influence of the main magnetic field.

The instant that the RF pulse is disengaged, the net magnetization begins to lose its phase coherence through T_2^* mechanisms (described below). Taken together with the

torque produced by the main magnetic field, the net magnetization produces a decaying, sinusoidal magnetic field, inducing a corresponding sinusoidal decaying electrical voltage in the RF coil. This is known as the free induction decay (FID). An example FID is depicted in Figure 1.5

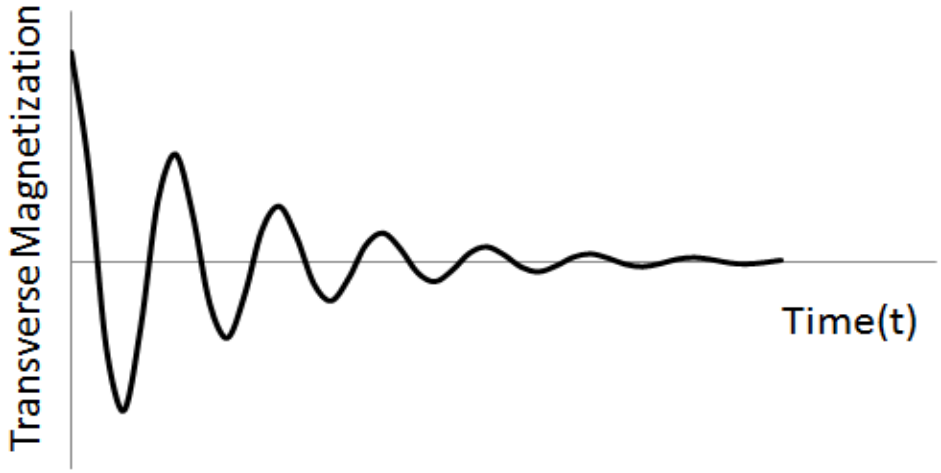

Figure 1.5 The time course of the transverse magnetization following an RF pulse

The time varying magnetic field produced an electric current in the RF coil. The electrical current is recorded and a Fourier transform is applied to obtain the frequency and amplitude of the original NRM signal.

1.1.8 NMR Relaxation Mechanisms

Much of the contrast produced in NMR and MRI can be obtained by exploiting the relaxation mechanism, T_1 and T_2. The relaxation times are characteristic of the tissue under investigation and can provide valuable information about the tissue physiology and the effects of disease processes. The section below will describe the origins of these relaxation mechanisms and techniques used to measure them.

1.1.8.1 T_1 – Longitudinal Relaxation

Following excitation with an applied RF pulse, the longitudinal magnetization recovers to Boltzmann equilibrium with the time constant, T_1. This time constant is dependent on the efficiency in which a spin gives up energy to the surrounding lattice, or surrounding environment. Protons in water lose energy to the lattice very efficiently if the water molecule is bound to other biomolecules. Thus, bound water has a faster T_1 as compared to free water. The effect of binding can be quantified as the molecules rotational rate (also known as the rotational correlation time). Rotational rates faster than the Larmor frequency lose energy to the lattice less efficiently. T_1 contrast agents work by binding water and increasing the bound water molecules overall correlation time. Therefore, presence of a contrast agent serves to shorten the T_1 of the water molecules.

The most common methodology for measuring the longitudinal relaxation time is through the use of inversion recovery. The net magnetization vector is inverted to the –z axis through the application of a 180° RF pulse. The net magnetization will begin to recover to its thermal equilibrium. At varying times following the 180° inversion pulse, the magnetization is sampled in the transverse plane through the application of a second RF pulse. The longitudinal magnetization can be sampled at varying times following the inversion pulse. This delay between the inversion pulse and the sampling pulse is known as the inversion time. By fitting the sampled magnetization to equation 1.25, the longitudinal relaxation time can be determined. The time course of the longitudinal magnetization followed by an inversion depicted in Figure 1.6.

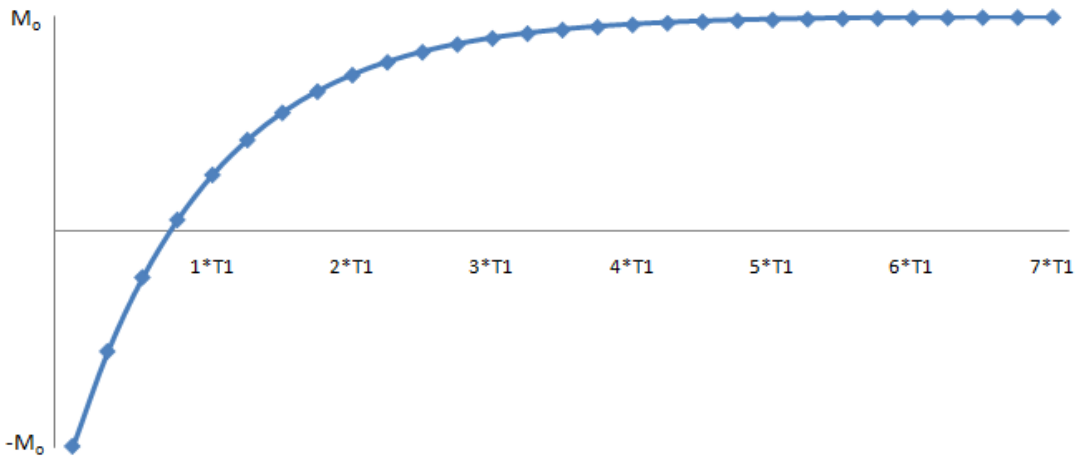

Figure 1.6 The time course of the longitudinal magnetization following an inversion of the magnetization.

1.1.8.2 T_2 – Transverse Relaxation

Following the application of a RF pulse, magnetization is tipped onto the transverse plane. At the instant the RF pulse is disabled, the net magnetization is precessing coherently. That is, the individual spins are precessing with the same phase. The transverse relaxation is the process by which this phase coherence is lost. Phase coherence is lost due to the interaction of spins with each other. This process is known as spin-spin relaxation. When interacting, spins will either precess slightly faster or slower than their Larmor frequency. Once isolated from each other, they return to precessing at their Larmor frequency with different phases. Eventually all spins in the transverse plane will be precessing with random phases and the net magnetization in the transverse plane will dissipate. The exponential time constant of this process is the T_2.

Other factors contribute to the loss of phase coherence of the system including inhomogeneities of the main magnetic field, magnetic susceptibilities (i.e. an induced

magnetism in a material due to an external magnetic field), and molecular diffusion. The time constant of loss of magnetic coherence due to the above factors is termed T_2^*. T_2^* can be quantified as:

$$\frac{1}{T_2^*}=\frac{1}{T_2}+\frac{1}{T_2^{IH}}+\frac{1}{T_2^{MS}}+\frac{1}{T_2^{MD}} \quad [1.27]$$

where T_2^{IH}, T_2^{MS}, and T_2^{MD} are the T_2 contributions due to main magnetic field inhomogeneities, magnetic susceptibility, and molecular diffusion.

To measure the T_2 directly, a technique known as Hahn Spin Echo can be used

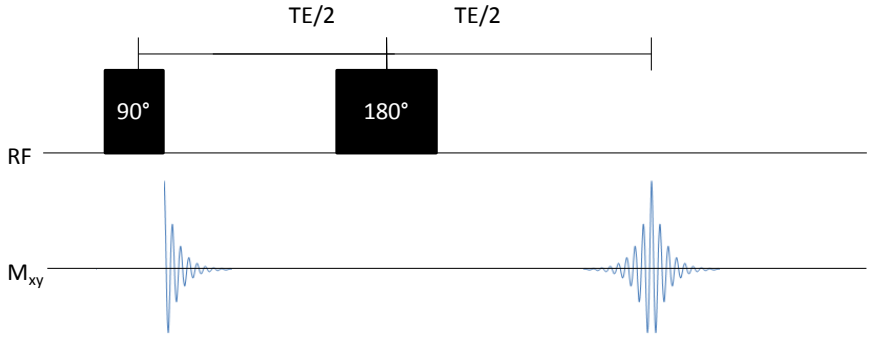

Figure 1.7 Diagram of the production of a Hahn Spin Echo

which is depicted in Figure 1.7. A spin echo can be used to isolate the decay due only to the T_2 and not due to inhomogeneities, magnetic susceptibility, and molecular diffusion. Following a 90° pulse which tips the net magnetization into the transverse plane a loss of phase coherence begins. After some time, TE/2, where TE is known as the echo time, a 180° pulse is applied and the phase of spins in the transverse plane are reversed. At time TE, the phase of the signal is aligned and a spin-echo is produced. Although the phase coherence loss due to T_2 spin-spin relaxation is non-recoverable, phase coherence loss due to magnetic field inhomogeneities, magnetic susceptibility and molecular diffusion

can be reversed due to their non-random nature. This measurement can be repeated for different values of TE allowing for the T_2 to be determined.

1.1.9 Image Formation

Image formation in MRI is accomplished by changing the Larmor frequency of spins as a function of position through the use of spatially changing magnetic fields. This is performed through the application of linear magnetic field gradients. The following section will describe how these gradients are used in order to perform slice selection and in-plane magnetization localization.

1.1.9.1 Linear Magnetic Field Gradients

Linear magnetic field gradients (LMFG) produce a change in the static magnetic field as a function of position. Suppose a LMFG is applied along the z-axis. The effective precession frequency, ω_{eff}, would be dependent on its position on the z axis as:

$$\omega_{eff} = \omega - \gamma(G * z) \qquad [1.28]$$

where G is the gradient strength in units Gauss/cm, z is the distance from the isocenter of the magnet. Spins located at the isocenter of the magnet will experience no change in its Larmor frequency while spins away from the isocenter will experience a linear change in the Larmor frequency depending on that distance from the isocenter.

1.1.9.2 Slice Selection

In typical NMR spectroscopy, an RF pulse is applied and the entire sample within the RF coil is affected. With the addition of LMFG, spins from a finite slice can be

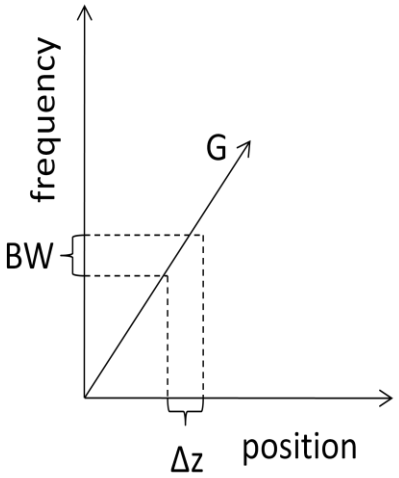

Figure 1.8 Graphical depiction of slice selection. The slice width, Δz, is dependent on the gradient strength, G, and the RF pulse Bandwidth

selected. A gradient applied along the axis of slice selection will cause the spins to precess at a frequency dependent on how far it is from the isocenter of the magnet. If an RF pulse is applied with a frequency bandwidth, BW_{RF}, only spins with precession frequencies within that bandwidth will be tipped into the transverse plane. If the center frequency of the RF pulse is set to the Larmor frequency, spins with precession frequencies of from $\omega - BW_{RF}/2$ to $\omega + BW_{RF}/2$ will be tipped into the transverse plane. The slice thickness, Δz, in cm, can be calculated by:

$$\Delta z = \frac{BW_{RF}}{\gamma G} \qquad [1.29]$$

Figure 1.8 graphically displays slice selection. Slice offset from the isocenter can be achieved by changing the carrier frequency of the RF pulse to values higher or lower than

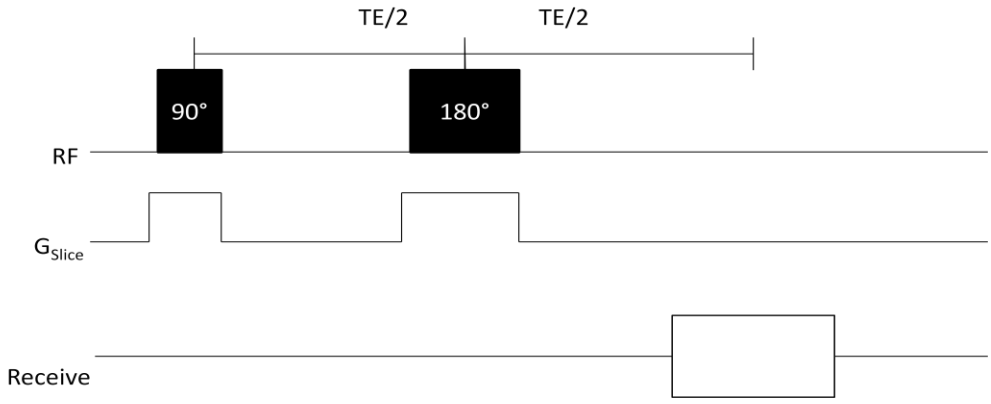

Figure 1.9 Modification of the Hahn spin echo with slice encoding gradients.

the Larmor Frequency thus exciting a different set of frequencies. The addition of slice selection to a standard NMR Hahn spin echo experiment is shown if Figure 1.9.

1.1.9.3 Frequency Encoding

Following tipping the desired spins into the transverse plane, in plane encoding must be accomplished. One dimension of the in-plane encoding can be obtained using frequency encoding. During signal acquisition, a LMFG is applied along the axis in which spatial encoding is desired. The precessional frequency of the FID (or spin echo) of the slice selected spins is determined by their position away from the isocenter of the magnet in desired axis of spatial encoding. Therefore, during acquisition with frequency encoding, the signal will be comprised of a wide range of frequencies.

The field of view (FOV) in the axis of frequency encoding can be described in terms of the receiver bandwidth ($BW_{receiver}$) by:

$$FOV = \frac{BW_{receiver}}{\gamma G_{Freq}} \quad [1.30]$$

where the $BW_{receiver}$ is equal to the ratio of the data points used to sample the signal and the acquisition time and G_{Freq} is the gradient strength in the frequency direction. Figure 1.10 shows a modified Hahn spin echo pulse sequence with both frequency and slice selection.

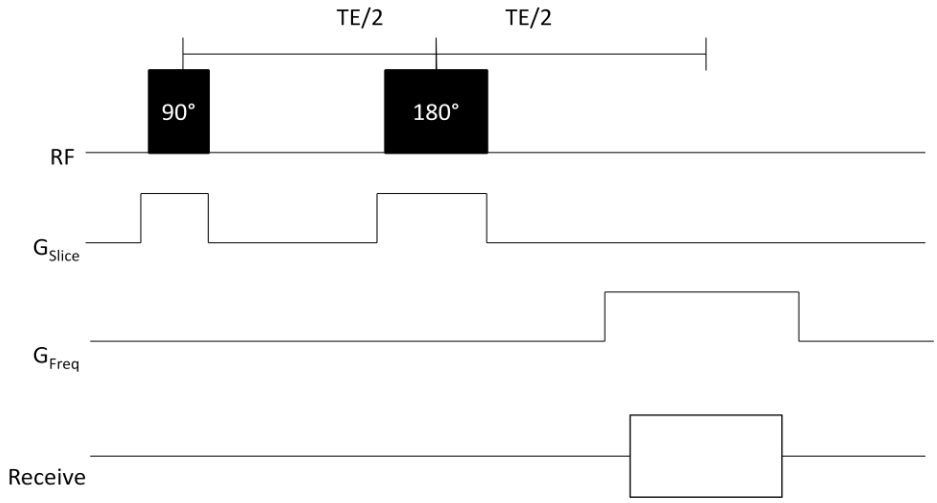

Figure 1.10 Hahn spin echo sequence with the addition of slice and frequency encoding

1.1.9.4 Phase Encoding

Encoding in the second direction can be accomplished via modifying the phase of the spins. Following tipping the desired spins into the transverse plane, a gradient is applied in the desired axis of encoding prior to signal acquisition. The gradient temporarily changes the precessional frequency of the spins as a function of the spin's distance from the isocenter of the magnet. The gradient is then disabled and the precessional frequency returns to the Larmor frequency. Because of the temporary change in frequency, the spins are precessing with a different phases as a function of the

spin's distance from the isocenter in the desired encoding axis. The amount of phase acquired by a spin at a distance d from the iosocenter in the desired encoding axis is:

$$\phi = \gamma G_{phase} dt \quad [1.31]$$

where G_{phase} is the gradient strength in the phase encoding direction and t is the time of the gradient. This equation holds true only for square shaped gradient waveforms. The

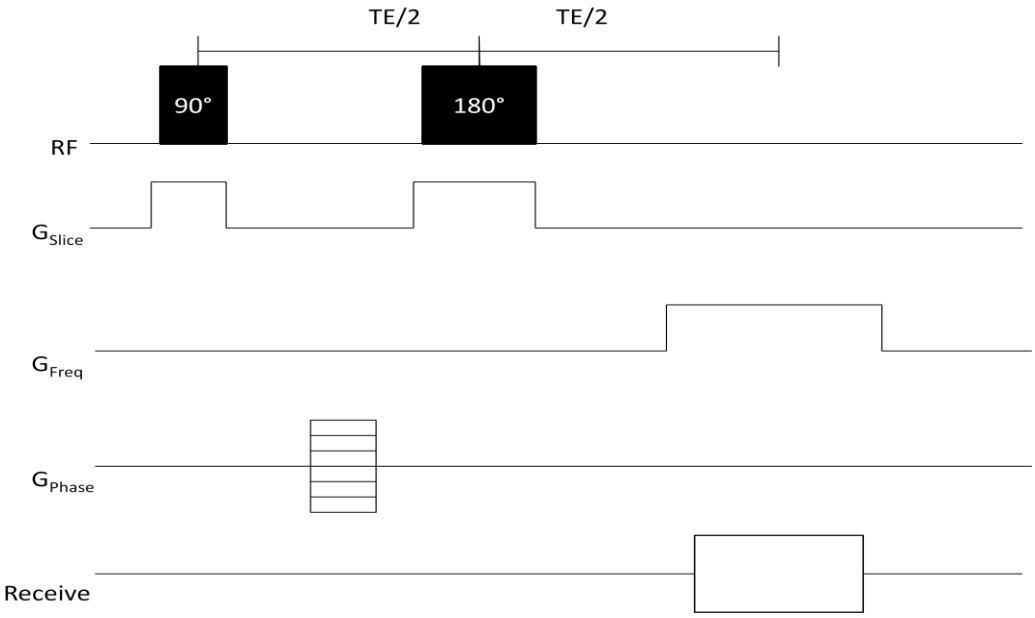

Figure 1.11 Hahn spin echo with the addition of slice, frequency, and phase encoding.

strength of G_{phase} can be incrementally increased to produce a full range of phase offset from -180° to +180°. The minimal amount G_{phase} can be incrementally increased, $G_{p(min)}$, is a function of the FOV in the phase direction, FOV_p, and the gradient duration, t, can be calculated by:

$$G_{p(\min)} = \frac{1}{\gamma FOV_p t} \quad [1.32]$$

Taken together with frequency encoding, incrementally increasing the phase encoding gradient will allow for complete mapping of the image space. The Hahn spin echo pulse

sequence is shown is Figure 1.11 with the addition of phase encoding gradients. The gradient depicted on the phase encoding axis indicating the ability of the gradient to take on a number of different values.

Each increment of the phase encoding gradient is delayed by a recovery time, TR. The total acquisition time of a sequence is equal to the total number of phase encoding gradient increments multiplied by the TR.

1.1.9.5 Rephasing Gradients

Both the slice selection gradient and the frequency encoding gradient cause the unwanted side of effect of dephasing the transverse relaxation. This can be remedied by the addition of a rephasing gradient. In the case of the slice selection, the rephasing

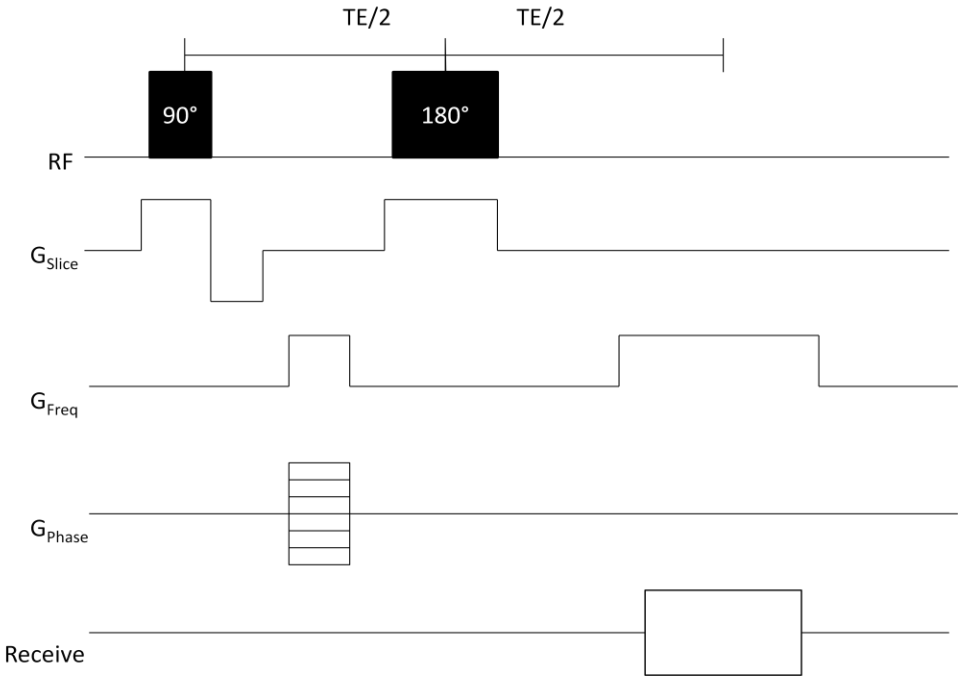

Figure 1.12 A complete Hahn spin echo sequence

gradient serves to rephase the spins following the application of the slice selection gradient. In the case of the frequency encoding, a gradient is placed prior to the frequency encoding gradient. This gradient serves to diphase the signal such that during the application of the frequency encoding gradient, the spins are brought into phase coherence. The complete pulse sequence is given in Figure 1.12

1.1.9.6 Gradient Echo Imaging

Thus far, pulse sequences have been described using Hahn spin echo signal excitation. Excitation can also be accomplished with a single RF pulse with a flip angle <= 90°. Following the RF pulse, the longitudinal magnetization is tipped into the transverse plane. The amount of magnetization in the transverse plane by an RF flip angle is given by

$$M_{xy} = M_0(1 - cos\theta) \quad [1.33]$$

Once tipped into the transverse plane, the magnetization begins to lose phase coherence due to the T_2* relaxation mechanism described earlier. The time between the excitation and the signal acquisition (TE) determines the magnitude of decay due to the T_2*. Similar to the Hahn spin echo pulse sequence, the slice selection, phase encoding, and frequency encoding gradients are present.

1.1.9.7 Mapping k-space

For each increment of the phase-encoding gradient and an applied frequency-encoding gradient during signal acquisition, a separate time domain signal is acquired consisting of signals with varied frequencies and phases. Each increment of the phase

encoding gradient from $\pm G_p$ can be placed in a line of a matrix. This matrix is known as k-space. By performing a two dimensional Fourier Transform (2DFT), the time domain signal can be transformed to the frequency domain which will result in a 2D MR image.

K-space can be mapped in a number of ways. In one method, each spin excitation can be used to fill one line of k-space. As mentioned above, the acquisition would be repeated identically except that the phase encoding gradient would be incrementally increased from $-G_p$ to $+ G_p$. Another method consists of filling multiple lines of k-space after a single acquisition. Applications of this methodology are described below.

1.1.9.7.1 Echo Planar Imaging

Echo planar imaging (EPI) describes a methodology in which a multiple number of lines of k-space can be acquired following a single RF pulse. This method is

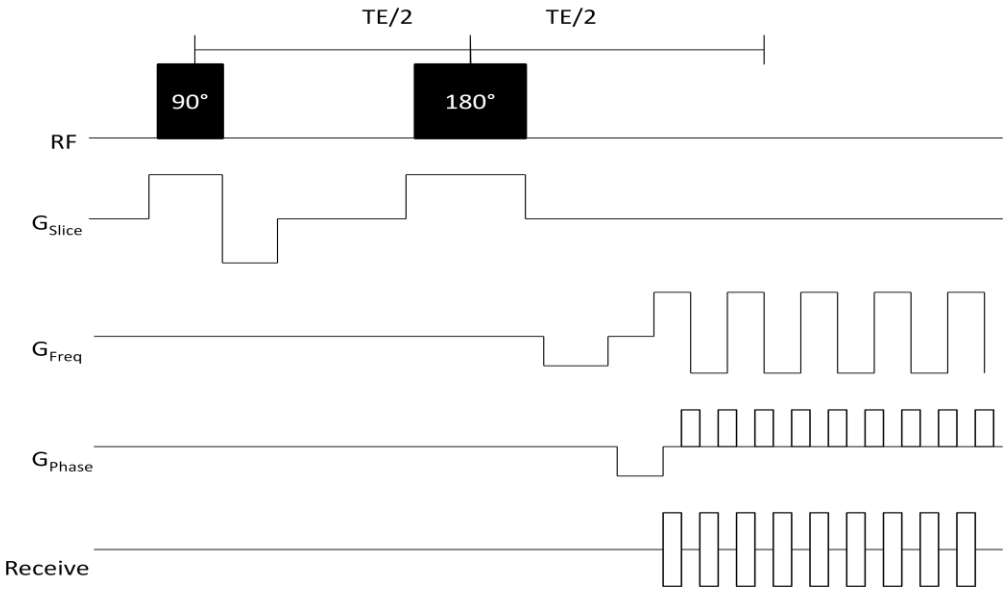

Figure 1.13 An Echo Planar Imaging Sequence using the blip technique

advantageous due to the speed in which image acquisition can be performed. A variant of EPI is described in Figure 1.13. Following RF excitation an initial prephasing gradient is applied which sets the phase of the spins to $-G_p$. Next, an oscillating frequency encoding is applied. Prior to each oscillation of the frequency-encoding gradient, a small phase encoding gradient, or blip, is applied to increment the phase of the spins. K-space is acquired in a rectilinear fashion. While providing rapid acquisition of imaging information, EPI based acquisitions typically require longer echo times. In EPI acquisition, the echo time is defined as the time between the initial excitation and the acquisition of the data from the center of k-space. The longer echo times may result in higher sensitivity to T_2^*.

1.1.9.7.2 Turbo Spin Echo

In this method of rapidly traversing k-space, a modified Hahn spin-echo sequence is used known as the Carr-Purcell-Meiboom-Gill sequence. In this sequence, a 90° pulse is applied followed by multiple 180° RF pulses which constantly rephrase the magnetization resulting in numerous spin echoes each attenuated by the T_2 relaxation time. Between each 180° RF pulse, an incremented phase encoding gradient is applied followed by a phase encoding gradient during signal acquisition. In this scheme, each subsequent spin echo encodes a line of k-space. This process is described in Figure 1.14. The number of lines of k-space acquired with each 90° RF pulse defines the amount in which image acquisition is accelerated. Although images can be obtained rapidly, the signal encoded in each line of k-space will have been attenuated by a different amount due to T_2 decay which may affect uniform sampling of k-space and cause image artifacts.

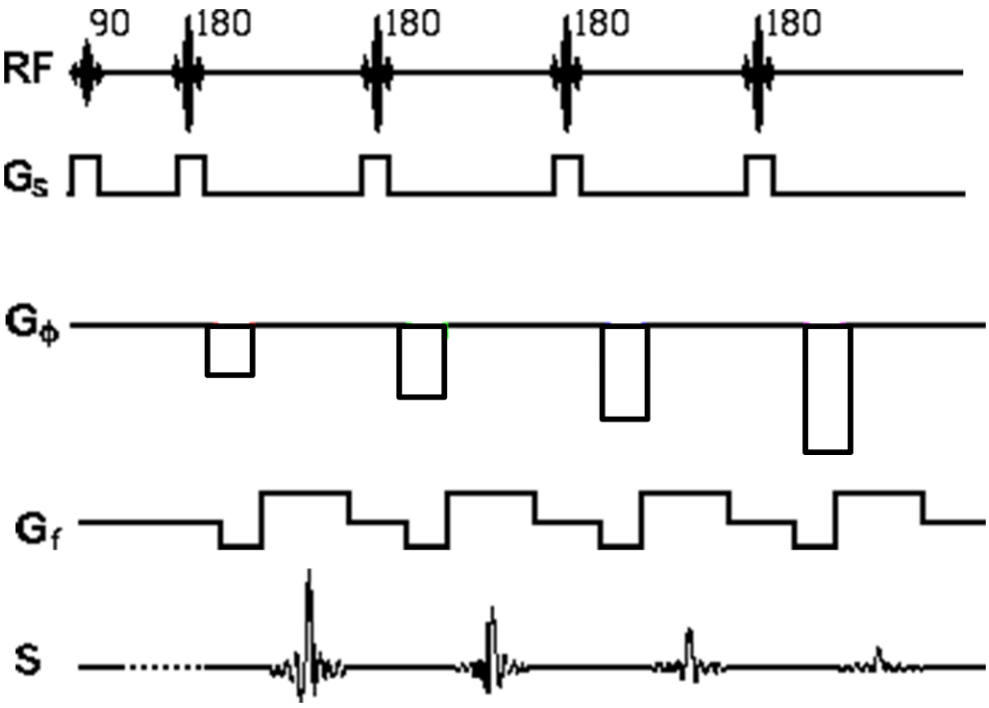

Figure 1.14 Turbo Spin Echo Sequence. The phase encoding gradient strength increases after each refocusing pulse to fill k-space. Adapted from Hornak with permission (5).

1.1.10 Image Weighting

Depending on the parameters of the pulse sequence, different image weightings can be achieved. The following section will describe various weightings that were utilized in subsequent chapters of this dissertation.

1.1.10.1 T_2, T_2, and T_1 Weighted Images*

In order to achieve contrast in MRI, the duration of the echo time (TE) and recovery time (TR) can be varied. To achieve a weighting based on a tissues T_1 value, both the recovery time and the echo time are shortened. A short TE minimizes the effect of T_2 and T_2* decay while a short TR allows for greater signal enhancement in tissue which has a faster T_1 recovery time. To achieve T_2 or T_2* weighting with a spin echo or gradient echo sequence, respectively, a long TR and TE time should be utilized. The long

TE time allows for tissue with longer transverse relaxation times to have higher signal intensity while the long TR reduces the influence of the longitudinal relaxation time.

1.1.10.2 Diffusion Weighted Imaging

Diffusion Weighted Imaging (DWI) has emerged as a valuable tool for characterizing and diagnosing a number of disease states including cancer and stroke (7,8). Diffusion weighting is sensitive to the random Brownian motion of water. A clear picture of molecular motion is impossible due to a number of factors including pressure gradients, thermal gradients, and interaction with ionic components (9). A measurement of the combined effects of many processes on the molecular motion of water molecules is quantified as the apparent diffusion coefficient (ADC).

Water diffusion can be either isotropic or anisotropic. In the case of isotropic diffusion, water is free to move in any arbitrary axis. In anisotropic diffusion, water may be restricted in one or more of any arbitrary axis. In this case, the ADC can be defined as a tensor, $\overline{ADC}$, as

$$\overline{ADC} = \begin{bmatrix} ADC_{xx} & ADC_{xy} & ADC_{xz} \\ ADC_{xy} & ADC_{yy} & ADC_{yz} \\ ADC_{xz} & ADC_{yz} & ADC_{zz} \end{bmatrix} \quad [1.34]$$

The elements on the diagonal represent diffusion in each of the three orthogonal axes, while the off diagonal terms represent the degree of random motion between two orthogonal axes (1). In the case of isotropic diffusion the diffusion coefficient, $\overline{ADC}$, is equal to the ADC in any direction. To quantify anisotropic diffusion, the average ADC can be calculated as:

$$< ADC >= \frac{ADC_{xx}+ADC_{yy}+ADC_{zz}}{3} \quad [1.35]$$

The measurement of diffusion can be accomplished using a Hahn spin echo, echo-planar imaging with a pair of bipolar gradients that straddle the 180° pulse in the axis of diffusion encoding. Figure 1.15 displays a sample pulse sequence for diffusion imaging. The first of the bipolar gradient on the phase encoding axis imposes a phase shift on the spins, similar to the effect of the phase-encoding gradient. The second bipolar gradient imposes a further phase, however, because of the rephasing of the 180° RF pulse, the

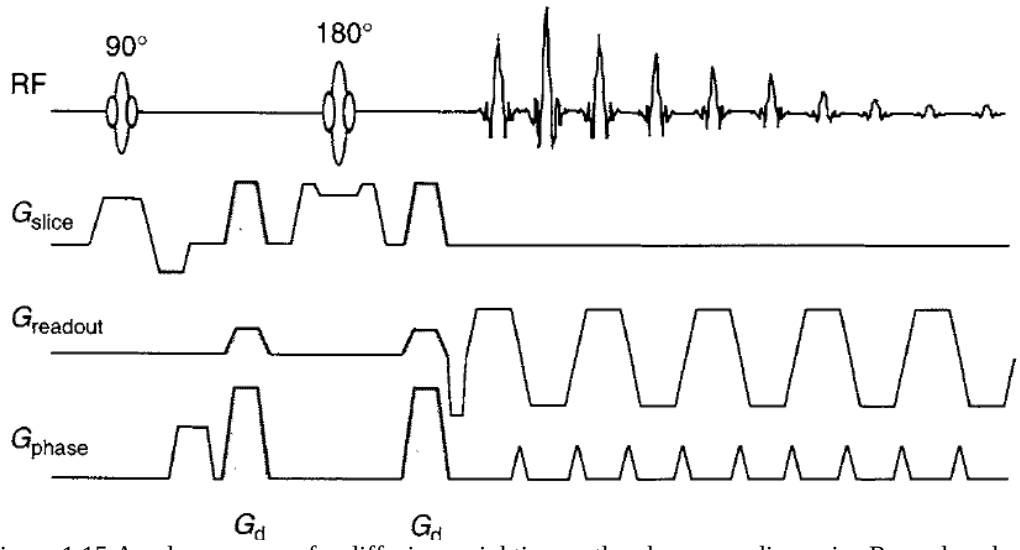

Figure 1.15 A pulse sequence for diffusion weighting on the phase encoding axis. Reproduced from Bernstein with permission (1)

phase is reversed. The imparted phase is determined by the position of the water molecule from the isocenter. Therefore, a spin that is stationary will experience no phase change following the bipolar gradient. Spins the move from position r_1 to position r_2 will experience a phase change, $\Delta\phi$, is calculated as:

$$\Delta\phi = \gamma G\delta(r_2 - r_1) \quad [1.36]$$

where G is the gradient strength and δ is the gradient duration. The signal intensity from the above sequence is given by:

$$M = M_o e^{-bADC} = M_o e^{-\gamma^2 G^2 \delta^2 t_{diff} ADC} \quad [1.37]$$

where b is dependent on γ, G, δ, and the time difference between the applications of the gradients, t_{diff}. By changing the value of b over a number of repetitions of the sequence, the value for D can be determined for each axis of interest.

1.1.10.3 Continuous Arterial Spin Labeling

Blood flow to an organ can be measured by magnetically labeling the spins of the inflowing blood. Generally, this technique has been referred to as arterial spin labeling. Many variations of the arterial spin labeling technique have been proposed. The experiments in this dissertation utilize the continuous arterial spin labeling (CASL) technique. In this technique, two coils are utilized. The first coil is used for imaging the organ of interest while the second is used to invert inflowing blood. In perfused tissue, the inverted blood causes a decrease in the voxel intensity. A subtraction of an image with inversion and one without (control) is related to the blood flow. Assuming a rapid transit time from the tagging plane to the imaging plane, the blood flow can be calculated as

$$\frac{2\alpha\left(\frac{M_o}{\lambda}\right)\gamma {T_1}'}{\Delta M \rho} \quad [1.38]$$

where ρ is the density of the tissue, α is the inversion efficiency, M_o is the initial magnetization, ΔM is the change in signal between the inverted image and the control image, and ${T_1}'$ is the measured longitudinal relaxation time (1).

Blood is inverted through Flow-Induced Adiabatic Inversion. This technique utilizes an RF pulse and a gradient. The gradient induces a frequency offset as a function of time, Δw(t), of the incoming spins from the carrier frequency as a function of position, r(t), as a function of time. The relationship between Δw(t) and r(t) is given by

$$\Delta w(t) = \gamma G[r(t) - r_o] \quad [1.39]$$

where r_o is the tagging plane. Assuming application of the RF field on the x axis, the effective magnetic field, $\bar{B}_{eff}$, seen by the spins as a function of time is given by:

$$\bar{B}_{eff} = \frac{\hat{z}\Delta w(t)}{\gamma} + \hat{x}A \quad [1.40]$$

where A is the amplitude of the RF pulse. When the spins are in the same plane as the tagging pulse, the $\hat{x}$ axis term dominates and the spins are tipped to the transverse plane. As the spin moves further from the RF pulse, the $\hat{z}$ axis term dominates and the spins are inverted.

CASL has the advantage of being completely non-invasive and does not require the injection of a paramagnetic contrast agent. Further, given information on the inversion efficiency and blood and tissue magnetization, the method can give quantitative results of blood flow. The implementation of CASL, however, has many challenges. Due to the requirement of two separate RF coils for imaging and labeling, two RF transmission channels are necessary. Further, transit delay times in disease (i.e. stroke) cause magnetization decay of the labeled blood, producing an artificially lower blood flow measurement. Finally, the contrast between the labeled and unlabeled images may be small and can result in a low contrast to noise ratio of the blood flow map.

1.2 Hyperpolarized Gas Physics

The following section will discuss hyperpolarized (HP) gas physics and imaging. This section will serve as background for chapter 5 of this dissertation. As mentioned in section 1.1.2, the MRI signal is dependent on the number of nuclei imaged within the sample and the main magnetic field. Standard proton imaging of the lungs has proven to be challenging due to the low concentration of intrinsic water. To ameliorate this issue, MRI has been proposed using either exogenous ^{129}Xe or ^{3}He gas. These nuclei are both spin-1/2 allowing for MR-detectabiliy. At standard temperature and pressure (STP), however, the number of nuclei present in exogenously delivered gas is not high enough to produce a meaningful MR signal at Boltzmann equilibrium(10). The following section will discuss technology that allows for increasing the signal from ^{129}Xe or ^{3}He gas nuclei above the Boltzmann equilibrium by hyperpolarization and the different imaging considerations inherent in gas imaging.

1.2.1 Polarization

The MRI signal is ultimately determined by the difference between the numbers of nuclei in one energy level versus the other. To quantify this, we introduce a term, polarization (P), expressed by

$$P = \frac{\Delta N}{N} \qquad [1.41]$$

At the Boltzmann equilibrium, the value of P can be readily calculated for any spin-1/2 nuclei. By substituting Equation 1.8 and 1.12 into equation 1.41, the Boltzmann (or thermal) equilibrium can be expressed as

$$P_{thermal} = \frac{\gamma \hbar B_o}{2kT} \quad [1.42]$$

Considering the ^{3}He nuclei (γ = 32MHZ/T) at 3.0T main magnetic field strength, the thermal equilibrium polarization is equal to $1.22*10^{-6}$.

1.2.2 The Process of Hyperpolarization

Hyperpolarization allows for the enhancement of $P_{thermal}$ by inducing a polarization outside of the main magnetic field. Two methods of performing hyperpolarization of gas nuclei have been purposed. The first such method is known as the 'Brute Force' technique which describes the method of increasing polarization through the use of strong magnetic fields and low temperatures. Equation 1.42 shows that given these conditions, a large P can be achieved. Following polarization of this type, the nuclei are rapidly warmed. Effective polarization for imaging and spectroscopy experiments can be maintained if the warming period and use is more rapid then the T_1 decay back to thermal equilibrium(11).

The second and more popular method for *in vivo* applications of HP MRI is known as Optical Pumping (OP). Optical pumping is currently performed in two ways: metastable and spin exchange. The method our laboratory utilizes is the spin exchange method which will be described in detail in the next section.

1.2.2.1 Spin Exchange Optical Pumping

Spin exchange optical pumping (SEOP) has been widely used by the MRI community for hyperpolarization of ^{3}He and ^{129}Xe. The first biological application of gas

polarized using this method was performed by Albert et al. who imaged the excised lungs of mice (12). The following section will detail the physics of the SEOP process.

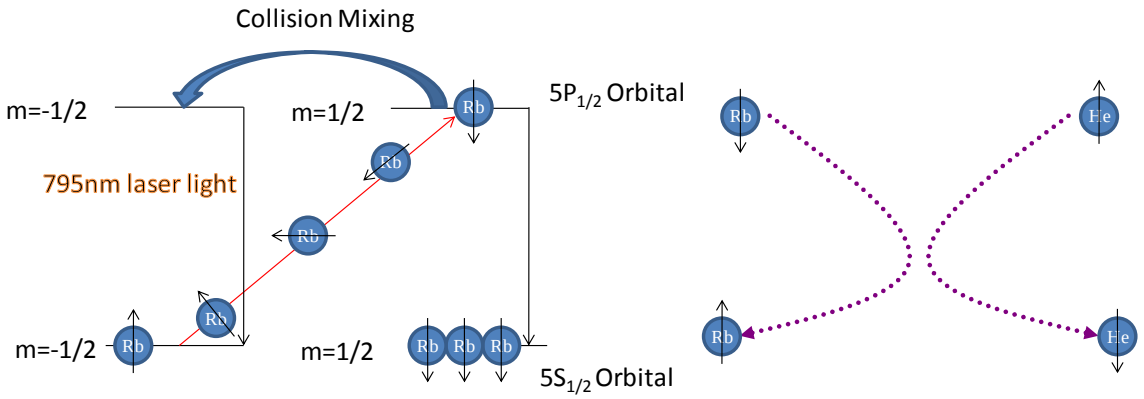

Figure 1.16 Left: The process of optical pumping. Rb $5S_{1/2}$ $m_{1/2}$ valance electrons are excited to the $5P_{1/2}$ m=+1/2 state. The electron can then decay to either the $5S_{1/2}$ m=-1/2 or to the $5S_{1/2}$ m=1/2 state. Right: The process of spin exchange. The m=1/2 electron interacts with the m=-1/2 ^{3}He nucleus. The spin state of the Rb electron and ^{3}He nucleus is exchanged.

Helium gas is pressurized in a glass cell with alkali-metal atoms which is contained within a static magnetic field. The cell is heated to vaporize the alkali-metal. A circularly polarized laser is incident on the cell which causes a transition of the valance electrons of the alkali-metal from the $5S_{1/2}$ m=-1/2 $5S_{1/2}$ orbital to the $5P_{1/2}$ m=+1/2 orbital. In many SEOP experiments, rubidium (Rb) is typically used due to advantageous properties such as high vapor pressure allowing lower temperature use for vaporization and excitation wavelength requirement of ~795 nm which is an available laser wavelength from commercial vendors (13). The valance electron have an equal chance to decay to either $5S_{1/2}$ m=-1/2 or collide with a noble gas or nitrogen gas and switch to the $P_{1/2}$ m=1/2 state which decays to the $5S_{1/2}$ m=+1/2 state. Electrons that have decayed to the $5S_{1/2}$ m=-1/2 state are immediately transitioned to the $5P_{1/2}$ m=+1/2 state by the laser over time causing ~100% of the Rb valance electrons into the $5S_{1/2}$ m=+1/2 state (13).

This process, depicted on the left of Figure 1.16, is known as depopulation optical pumping graphically describes this process. Upon collision between the polarized valance electrons of Rb and the unpolarized ^{3}He nucleus the electron spin polarization of Rb is transferred to the ^{3}He nucleus. As shown on the right side of Figure 1.16, the Rb valance electron returns to the m=-1/2 ground state at which point it is available for re-transitioning to the m=+1/2 excited state. After a time ranging from 12-24 hours for polarization of 1 liter of helium gas, the temperature of the cell is reduced, the alkali metal returns to the solid state and the polarized helium gas is extracted from the cell (13).

1.2.3 Hyperpolarized Gas Magnetic Resonance Imaging Considerations

The MRI considerations for imaging hyperpolarized Helium (HP-He) and other HP nuclei are different than thermally polarized MRI in a number of ways. Of these considerations, the non-renewable nature of the polarization greatly affects image acquisition parameters. Following removal from the glass polarization cell, the gas begins to immediately decay from the HP state to the thermally polarized state. In the absence of impurities, the relaxation rate from the HP to the thermally polarized state is long (on the order of 40 minutes) (14). In the presence of oxygen, however, this rate is greatly increased (15). It is critical, therefore, that oxygen contamination is limited during the transfer process from the polarization cell to the patient and that the transfer happens in short order. The oxygen effect on this relaxation, however, can be exploited for imaging lung physiology, which is the basis for the experiments in chapter 5 (15-17).

Further, RF pulses used for MRI destroy the longitudinal magnetization. For each pulse, the HP longitudinal magnetization is reduced to a level equal to the cosine of the excitation angle. A 90° pulse, for example completely destroys the HP longitudinal magnetization, whereas a 5° flip angle maintains 99.6% of the HP longitudinal magnetization. The RF destruction of the HP longitudinal magnetization has necessitated the need for imaging with very low flip angles (18). Several methods have been proposed to ameliorate this effect on the image SNR and uniformity of k-space sampling. For example, images can be acquired using a centric-reordered k-space sampling scheme to ensure high SNR (18). Further, variable flip angle methods have been developed to more uniformly sample k-space (14,19).

Because of the externally imparted polarization, the signal-to-noise ratio of HP nuclei imaging is almost completely independent of the strength of the main magnetic field. This has opened up possibilities for low magnetic field imaging which may be less costly and more accessible (20,21). Finally, it should be noted that most clinical MRI systems are primarily designed to image only protons. Hardware optimized for non-proton imaging will have to be more readily available for this technology to enjoy widespread use in the clinic.

1.3 MRI Characterization of Experimental Cerebral Ischemia

The following section of this chapter will serve as a background for chapters 3 and 4 of the dissertation. Cerebral ischemia will be discussed including it pathophysiology and treatment regimen. Next, aspects of MRI as they relate to cerebral ischemia will be discussed including diffusion, perfusion, and angiographic imaging.

1.3.1 Pathophyisiology of Cerebral Ischemia

Cerebral ischemia is the result of lack of oxygenation to the brain due to a severe restriction of blood flow caused by either arterial occlusion or vessel damage. Ischemic strokes account for 87% of all stroke cases (22,23). Arterial occlusion can occur due to local cerebral thrombosis or from remote emboli which can block blood flow to the brain. The embolic occlusion typically originates from the chambers of the heart or the carotid artery.

Oxygenation is required for the normal functioning of the mitochondria and the production of the neuronal cell's energy, Adenosine Triphosphate (ATP). Under ischemic conditions, the supply of ATP is quickly depleted and the cell can no long effectively maintain homeostasis. A vital consequence is the inability of the cell to power the ionic pumps that maintain ionic balance (24). The resulting ionic imbalance causes water to move down its osmotic gradient increasing the intracellular volume, resulting in cytotoxic edema.

The amount of damage to the cerebral tissue can be described by the amount of residual cerebral blood flow (CBF) following infarction. With 50% reduction in blood flow, neuronal protein synthesis is reduced and progressively inhibited (CBF

<.55ml/g/min) (25). At lower blood flow, a switch from aerobic to anaerobic metabolism occurs (CBF < .35ml/g/min(25). At progressively more restricted blood flow, energy metabolism is disrupted (CBF < .2ml/g/min) and finally, anoxic depolarization occurs (.15ml/g/min) due to ionic imbalance from inability to maintain the ionic pumps. (25).

The function of neurons also degrades as blood flow is restricted. A large range of thresholds for neuronal inhibition of functional activity exists, ranging from CBF < .25ml/g/min to CBF < .15ml/g/min (25). A non-specific release of neurotransmitters begins to occur at CBF =.2ml/gm/min.

1.3.2 The Ischemic Penumbra

It is interesting to note in the above section that tissue can undergo a functional deficit without necessarily undergoing complete cellular depolarization. Tissue that has only a functional deficit without structural deficit (i.e., cytotoxic edema) may be able to be restored if the blood flow is increased (25). The definition of penumbra is the difference between cerebral tissue that has undergone irreversible cellular damage and tissue that has experienced low blood flow and some cellular functional changes (25-27). The penumbra is potentially salvageable if blood flow to the cerebral tissue was restored through pharmacological or surgical intervention. Typically, the core is in the center of the larger CBF deficit. The penumbral tissue is supported by collateral vessels which allow it to maintain its viability longer then the core tissue.

The practical definition of penumbra is typically made through either MRI or Computed Tomography (CT) imaging. In the case of MRI, the penumbral volume is the difference in volume of tissue that is permanently infarcted, also called the stroke core, as

measured by diffusion weighted imaging (DWI) and the volume of tissue with reduced CBF as measured by perfusion weighted imaging (PWI). DWI is sensitive to the restricted motion of water. Due to the rapid influx of water into the cell corresponding to an ionic imbalance in severely ischemic cerebral tissue, water movement is severely restricted, creating contrast on DWI. In CT, the penumbra is defined by the difference between the CBF deficit and the Cerebral Blood Volume (CBV) deficit (28). Although cerebral tissue may have low CBF, auto regulatory mechanisms in salvageable cerebral tissue enable it to maintain adequate CBV (29). Once the CBV measurement is reduced, the tissue is said to be unsalvageable. The measurement of CT derived CBF and CBV is performed using bolus contrast chasing.

It has been shown in both animal models of stroke and in human disease that cerebral tissue classified as penumbral does not maintain that status through the time course of the disease (7,30). Over time, the penumbral tissue changes to become part of the core (7). The goal of treatment, therefore, is to preserve the tissue in the penumbral area.

1.3.3 Recombinant tissue Plasminogen Activator

Recombinant tissue Plasminogen Activator (r-tPA) is currently the only Food and Drug Administration approved treatment for embolic ischemic stroke. r-tPA works by activating the fibrinolysis pathway to ultimately breakdown the embolus in the cerebral vasculature. r-tPA converts the inactive plasminogen to the active plasmin which ultimately performs the thrombolysis (31). The possibility of hemorrhage must be taken into consideration as it is a potential side effect of treatment.

Guidelines for the administration of r-tPA in light of the hemorrhage risk have been developed and are currently being reevaluated. The European Cooperative Acute Stroke Study (ECASS III) has suggested that the time window for administration of r-tPA should be extended to 4.5 hours following symptom onset (32). Other investigators have indicated that r-tPA administration should be based on imaging findings regardless of the time window (33).

1.3.4 The no-reflow phenomenon

One important aspect of thrombolytic therapy is the 'no-reflow phenomenon' in which microcapillary blood flow is not fully restored even though complete recanalization of the occluded vessel occurs. Microcapillary damage is thought to accompany neuronal damage during ischemia (34). In ischemia, loss of the protective barrier between the blood and the neurons is damaged (34). Further, following ischemia, leukocyte adhesion molecules are expressed (34). Upon recanalization, this leads to recruitment of an immune response which serves to block microcapillary blood-flow (35).

1.3.5 Experimental Rodent Models of Ischemic Stroke

Two models of rat ischemic stroke have become popular in preclinical stroke pathophysiology characterization and treatment experimentation. The first procedure involves threading a suture through the internal carotid artery to the level of the middle cerebral artery, inducing a middle cerebral artery occlusion. In this model, reperfusion can be accomplished through withdrawal of the suture. The second procedure induces a middle cerebral artery occlusion via injection of an *ex vivo* created embolus through the

cerebral vasculature. Reperfusion can be achieved through the injection of a thrombolytic compound.

A comparison of the two models performed by Henninger et al. reveals that the ischemic lesion is larger in the embolic model than the suture model (36). Further, the penumbral volume was larger and persisted longer in the embolic model (36). Finally, the embolic model produced more heterogeneous ischemic lesion volume than the suture model (36).

1.3.6 MRI of Experimental Cerebral Ischemia

Magnetic Resonance Imaging (MRI) of preclinical ischemic stroke in rats has been used to ascertain the response of brain tissue to recanalization by r-tPA and other thrombolytic compounds (37,38). The following section discusses the methods available for assessing the penumbral volume and determining the status of large vessel blood flow.

1.3.6.1 Diffusion Weighted Imaging

As mentioned earlier DWI is sensitive to infarcted cerebral tissue that has undergone electrical dysfunction and shifting of water from the extracellular to intracellular space. Much work has been performed in small animals to characterize the time course of volume changes of stroke core tissue. Much of that work has focused on characterizing the response of the stroke core to treatment. For example, in determining the efficacy of administration of r-tPA at different time points, Jiang et al. showed that treatment at 1 hour produced significantly lower infarct volumes in the treated groups as defined by DWI (39). Further, it has been shown through DWI that certain treatments can

halt the transformation of penumbral tissue into infarcted tissue. Bråtane et al., for example, showed that administration of granulocyte-colony stimulating factor during embolic stroke freezes the increase of permanently infarcted tissue volume (30).

In order to facilitate quantitative analysis of permanently infarcted tissue, a threshold for infarction based on the ADC value was derived. As described in earlier sections, the ADC quantifies motion of water based on DWI images. In experimental rat stroke, Meng et al. defined permanently infarcted tissue as tissue in which the ADC falls below $.53*10^{-3}mm^2/sec$ (40). This threshold has been used in subsequent experimentation and is well validated (30,36,37).

1.3.6.2 Perfusion Weighted Imaging

MRI based PWI is a method in which CBF can be calculated. CBF can be determined through two techniques, Arterial Spin Labeling (ASL) and Dynamic Susceptibility Contrast (DSC). The applications of these techniques to small animals will be discussed below.

1.3.6.2.1 Arterial Spin Labeling

Arterial Spin Labeling (ASL) is a PWI technique in which the inflowing blood is magnetically labeled using RF pulses. In small animals, much work has been performed using the continuous arterial spin labeling technique (CASL) which has been described in earlier sections of this chapter. CASL has been used extensively in experimental stroke imaging for definition of volume of tissue that experienced reduced CBF. Meng et al. determined that through the use of CASL, CBF must be less then .3ml/g/min in order for

the tissue to be considered ischemic (40). During rat permanent experimental ischemic stroke, the ischemic volume remains constant if not treated (41). The ischemic lesion volume as defined by CASL is rapidly reduced in the a suture reperfusion model of ischemic stroke (40). In the embolic model of ischemic stroke, r-tPA causes a slower reduction of the ischemic lesion (37).

1.3.6.2.2 Dynamic Susceptibility Contrast

Dynamic Susceptibility Contrast (DSC) is a method of measuring CBF through the injection of a para- or ferro-magnetic contrast agent and observing the changes in the signal intensity derived from T_2* weighted imaging. Typically, a gradient-echo, echo-planar imaging sequence is used to allow for high temporal sampling during the bolus transit. The use of DSC has been utilized extensively in the literature (42-44). As compared to ASL, DSC is straight forward to implement, however, the measurement cannot be repeated in rapid succession due to the need for exogenously delivered contrast agents. Finally, threshold characterization of DSC derived relative CBF values for ischemia has not been performed.

1.3.6.3 Time of Flight Angiography

Time of Flight (TOF) angiography has been used to characterize the patency of major cerebral blood vessels in the brain. A high flip angle, short recovery time, short echo time pulse sequence is used to saturate the longitudinal magnetization of stationary tissue. Flowing spins, such as those in the blood, are not saturated and produce large transverse magnetization upon excitation. Thus, stationary tissue produces little signal while flowing

blood produces high signal. The application of TOF to the study of experimental stroke treatment has been rare. Hilger et al. has used TOF angiography to characterize reperfusion in an experimental rat stroke model (45). TOF produces excellent vessel/tissue contrast in areas of high, non-complex flow but may inaccurately characterize vessel patency if these conditions are not met. Both complex and low flow may increase the blood saturation due to the RF pulses causing a reduction in blood contrast.

1.4 Pulmonary Vascular Function

The following section will describe vascular physiology in the lungs and the effects of pulmonary ischemia and alveolar hypoxia. MRI techniques used for quantitative imaging of pulmonary vascular function will be discussed along with their adaptations for preclinical imaging. This section will serve as background for chapter 5 and 6.

1.4.1 Pulmonary Vasculature

The major pulmonary artery (PA) is supplied directly from the right ventricle of the heart. Major pulmonary arteries are characterized by their elastic properties to accommodate varying blood flow with a corresponding changes in pressure (46). This maintains the low pressure of the system. The major artery branches into smaller arterioles. These arterioles contain smooth muscle which undergo thinning as the vessels branch off closer to alveolar sacs (47). The arterioles feed capillaries which are fused to the surface of the alveolar sacs (47). The capillary interstitial space can be characterized as being either thin or thick (47). The thick interstitial space contains collagen fibers and other cellular elements such as fibroblasts and immune cells (47). Capillaries become venules which are similar in structure to the pulmonary arterioles (47). Finally, the venules branch away from areas of respiration into larger veins and eventually into the left atrium of the heart (47).

1.4.2 Alveolar Gas Exchange

Oxygenation of the blood is the primary function of the lung. The process of oxygenation of the blood involves two steps: 1.) transfer of the gas from the atmosphere to the alveoli, the site of gas exchange, and 2.) transfer of the gas from the lungs to the

blood. This process therefore involves both ventilation of gas and blood perfusion to the alveolar units.

The conductance of the air from the atmosphere to the alveoli is performed by branching airways which terminate at gas exchanging units known as alveoli. Gas exchange begins to occur 2-5 branches prior to the terminating alveolar sac (48). The alveolar wall is typically extremely thin and consists of an epithelium lining, a basement membrane, and an endothelial lining of a capillary. The thin wall is critical for efficient gas exchange from the air spaces to the blood (48).

Oxygen diffusion from the airspaces to the blood is a passive process determined by concentration gradients between the airspaces and the blood. In the 'ideal' scenario for efficient gas exchange a higher partial pressure of oxygen exists in the lung airspace, while a lower partial pressure of carbon dioxide exists in the blood. In this situation, oxygen diffuses into the blood and carbon dioxide diffuses into the airspace. A scenario may also exist in which the airspace has an equal or lower partial pressure of oxygen then that in the blood. In this situation, known as a shunt, no transfer of oxygen occurs. A final scenario may exist if no blood is flowing to the alveolar units which causes an increase in the partial pressure of oxygen in the effected airspace (49).

1.4.3 Hypoxic Pulmonary Vasoconstriction

The main function of the pulmonary vasculature is to match well ventilated areas of the lung with perfusion. A well studied phenomenon of the lung vasculature, known as hypoxic pulmonary vasoconstriction (HPV), constricts vessels to areas of lung in the condition of low alveolar partial pressure of oxygen (50). HPV plays an important role in

normal pulmonary function and in pulmonary disease. One of the most clinically prevalent examples of HPV occurs when patients expose themselves to areas of high altitude in which the partial pressure of oxygen in the atmosphere is reduced (51). HPV also occurs in obstructive diseases such as Chronic Obstructive Pulmonary Disease (COPD) and asthma. In these cases, areas of the lungs have reduced ventilation leading to regional reduction of the alveolar partial pressure of oxygen. In severe cases of COPD, HPV leads to chronic pulmonary hypertension which ultimately affects cardiac function (52-54). In a final example, HPV is an important consideration in the management of anesthesia. Specifically, patients often require single lung ventilation for the purposes of performing surgery which would be made difficult by the motion of the non-ventilated lung. Single lung ventilation results in a severe reduction of the partial pressure of oxygen to the alveoli units of the non-ventilated lung resulting in localized HPV. Certain anesthetic regiments ameliorate the HPV response, causing a shunt condition and ultimately hypoxemia (55,56).

The site and molecular mechanisms underlying HPV are complex and not well understood. Current research indicates that the site of HPV occurs at the small pre-capillary arterioles with some constriction occurring in the veins (57). It is currently thought that mitochondria housed within PA smooth muscle cells initiate a molecular response ultimately resulting in vasoconstriction (50). The molecular response is thought to be initiated by an increase in mitochondria reactive oxygen species (ROS) production, ultimately resulting in the activation of potassium membrane pumps and an increase in

intracellular concentrations of calcium, causing muscle depolarization and contraction (50,57,58).

The long term effects of acute pulmonary hypoxia on pulmonary parenchyma are minimal. Edema formation has been shown to occur only after 24 hours of hypoxic exposure (59). Further, protein leak, a common occurrence in pulmonary vascular disease, is present only after exposure greater than 24 hours (59). Chronic hypoxia is associated with remodeling of the pulmonary arterioles and an inflammatory response (60,61). It is also interesting to note that during generalized hypoxia, such as seen at high altitudes, cardiac stroke work and carotid blood flow has been shown to increase owing to the increase in pulmonary vascular resistance (62).

1.4.4 Pulmonary Embolism

Pulmonary ischemia can occur as a result of an embolism which typically originates from thrombi in the extremities. The thrombi become dislodged and travel through the venous system ultimately lodging in the pulmonary arterial system. There are six hundred thousand new cases of pulmonary ischemia due to pulmonary embolism (PE) in the United States each year (63).

PE can lead to a number of complications and has a high mortality rate when left untreated (63). PA occlusion results in high pulmonary circulation pressure. Increased PA pressure causes stress on the right ventricle which ultimately can lead to cardiac failure (64). Further, an immune response to PE has been shown in rat experimental models. Following one day of ischemia, neutrophils have been found in the right ventricle of the heart. During longer periods of embolism, macrophages have been localized to the right

ventricle (65,66). Ultimately, the presence of right ventricular dysfunction associated with PE results in poor clinical outcomes (64).

PE does not cause pulmonary tissue damage as seen in other organs during ischemic disease, but does affect the lung's ventilatory processes. Pulmonary parenchymal tissue oxygenation is provided alternatively by the bronchial circulation and by the airways (46). In experimental models of PE, an increase in airway resistance and a decrease in pulmonary compliance have been shown (46).

Treatment focuses on preventing future pulmonary thromboembolic events and not on the treatment of the acute PE except in cases of massive PE . Oxygen administration, anticoagulant therapy, and bed rest are standard treatments for non-massive PE (64). Treatment can also include placement of a filter within the abdominal vena cava to prevent future emboli (64,67). Massive PE requires aggressive treatment including administration of thrombolytic therapy or mechanical embolus retrieval (68,69).

1.4.5 Rodent Pulmonary Functional Vascular Imaging

Quantification of pulmonary vascular functionality through imaging is important in clinical imaging of pulmonary disease. In the diagnosis of PE, for example, Single Photon Emission Computed Tomography (SPECT) is used to measure the capillary blood perfusion to lung tissue (70). In coordination with a SPECT pulmonary ventilation exam, a diagnosis of PE can be considered (64). Computed Tomography (CT) has emerged as the imaging modality of choice for visualization of the patency of the pulmonary arteries (71). MRI perfusion contrast bolus tracking has been used to quantify capillary blood

flow to the lungs and its usefulness in performing angiography has been demonstrated (72,73).

Unfortunately, the advances in human pulmonary imaging have not translated into viable methodology for measuring pulmonary vascular function in rodents. Performing standard clinical imaging techniques for measuring pulmonary vascular function in rodents is made difficult by the necessity of high spatial and temporal resolution and by the faster rodent cardiac and respiratory rate. Development of techniques to measure pulmonary vascular function in rodents is important for studies of physiology, disease pathophysiology, and drug discovery. The following section describes attempts using various imaging modalities to measure pulmonary vascular function in rodents.

1.4.5.1 Micro-CT

Micro-CT operates on the same principle as clinically available CT imaging systems. The spatial resolution is sufficient to perform very detailed imaging of rodent anatomy. However, the temporal resolution is insufficiently high to perform standard contrast bolus tracking for angiography or blood perfusion measurements in rodents (74,75). Although there has not been much work in adapting micro-CT for rodent perfusion or angiography, Badea et al. introduced a method of staggered delivery of contrast agents for high spatial and temporal measurements of bolus perfusion (75).

1.4.5.2 SPECT Perfusion Imaging

In the clinic, perfusion imaging utilizing SPECT is performed using a long clearance radiotracer. Accumulation of the tracer in the capillaries of the organ of interest

indicates blood flow (70). Because of the steady state nature of this imaging protocol it is more readily translatable to imaging of small animals. Wietholt et al. introduced a SPECT system for small animal imaging and applied it to pulmonary perfusion imaging (76,77). Despite some success, the application of small animal SPECT to pulmonary perfusion imaging has been limited in the literature. Further, steady state SPECT perfusion imaging is semi-quantitative, making longitudinal studies difficult.

1.4.5.3 Magnetic Resonance Imaging

Proton MRI of pulmonary vascular function is hindered by low proton density, areas of high susceptibility resulting in very short T2* relaxation times, and cardiac and respiratory motion (78). These problems in rodents are amplified by the need for higher spatial and temporal resolution and by the increased cardiac and respiratory rate. Nonetheless, proton lung imaging methods have been developed for blood perfusion imaging of rodent lungs. Further, much work has been performed using HP gas imaging to measure vascular function.

1.4.5.3.1 Proton MRI Techniques

Proton MRI techniques of measuring pulmonary vascular function can be separated into two categories: steady state and dynamic imaging. The first, steady state imaging, involves injection of an intravascular contrast agent and measuring changes in the signal intensity of a T_1 weighted image due to the contrast agent. The contrast agent used in many studies has been gadolinium-based and has typically consisted of a large molecular weight poly-l-lysine which has a slow rate of clearance and very little

extravascularization (79). These imaging protocols are very similar to SPECT perfusion scanning described previously. Spin echo with cardiac and respiratory gating or short echo time, and gradient echo projection-reconstruction imaging have been used to ameliorate the susceptibility issues inherent to lung tissue (79,80). The T_1 signal intensity changes seen following contrast injection are based on a number of factors and cannot therefore result in a quantifiable measurement of vascular function.

Little work has been performed in dynamic imaging of vascular function using MRI due to the interference of cardiac and respiratory motion. This measurement consists of injection of a gadolinium chelate while performing fast gradient echo T_1 weighted imaging. The change in the signal intensity can be used to calculate pulmonary blood flow (PBF), pulmonary blood volume (PBV) and bolus mean transit time (MTT). Mistry et al. utilized scattered administrations of contrast agent following the detection of a cardiac R-wave similar to that adapted for micro-CT vascular imaging (81,82).

1.4.5.3.2 Hyperpolarized Gas MRI Techniques

HP-He can be administered to an animal and indicates areas of the lungs that are well ventilated. HP-He gas can also be used to indirectly detect pulmonary vascular functionality through the injection of contrast agent or through the monitoring of signal decay via oxygen relaxation (15-17,83-85). Both methods of imaging will be discussed below.

Similar to proton MRI, interaction of HP-He with paramagnetic or ferromagnetic species hastens its transverse relaxation time. Due to the small distance between the capillary lumen and the alveolar airspace, injection of a paramagnetic or ferromagnetic

contrast agent will cause a reduction of the transverse relaxation time (85). This phenomenon can be used in a similar manner as that descried previously for proton MRI. Viallon et al. performed HP-He dynamic breath hold imaging while simultaneously injecting a ferromagnetic contrast agent (86). Following correction for flip angle HP magnetization destruction, the PBV was calculated. In a second application of perfusion imaging using HP gas and the injection of a contrast agent for perfusion quantification, the phase change of the HP-He signal was measured due to the presence of a paramagnetic contrast agent localized in the capillary network of the lung (85). The magnitude of the phase change is related to the concentration of the paramagnetic contrast agent present. These methods have the advantage of allowing for simultaneous ventilation and perfusion imaging.

In a second technique, the relationship between oxygen content and the rate of HP-He magnetization destruction can be utilized to measure the ability of the lungs to oxygenate the blood (15-17,83,84,87,88). During a breath hold, oxygen is continuously being up taken by the lungs in areas of normal perfusion. In areas of abnormal perfusion, oxygen remains in the airspace. A breath hold with both oxygen and HP-He results in destruction of the hyperpolarized magnetization proportional to the concentration of oxygen in the lungs (16). As oxygen leaves the air spaces, the rate of magnetization destruction is reduced. Accounting for RF flip angle magnetization destruction allows for the measurement of the initial partial pressure of oxygen and the oxygen uptake rate in the lungs. This methodology has been applied to a number of species and animal models

of disease (16,83,84). The details of the imaging protocol for this measurement is described in detail in chapter 5 of this dissertation.

Chapter II: Gadolinium Based Contrast Perfusion Compared to Continuous Arterial Spin Labeling for Perfusion Lesion Determination

Bernt t. Bråtane[1], Ronn P. Walvick[1], Claire Corot, Eric Lancelot, Marc Fisher

From the Department of Radiology (R.P.W) and Neurology(B.T.B, M. F), University of Massachusetts Medical School, Worcester, MA 01604 and Guebert(C. C, E. L) Roissy Charles-de-Gaulle Cedex, France.

Published in Journal of Cerebral Blood Flow and Metabolism February 2010

1 Authors contributed equally to work

2.1 Preface

In this work, we compare the definition of the ischemic lesion in rats using two Magnetic Resonance Imaging (MRI) methods: Dynamic Susceptibility Contrast (DSC) and Continuous Arterial Spin Labeling (CASL). We derived a threshold for ischemia as defined by DSC and used this threshold to make volumetric measurements of the ischemic lesion. The volume of this lesion was compared to the lesion volume as defined by ASL. Further, we analyzed the cerebral blood flow (CBF) time course in different ischemic stroke regions. My contributions to this work include experimental design, collecting and analyzing MRI data, and co-principle authorship of the manuscript.

2.2 Acknowledgements

This work was supported by a grant from Oseo ISEULT / INUMAC French / German project and a research grant from Guerbet. Two authors (CC and EL) are employees of Guerbet.

2.3 Abstract

Perfusion imaging is critical in imaging of ischemic stroke to determine "tissue at risk" for infarction. In this study we compared the volumetric quantification of the perfusion deficit in two rat middle cerebral artery occlusion (MCAO) models utilizing two gadolinium based contrast agents (P1152, Guerbet and Magnevist®, Bayer-Schering) compared to our well established continuous arterial spin labeling (CASL) perfusion imaging technique. Animals underwent either permanent MCAO or transient MCAO with 80 minute reperfusion. Imaging was performed at four different time points post-MCAO. A region of interest (ROI) analysis of subregions of the ischemic zone (core, penumbra, transient reversal (TR) and sustained reversal (SR)) utilizing P1152 showed a significant reduction in blood flow in the core and TR subregions relative to the penumbral and SR subregions while occluded. After reperfusion a significant increase in blood flow was recorded at all time points post-reperfusion in all regions except TR. From the ROI analysis the threshold for penumbra was determined to be -62±11% and this value was subsequently used for quantification of the volumetric deficit. The ischemic volume as defined by dynamic susceptibility contrast (DSC) was only statistically different from the CASL derived ischemic volume when using Magnevist® at post reperfusion time points.

2.4 Introduction

With Magnetic Resonance Imaging (MRI), the ischemic penumbra can be approximated as the mismatch between the volume of the perfusion deficit and the volume of ischemic tissue injury as measured by Apparent Diffusion Coefficient (ADC) mapping (40,89). The characterization of this mismatch has implications clinically for identifying patients who might respond to acute therapies (90). Preclinical models of ischemic stroke in rats have shown that areas of penumbra ultimately are destined to become infarcted tissue without intervention (36,43,89).

The perfusion deficit can be characterized by using a number of different methodological approaches. In one approach, an exogenous contrast agent, typically Gadolinium based, is injected intravenously (i.v.) and flows through the capillary system of the brain parenchyma (91). The presence of the agent causes a concentration-based change in both the longitudinal and transverse relaxation rates. Commonly, a dynamic single shot gradient echo sequence is performed to measure the contrast induced magnetic susceptibility (T2*) changes over time, which has been termed dynamic susceptibility contrast (DSC). This data can be used to define cerebral blood volume (CBV) and mean transit time (MTT), which can be combined to construct the cerebral blood flow (CBF) as a function of voxel position (92). Quantification of the parameters is only possible when an arterial input function can be measured (93).

In a second approach, the proton spins in the blood are magnetically labeled with a technique known as arterial spin labeling (ASL) (94). In the typical ASL imaging

sequence, the flowing spins in the blood are inverted or saturated. The contrast is produced as the magnetically labeled spins replace unlabeled spins in the cerebral vasculature, typically causing a reduction of signal in the areas of blood flow. This image is then subtracted from a control image in which labeling of the blood has not occurred. While a variety of methods exist to perform ASL, continuous ASL (CASL) has been shown by our group to accurately map the ischemic lesion (36,37,40,89). Preclinically, both contrast and ASL based MR perfusion measurements are used. Although thresholds have been derived to determine hypoperfused tissue for the CASL perfusion method, minimal work has been performed to derive such a threshold for the contrast enhanced perfusion method (41). Further, a comparison of the two methods for determining regions of hypoperfusion has not been performed. Therefore, in this study we examined perfusion deficits in permanent (pMCAO) and transient (tMCAO) middle cerebral artery occlusion models in rats using both the contrast enhanced and CASL methods of perfusion MRI. Changes in cerebral blood flow in ischemic stroke subregions as well as volumetric analysis of the perfusion deficit were determined. Based on CASL perfusion measurements, ADC mapping, and histology, we derived a contrast perfusion based threshold for identifying tissue at risk for ischemia and we further characterized relative cerebral blood flow (rCBF) values in ischemic subregions. In this work, we hypothesize that 1.) The temporal evolution of the rCBF is different in each stroke sub-region as characterized by DSC, 2.) A threshold for ischemia using DSC can be derived, and 3.) the volume of the ischemic deficit as determined by DSC is similar to that determined by CASL.

2.5 Methods

All procedures used in this study were performed in accordance with our institutional guidelines. Spontaneously breathing male Wistar rats (n=20, Taconic Farms, Hudson, NY, USA) weighing 300±30g were anesthetized with isoflurane (5% for induction, 2% for surgery, 1.2% for maintenance) in room air. PE-50 polyethylene tubing was inserted into the femoral artery and vein. The femoral artery was used for monitoring the mean arterial blood pressure (MABP) and blood gases (pH, PaO2, PaCO2), electrolytes (Na+, K+, Ca2+), and plasma glucose levels. The femoral vein was used for i.v. bolus injection of the contrast agent. Body temperature was monitored continuously with a rectal probe and maintained at 37.0±0.3 °C with a thermostatically controlled heating pad.

2.5.1 Middle cerebral artery occlusion

Suture MCAO was performed as previously described in detail (95). Ten animals were subject to pMCAO using 4-0 silicone-coated nylon filament sutures, and ten to tMCAO using the in-bore reperfusion technique where the rats were mechanically reperfused by withdrawing the occluder at 80 minutes after MCAO while the animal was in the magnet (44). On the day of the experiment, rats were randomly assigned to receive either temporary or permanent MCAO. Further, data analysis was performed by an author blinded to the occlusion type and time point.

2.5.2 DSC properties

In this study, P1152 (Guerbet) and Magnevist® (Bayer-Schering) were utilized for DSC measurements. P1152 (Guerbet) is an investigational small molecular weight Gd

chelate compound with r_1 longitudinal and r_2 transverse relaxivities of 11.7 and 13.8 $mM^{-1}s^{-1}$ in water at 0.5 T, respectively. These values are significantly higher than those reported for conventional Gd chelates such as Gd-DTPA (Magnevist®) or Gd-DOTA (Dotarem®) (96). P1152 does not display any protein binding and shows a similar pharmacokinetic profile as Dotarem® in anaesthetized rats with a blood half-life of 50 ± 7 vs. 38 ± 2 min, a blood clearance of 6.9 ± 0.6 vs. 8.4 ± 0.8 ml/min/kg and a distribution volume of 322 ± 27 vs. 293 ± 6 ml/kg for both contrast agents respectively (unpublished Guerbet data). Magnevist and Dotarem are standard gadolinium chelates with comparable blood pharmacokinetics (97,98).

2.5.3 Experimental protocol

All 20 rats were imaged at the same time points (30, 60, 90, 120, 150, 180 and 210 minutes) after MCAO. ADC and CBF maps derived from CASL were recorded at each imaging time point. For DSC, a contrast agent (P1152) was injected over ~1 sec at a dose of 0.1 mmol/kg followed by a saline bolus chaser (n = 12). DSC data were acquired every hour starting at 30 minutes (30, 90, 150 and 210 minutes). DSC data were also acquired in a subgroup of animals using Magnevist® at a dose of 0.1mmol/kg (n = 8). At 24 h post-MCAO, brains were removed and sectioned coronally into seven 1.5 mm thick slices corresponding to the MR slices and stained with a 2% solution of 2,3,5-triphenyltetrazoliumchloride (TTC) for 20 minutes at 37°. All histological analyses were conducted by an author who was blinded to the experimental protocol.

2.5.4 MRI measurements

MRI experiments were performed on a 4.7 T/400 mm horizontal magnet equipped with a Biospec Bruker console (Billerica, MA), and a 2.0 G/mm gradient insert (inner diameter = 120 mm, rise time = 120 μs rise time). A surface coil (inner diameter = 23 mm) was used for brain imaging with an actively decoupled butterfly neck coil for carotid blood spin labeling. Three diffusion-weighted images were separately acquired with diffusion-sensitive gradients applied along the x, y, or z direction. Single shot, spin echo echo-planar images were acquired over 2.5 minutes with matrix = 64 x 64, spectral width 200 kHz, TR 2 s (90° flip-angle), TE 37.5 ms, b = 8 and 1,300 s/mm2, Δ = 24 ms, δ = 4.75 ms, field of view 25.6 x 25.6 mm, seven 1.5 mm slices, and 16 averages. The total acquisition time was 2 minutes and 4 seconds.

Quantitative CBF measurements were made using the CASL technique with single-shot, gradient-echo, echo-planar images acquisition. Sixty paired images (for signal averaging) were acquired over 4 minutes, alternately; one with and the other (control) without spin labeling preparation. The MRI parameters were similar to ADC measurements except TE = 13.5 ms. The labeling pulse utilized a 1.78-second, square radiofrequency pulse in the presence of 1.0 Gauss/cm gradient along the flow direction. The sign of the frequency offset was switched for non-labeled images. DSC measurements were performed using an echo planar gradient echo imaging sequence with a TR of 1 s, TE of 15 ms, and flip angle of 90°. The field of view was 25.6 mm x 25.6 mm with a matrix size of 64 x 64. Ten dummy scans were conducted to reach a steady

state and contrast injection occurred after 25 acquisitions The total acquisition time was 1.5 minutes.

2.5.5 ADC and Quantitative CBF Mapping

Diffusion weighted and CASL perfusion images were analyzed using QuickVol II (http://www.quickvol.com/). Quantitative CBF and ADC maps and their corresponding threshold-derived lesion volumes were calculated as described previously (41). Assuming a blood-brain partition coefficient, λ, of .9, tissue T_1 of 1.5 seconds, and inversion efficiency, α, of .75 the blood flow in terms of ml/g/tissue can be calculated by:

$$CBF = \frac{\lambda(S_c - S_L)}{T_1(S_L + (2\alpha - 1)S_c)} \quad [2.1]$$

where S_c and S_L are the control and labeled images, respectively. ADC maps were calculated through the methods described in section 1.1.10.2.

The thresholds used to define respective abnormal ADC and CBF regions were a reduction to 0.53 x 10^{-3} mm^2/s and reduction of 57 ± 11% respectively (41). ADC and CBF data that met that threshold were considered infarcted and ischemic, respectively.

2.5.6 Derivation of regions of interest

Four subregions in the ischemic zone were investigated. To locate these regions, ADC and CASL maps were compared to 24 h histology by coregistration of the imaging derived pixels on the corresponding TTC pixels. The ischemic core was defined as abnormal by the previously determined threshold on the ADC maps and infarcted tissue on the 24h histology. The penumbra was defined as abnormal on the CASL map using

the previously determined threshold but was not abnormal on the ADC map at 30 min post MCAO. Transient and sustained recovery (TR and SR) were both regions with a deficit on the ADC map at 30 min, but with normalization of that region on the ADC map after reperfusion. In the SR region the 24 h histology did not show infarction whereas in the TR region the 24 h histology did show infarction. TR and SR were only found in the tMCAO group. A graphical description of the four regions of interest (ROI) is given in Figure 2.1. The ROIs were manually outlined based on the criteria described in this paragraphy using QuickVol II.

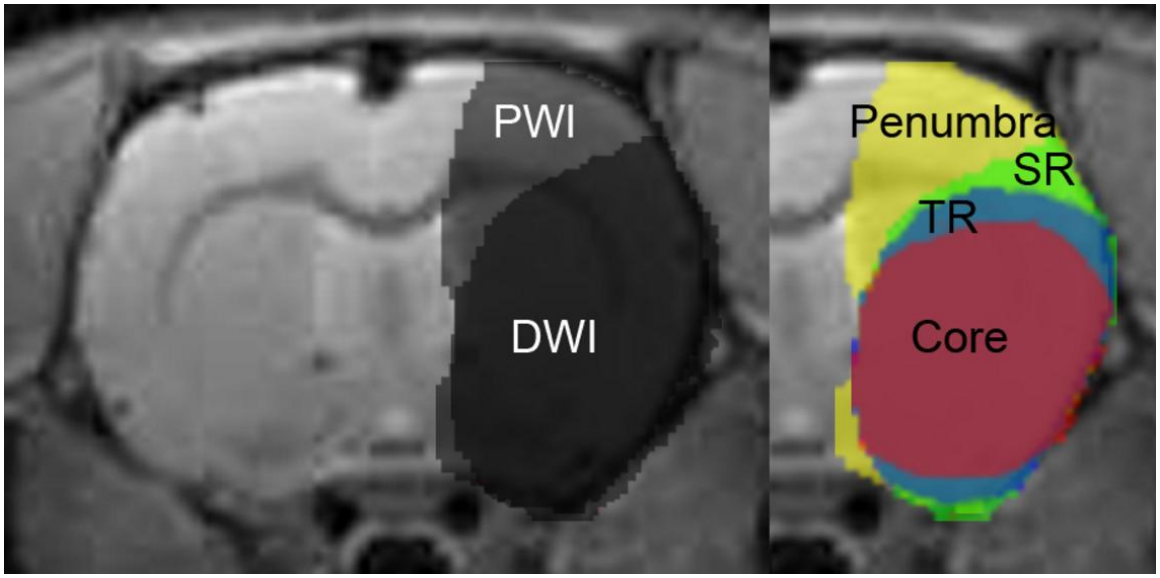

Figure 2.1 Schematic representation of subregions within an ischemic stroke. CBF deficits represent the total region that will be infarcted at 24h with no intervention. ADC deficits represent regions that are affected early after MCAO. The mismatch between CBF and ADC is referred to as ischemic penumbra (yellow). Sustained Recovery (SR, green) is the part of this recovery that ended up as healthy tissue on histology at 24h in contrast to Transient Recovery (TR, blue) that was incorporated in the ischemic stroke at 24h histology. Core (red) is the diffusion lesion that did not reverse with intervention.

2.5.7 Derivation of rCBF from DSC Data

Curves from contrast enhanced perfusion images and ROI data were fit to a modified gamma variate which allows for simplified fitting of first pass data implemented using Matlab (Mathworks, Natick, MA) software (99). Briefly, the first pass of a bolus contrast can be described as a gamma variate function given as

$$C(t) = A(t^{\alpha})e^{-\frac{t}{\beta}} \qquad [2.2]$$

where α and β are shape and scale parameters and A is the amplitude of the change in bolus concentration (99). While fitting DSC to this equation can be performed using non-linear techniques, Madsen describes a method in which the equation can be linearized to

allow for more simplified fitting (99). The gamma variate fit allowed for determination of the relative cerebral blood volume (rCBV), relative mean transit time (rMTT), which were used to construct the rCBF maps as

$$rCBF = \frac{rCBV}{rMTT} = \frac{\int \Delta R_2{}^* dt}{\int \Delta R_2{}^* t dt} \quad [2.3]$$

where $\Delta R_2{}^*$ is the change in transverse relaxation rate and t is the time following bolus arrival. The term relative indicates that deconvolution with an arterial input function was not performed (93). rCBF values were reported as percent changes in rCBF between the ipsi- and contralateral regions as previously described (92). A threshold for ischemic tissue was derived by averaging the rCBF in the penumbral area at all time points in the pMCAO group and at the 30 min time point in the tMCAO group. Volumetric analysis of the rCBF based perfusion deficit was identified by a combination of the derived threshold and visual inspection.

2.5.8 Statistical analysis

Data are presented as mean ± standard deviation unless stated otherwise. Statistical comparisons were performed using ANOVA with *post hoc* Bonferroni test, Mann-Whitney U, and Wilcoxon Signed Ranks Test, where appropriate. Calculations were performed using SPSS (v15.0, Chicago, USA). $P<0.05$ was considered significant.

2.6 Results

There were no between group differences in regard to physiological parameters (MABP, blood gases, electrolytes) (Appendix I). To illustrate a typical pMCAO and tMCAO animal, representative images of each image modality (ADC, CASL, and DSC) and histology are presented in Figure 2.2.

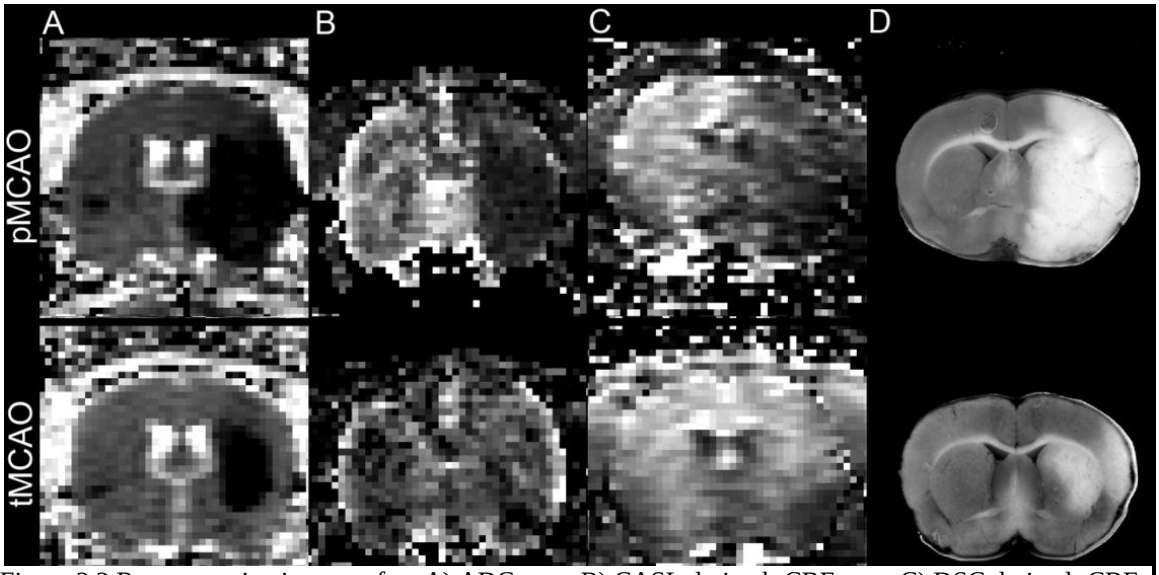

Figure 2.2 Representative images of an A) ADC map, B) CASL derived rCBF map, C) DSC derived rCBF map, and D) TTC in a pMCAO (top row) and tMCAO (bottom row) model of ischemic stroke. Note that the perfusion-weighted image in the tMCAO model was recorded post reperfusion. All MR images were recorded 90 minutes post MCAO and TTC was performed at 24 hours post MCAO.

2.6.1 Region of interest analysis

A ROI analysis was performed in order to characterize the temporal changes in the ischemic subregions (core, penumbra, TR and SR). Based on the DSC imaging with the contrast agents rCBF data were derived from each of the subregions (see Figure 2.3). In animals subjected to pMCAO, rCBF in the ischemic core and penumbra was depressed. This observation persisted over all time points. In the tMCAO group,

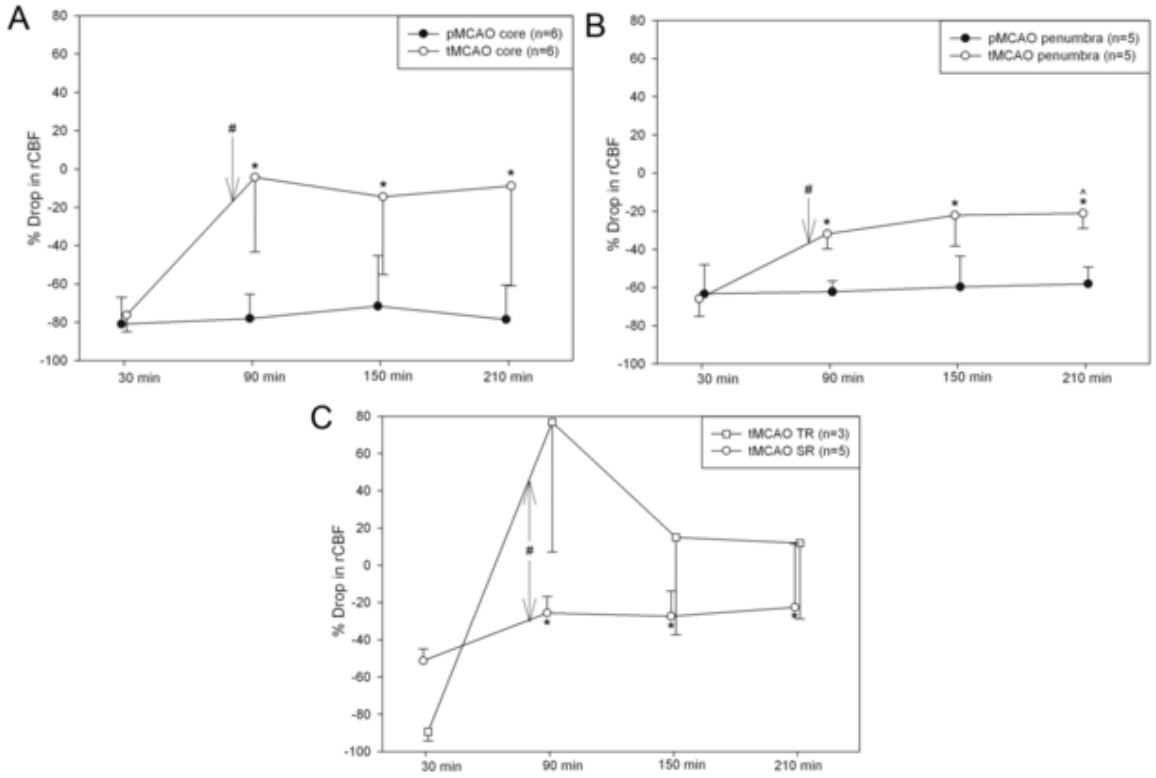

Figure 2.3 Time course of rCBF differences between the ipsi- and contralateral side in the A) core, B) penumbra, C) transient recovery and sustained recovery subregions as measured by P1152. *Significant increase in rCBF compared to 30min tMCAO ^ significant increase in rCBF compared to 90min tMCAO. # indicates the 80 minute reperfusion time point. P<0.05.

significant increases in rCBF were found at all time points following reperfusion as compared to the pre-reperfusion time point for both core and penumbra regions. The post-reperfusion time points also had significantly increased rCBF compared to the same time points in the pMCAO model. A significant increase in rCBF was also found between pre- and post-reperfusion time points in the SR region. Statistical differences in rCBF during ischemia were also found between the four subregions. Core and TR region were found to have significantly lower rCBF as compared to penumbra and SR region at the initial time point (see table 2.1). Based on DSC derived penumbral blood flow using P1152 during ischemia, an rCBF threshold of -62±11% was derived.

	Stroke Regions			
Stroke Region	Core	Penumbra	Sustained Reversal	Transient Reversal
Core	NA	0.005*	0.007*	0.984
Penumbra	0.005*	NA	1	0.023*
Sustained Reversal	0.007*	1	NA	0.006*
Transient Reversal	0.984	0.023*	0.006*	NA

Table 2.1 Significance levels of rCBF in ischemic subregions as determined by DSC during occlusion of animals subjected to MCAO. *$p < 0.05$.

2.6.2 Spatiotemporal evolution of the perfusion modalities

Figure 2.4A shows perfusion lesion volume evolution over time for CASL and P1152 derived DSC measurements in the pMCAO and tMCAO models. At each time point, no statistically significant volumetric difference was found between the perfusion lesion volume measured by CASL and contrast perfusion based rCBF as measured by P1152. As expected, in the pMCAO model, the volume of the perfusion deficit remained constant as shown by both the CASL and DSC techniques. As expected, the perfusion lesion volume in the tMCAO model revealed a large initial deficit with a rapid decrease following the 80 minute reperfusion. This decrease in hypoperfused volume was statistically significant compared to the pMCAO time point for both CASL and P1152.

To evaluate the generalizability of the P1152 DSC derived perfusion data, perfusion measurements were performed in a group of animals with Magnevist® and CASL. Similar to the results obtained with P1152, no statistical significant differences were found between the perfusion lesion volumes as measured by CASL and Magnevist®

DSC in animals subjected to pMCAO. However, the lesion volumes were significantly overestimated by Magnevist® DSC in tMCAO animals as compared to CASL following reperfusion. The perfusion deficit derived from Magnevist® DSC showed a similar temporal perfusion lesion volume evolution as that with P1152 (see Figure 2.4B).

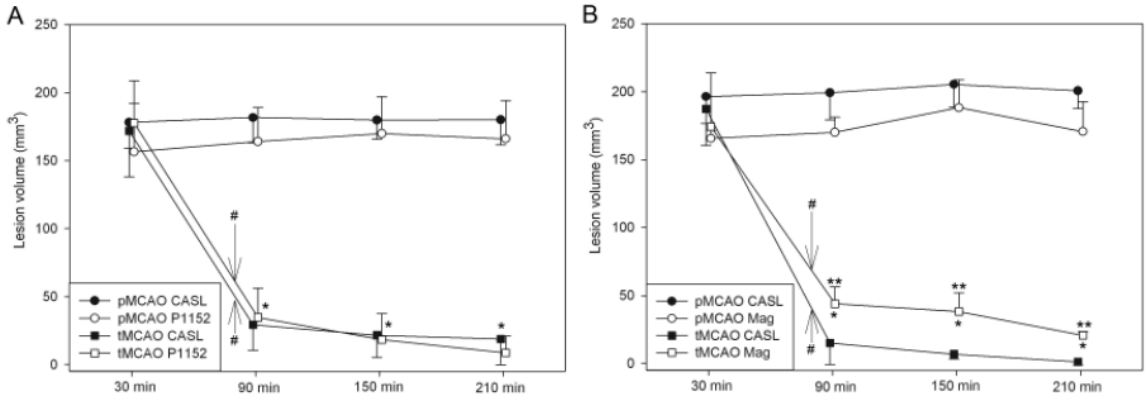

Figure 2.4 Volumetric analysis of the perfusion deficits in the pMCAO and tMCAO model. A) P1152 vs CASL and B) Magnevist® vs CASL. Note the persistent perfusion lesion volume over time in the pMCAO groups and the large drop in the perfusion lesion volume following reperfusion in the tMCAO groups. *Significant reduction in lesion volume compared to pMCAO time point for both CASL and DSC perfusion. **Significant increase in lesion volume compared to CASL perfusion. .#indicate the 80 minute reperfusion time point. $P<0.05$.

2.7 Discussion

Our results presented here demonstrate that DSC based relative perfusion measurements can potentially be used to monitor different regions of ischemic tissue in a preclinical model of stroke. Our results characterizing the time course of rCBF in ischemic subregions in both transient and permanent MCAO models of stroke are consistent with previously published results on spatial-temporal changes in blood flow as measured by CASL (36,89,100).

Results from animals subjected to tMCAO showed a statistically significant increase in rCBF in areas of core and penumbra compared to pre-reperfusion values. Areas of SR and TR also show an increase in blood flow from pre-reperfusion time points. The increase in rCBF as measured by P1152 in areas of SR following reperfusion reached significance, however, areas of TR did not. Lack of statistical significance may be due to the relatively small number of animals available displaying areas of TR and to the high inter-animal variability of the data.

Our results are consistent with previous work. In animals subjected to 35 minutes of MCAO followed by reperfusion, Bardutzky and colleagues reported that voxels which were characterized as being in the ischemic core during occlusion experienced an increase in rCBF following reperfusion (89). Despite different ultimate tissue fate, blood flow restoration was similar for each identified subregion (core, penumbra, SR, TR). This is similar to our results with the exception of the TR region where blood flow is more heterogeneous and tends to have a large initial overshoot in rCBF recovery followed by a

decline. In penumbral regions, we showed a moderate increase following reperfusion that leveled off at later time points. This is also similar to the results reported by Bardutzky and colleagues.

Interestingly, the initial values of rCBF for areas of SR were higher than those for TR. We also observed that penumbral regions had a significantly higher rCBF than both core and areas of TR. While a number of factors play a role in the recovery of tissue post-ischemia, the amount of remaining perfusion certainly plays a major role in tissue preservation (89). Our data suggest that careful analysis of the blood flow in the ischemic region as defined by ADC suppression may provide clues as to the extent of infarction recovery upon recanalization.

Based on our ROI analysis, we were able to derive a threshold value of -62±11% for the determination of ischemic tissue based on DSC derived rCBF. This threshold is slightly lower than the established threshold of a 57 ± 11% reduction of CBF for ischemic tissue as derived by CASL (41). This difference may be explained by the fact that quantitative CBF measurements in ASL techniques are highly dependent on the transit time of the labeled spins. Longer transit time, as is the case in ischemic stroke, causes longitudinal relaxation of the spins and may lead to underestimation of the blood flow in regions of low flow. In the case of longer transit times, the difference in signal intensity of the labeled images versus the control images would be smaller, resulting in an underestimation of the blood flow. Further, gradient echo based DSC measurements have been shown to overestimate the blood flow in areas of volume averaged large

vessels and tissue. (101). Given the spatial resolution, it is likely that some cerebral parenchyma voxels are partial volume averaged with large vessels. This would serve to increase the magnitude of the rCBF reduction between ischemic and normal tissue. Nevertheless, the threshold derived here for rCBF measurements can be used for quantitative analysis of the volumetric perfusion deficit in experimental stroke models. The derived threshold should be considered in light of the experimental technique used to acquire the data set. Contrast administration methodology and MR imaging parameters such as recovery and echo times can affect the derived threshold. Laboratories attempting to undertake contrast based MR perfusion measurements as the main modality for determining perfusion deficit in preclinical stroke models are encouraged to derive thresholds relevant to their contrast administration and imaging techniques.

Our DSC based volumetric analysis of the perfusion lesion in pMCAO and tMCAO models of stroke correlates well with the previously established CASL volumetric analysis. Moreover, there was no statistically significant difference between the volumetric analysis derived by DSC using P1152 and CASL. The volumetric measurements as derived by DSC matched well with the time course defined previously (40,42,89). While results demonstrated a similar temporal evolution of lesion volume between Magnevist® and P1152 derived measurements, Magnevist® derived data overestimated the perfusion deficit as compared to CASL in animals subjected to tMCAO. This is not entirely unexpected as areas on the border of tissue that remained ischemic and tissue that is fully reperfused may not be well characterized by Magnevist® as compared to P1152 due to its lower relaxivity.

These results lend credence to the use of DSC with P1152 to evaluate penumbral lesion volume in preclinical models of ischemic stroke. Although CASL offers many advantages over DSC based perfusion measurements, it suffers from more complex implementation from a hardware perspective. Transit time in rats from the spin labeling location (i.e. carotid arteries) to the brain parenchyma is rapid on the time scale of the longitudinal recovery rate of the blood magnetization. This is not the case in ischemic stroke where the transit time is increased (93). We have shown that contrast perfusion can be used to accurately measure the perfusion deficit in stroke. Due to its ease of implementation and the wide availability of contrast materials, it represents a viable alternative to CASL imaging in stroke in rats and perhaps clinically for perfusion deficit volume measurements. One of the main weaknesses of contrast enhanced methods from an imaging point of view is contrast retention in the blood causing 1.) a second pass phenomenon and 2.) a lack of rapid repeatability of perfusion measurements (102). The impact of the first issue has been addressed by fitting the data to a gamma variate function. Fitting this data set can be performed using non-linear least square fitting to a gamma variate model. Alternatively, a simplified form of the gamma variate, which was utilized in this study, allows for linear fitting of the data. One difficulty that has been pointed out for both approaches is the identification of the bolus arrival time, which can be particularly problematic in regions of low blood flow where the bolus arrival time may be indistinguishable from the baseline data. Automated detection schemes have been proposed to find the arrival time but all require clear delineations between the trend of the baseline and the bolus (103).

It is interesting to note that we were able to conduct these experiments using the same molarity per kilogram body weight of P1152 and Magnevist® as typically administered in clinical procedures for standard contrast agents. In other similar animal studies, double and triple doses of Magnevist® and other compounds are administered to be able to adequately characterize the rCBF (93,104).

A limiting factor for the ROI analysis is the small number of tMCAO animals that had TR regions that could be analyzed. The analysis of the TR and SR regions were not the primary goal of this study and should therefore be considered exploratory.

In conclusion, in this investigation, we have shown that MRI paramagnetic contrast agent based perfusion measurements reveal different blood flow changes within ischemic subregions. Further, we showed that ischemic lesion volume determination based on contrast perfusion measurements was not different as compared with CASL derived ischemic region volumes. High relaxivity contrast agents like P1152 may be more appropriate for measuring blood flow in certain ischemic subregions.

Chapter III: Visualization of the Temporal Dynamics of Clot Lysis *in vivo*

Ronn P. Walvick[1], Bernt T. Bratane[1], Nils Henninger, Kenneth M. Sicard, James Bouley, Zhanyang Yu, Eng Lo, Xiaoying Wang, Marc Fisher

From the department of Neurology (BTB, NH, KMS, JB) and Radiology (RPW), University of Massachusetts Medical School, Worcester, MA 01655 and the Neuroprotection Research Laboratory (ZY, EL, XW) Massachusetts General Hospital and Program in Neuroscience, Harvard Medical School, Charlestown, MA 02129.

1. Authors Contributed Equally

Aspects of this work presented at the 18th Annual International Society for Magnetic Resonance in Medicine Scientific Meeting and were accepted for presentation at the 7th Annual World Stroke Conference. Submitted to the journal Stroke.

3.1 Preface

MR visualization of clots can contribute to the overall utility of preclinical stroke research. There has been a recent push to derive new lytic compounds and compounds that augment tissue Plasminogen Activator (tPA). We have developed a method of labeling clots for MRI and histological visualization of *in vitro* clots injected in rats to cause an ischemic stroke. We have used this technique to test the effectiveness of recombinant Annexin II (rA2), a compound thought to increase the effectiveness of tPA. My contributions to this work include *in vitro* experimentation, experimental design, collecting and analyzing MR data, and co-principle authorship of the manuscript.

3.2 Acknowledgements

This study was supported by institutional grants. tPA was a kind gift from Genentech.

3.3 Abstract

Objectives: The purpose of this study was to develop a novel MRI method for imaging clot lysis in a rat embolic stroke model, and to compare tissue plasminogen activator (tPA) based clot lysis with and without recombinant Annexin-2 (rA2).

Methods: Experiment 1: *In vitro* optimization of clot visualization using multiple MRI contrasts agents in concentrations ranging from 5 to 50µL in 250µL blood. Experiment 2: *In vivo* characterization of the time course of clot lysis using the clot developed in the previous experiment. Diffusion, perfusion, angiography, and T1-weighted MRI for clot imaging were conducted prior to and during treatment with vehicle (n = 6), tPA (n = 8) or rA2+tPA (n = 8) at multiple time-points. Brains were removed for *ex vivo* clot localization.

Results: Clots created with 25µL Magnevist© were the most stable and provided the highest contrast-to-noise ratio. In the vehicle group, clot length as assessed by T1-weighted imaging correlated with histology (r = 0.93). Clot length and CBF-derived ischemic lesion volume were significantly smaller than vehicle at 15 minutes post-treatment initiation in the rA2+tPA group, while in the tPA group no significant reduction from vehicle was observed until 30 minutes post-treatment initiation. The rA2+tPA group had a significantly shorter clot length than the tPA group at 60 and 90 minutes post-treatment initiation, and significantly smaller CBF deficit than the tPA group at 90 minutes post-treatment initiation.

Interpretation: We introduce a novel MRI based clot imaging method for *in vivo* monitoring of clot lysis. Lytic efficacy of tPA was enhanced by rA2.

3.4 Introduction

Previous studies in experimental stroke models demonstrated that tissue plasminogen activator (tPA) mediated recanalization and subsequent reperfusion leads to reduced final infarct volumes (37,105,106). Currently available magnetic resonance imaging (MRI) methods to determine arterial patency such as time of flight angiography (TOF) in small animals are sensitive to a number of parameters including flow, blood longitudinal relaxation time, and sequence parameters (107). Signal intensity is based on a combination of these parameters and may make quantitative analysis of thrombolysis difficult. This might explain why a relationship between recanalization and reperfusion has not been clearly established (45). Direct clot imaging has been proposed, but these techniques typically require a multimodality approach or targeted contrast agents not readily available to investigators (108-110). Though *in vitro* assays are available to test the effects of thrombolytics on blood clots, these systems cannot sufficiently mimic the *in vivo* environment (111). Direct *in vivo* MRI-based visualization of the embolus will allow for near real time quantification of clot dissolution and provide unique information regarding lytic efficacy of thrombolytic agents.

In this study, we present a novel MRI methodology for clot visualization in an experimental stroke model using a commercially available contrast agent. Further goals of this study were to characterize clot lysis dynamics during thrombolytic therapy and to evaluate the lytic efficacy of tPA with or without recombinant Annexin-2 (rA2), a compound thought to enhance the lytic action of tPA (105). We hypothesize that 1.) clot visualization with MRI is possible via the addition of contrast agent to the blood prior to

formation, 2.) the clot length as measured by MRI is representative to that measured *ex vivo*, 3.) MRI based clot visualization is useful in visualization of clot lysis, and 4.) MRI based clot visualization is sensitive to the efficacy of different lytic agents.

3.5 Materials and Methods

This study consisted of two experiments. The first (*in vitro*) experiment involved designing a robust method for modifying standard clots for visualization on MRI and histology. The second (*in vivo*) experiment characterized the temporal evolution of clot lysis mediated by tPA vs. tPA combined with rA2 (rA2+tPA) utilizing MRI.

3.5.1 In vitro experiment (Experiment 1)

Briefly, clots were formed by as follows: 200uL of blood was withdrawn from the tail artery and mixed with 4.5uL of 1 mol/L calcium chloride and 1.0 National Institutes of Health (NIH) units of human thrombin. A portion of the mixture was drawn into a 30cm polyethylene catheter (PE-50) and was allowed to clot for 2 hours at 37°C for 2 hours. Following this period, the clot was ejected from the tubing into a 2% Evans Blue (EB) solution and stored at 4°C for 24 hours (112). These clots were modified by mixing 250 µL of blood with four different contrast agents at volumes of 0uL, 5uL, 10uL, 15uL, 20uL, 25uL, and 50uL to blood prior to clotting to determine optimal contrast agent type and volume for MRI visualization. The contrast agents used were Magnevist© (Berlex Laboratories, Montville, NJ, USA), Combidex© (Combidex Threading Tools b.v, Nieuwe Waterwegstraat 5, Schiedam, Holland), Omniscan© (GE Health Care, Princeton, NJ, USA) and Eovist© (Bayer Healthcare Pharmaceuticals, Wayne, NJ, USA). An animal surgeon with experience in embolic stroke modeling inspected the quality of the clots. At the contrast volumes used, Magnevist© infused clots showed consistent stability, while the use of the other contrast agents resulted in fragile and unstable clots. Magnevist© was therefore used for the *in vitro* and *in vivo* experiments.

For *in vitro* quantification of contrast intensity Magnevist© clots were placed in saline and imaged using the T1-weighted imaging (T1WI) sequence described in the MRI section. The resulting signal intensity of the clot and surrounding saline was measured. The clot enhancement ratio was calculated by dividing the clot signal intensity by the saline signal intensity.

3.5.2 In vivo experiment (Experiment 2)

All procedures used in this study were approved by University of Massachusetts Medical School Institutional Animal Care use Committee. Spontaneously breathing male Wistar rats (n = 22, Taconic Farms, Hudson, NY, USA) weighing 318 ± 27 g were anesthetized with isoflurane (5% for induction, 2% for surgery, 1.2% for maintenance) in room air. PE-50 polyethylene tubing was inserted into the femoral artery for monitoring of mean arterial blood pressure (MABP), blood gases, electrolytes, and glucose. Additional tubing was inserted into the femoral vein to allow for intravenous (i.v.) infusion of tPA, rA2+tPA, or vehicle. Body temperature was monitored continuously with a rectal probe and maintained at 37.0 ± 0.5°C with a thermostatically controlled heating pad. Embolic stroke (ES) was induced in all 22 animals. Briefly, the ES was induced by temporarily occluding the common carotid artery and catheterizing the external carotid artery. The external carotid artery catheter was advanced to the base of the skull via the internal carotid artery and a 18mm clot was injected (112). The animals were randomly assigned to either vehicle (n = 6), tPA (n = 8) or rA2+tPA (n = 8) treatment. The i.v. infusion of thrombolytics or vehicle was administered at 90 minutes following ES with a 10% bolus and the remainder infused over 1 hour. The vehicle group

received 1 mL of saline, while the tPA groups received 10 mg/kg tPA dissolved in either 1 mL of saline or rA2 solution (5 mg/kg). Histidine tagged rA2 was produced in *E. coli* from a bacterial expression vector containing full-length human annexin-2 complementary DNA according to the method previously described (113). Purity of rA2 was confirmed by sodium dodecyl sulfate polyacrylamide gel electrophoresis (SDS-PAGE) followed by Coomassie blue staining, and its identity was verified by western blot analysis. rA2 was finally eluted and kept in elution buffer (20 mM sodium phosphate, 0.5 M NaCl, 500 mM imidazole, pH 7.4). Imaging was performed from 30 to 180 minutes and animals were electively sacrificed at 3.5 hours after ES to remove their brains. Brains were imaged using an optical scanner and EB stained clots were identified and their lengths measured.

3.5.3 MRI

MRI experiments were performed on a Bruker system utilizing a 4.7 T/40 cm horizontal magnet equipped with Paravision software (Billerica, MA), and a 20G/cm gradient insert (ID = 120 mm, 120 μs rise time). A surface coil (ID = 23 mm) was used for brain imaging and an actively decoupled neck coil for perfusion labeling (40). T1WI and perfusion weighted images (PWI) were acquired at 60, 90, 105, 120, 135, 150 and 180 minutes post-ES. Diffusion weighted imaging (DWI) was acquired at 30, 90, and 160 minutes post-ES. TOF magnetic resonance angiography (MRA) was performed at 60 and 150 minutes post-ES. PWI, DWI and MRA were performed as previously described in detail.(112) Two contiguous slices with in plane visualization of the bifurcation of the middle cerebral artery (MCA), anterior cerebral artery (ACA), and internal carotid artery

(ICA) were recorded sequentially using a T1WI centric ordered turbo spin echo with a echo train length of 4, an echo time of 3.2 ms, a recovery time of 290 ms, a field of view (FOV) of 2.56 x 2.56 cm, a slice thickness of 750 µm, and a matrix size of 256 x 128. Saturation slabs 1 cm thick were placed posterior and anterior to the Circle of Willis to reduce flow induced imaging artifacts.

3.5.4 Analysis of MRI data

A maximum intensity projection image (MIP) was created from the two T1WI slices acquired, and analyzed using the Medical Image Processing, Analysis, and a Visualization software package (NIH, mipav.cit.nih.gov). To identify the clot on the MIP of the T1WI, a ≥ 30% signal intensity within the ICA, MCA, and ACA compared to the surrounding brain parenchyma was chosen. An investigator (RPW) blinded to treatment assignment outlined the clots using the software's tracing tool. The length of the clot in each vessel was summed and the total clot length during and after treatment was reported as a percentage of the initial clot length.

DWI, PWI and MRA were analyzed blinded to treatment assignment using QuickVol II (http://www.quickvol.com/) (114). Quantitative apparent diffusion coefficient (ADC) and cerebral blood flow (CBF) maps were created and their corresponding threshold-derived lesion volumes were calculated as described previously (40,114). The thresholds used to define respective abnormal ADC and CBF regions were a reduction to 0.53×10^{-3} mm^2/s and 0.3 mL/g/min, respectively, as previously validated.(40) Diffusion and perfusion lesion volumes are expressed as percentages of the initial volumes at 30 (DWI) and 60 (PWI) minutes, respectively.

For comparative purposes, MRAs were visually analyzed by a blinded investigator (KMS) and were scored on a 3 point scale as follows: 3 = complete MCA occlusion, 2 = partial MCA reperfusion and 1 = complete reperfusion of the MCA. MCA was selected for analysis to reveal an overall picture of vessel recanalization.

3.5.5 Analysis of Evans Blue Clot Histology

The entire surface of all the rat brains was scanned with a high resolution (1600 dpi) scanner. The EB clot was identified, and measured by summing the length of all clot fragments. Total clot length was assessed and correlated with MRI to validate T1WI-derived clot length and to determine the lytic efficacy of each treatment.

3.5.6 Statistics

Data are presented as mean ± standard deviation. Statistical comparisons were performed using one-way Analysis of Variance (ANOVA) with *post hoc* Least Significant Difference (LSD) test for multiple comparisons. Correlation analysis was performed using Pearson two-tailed test (Version 15.0, SPSS Inc., Chicago, IL, USA). $p<0.05$ was considered significant.

3.6 Results

3.6.1 In vitro clot experiments

Figure 3.1 shows a Magnevist© enhanced clot suspended in saline. The clot's signal enhancement ratio was calculated for concentrations ranging from 0 µL to 50 µL of Magnevist©. Signal enhancement was undetectable in clots with the lowest contrast agent

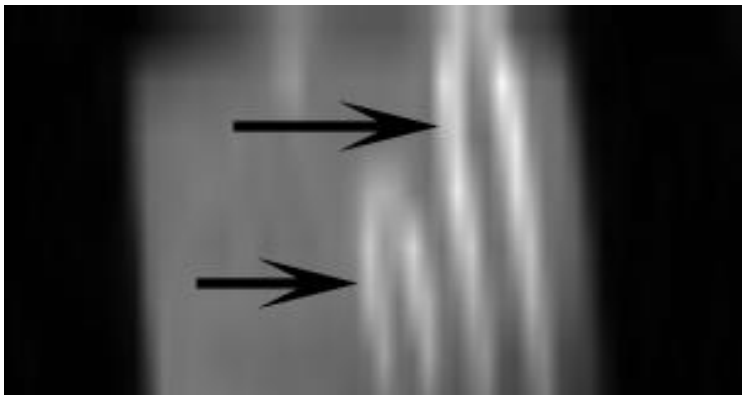

Figure 3.1 Maximum intensity projection of Magnevist© (25 µL contrast agent in 250 µL blood) infused clots suspended in saline utilizing T1-weighted imaging. Arrows point to clot sections.

volumes of ≤ 5 µL. Table 3.1 displays the clot's signal enhancement ratios at various Magnevist© volumes. The 25 and 30 µL Magnevist© volume provided significantly higher signal enhancement ratios relative to all other concentrations used, with insignificant differences between these two concentrations.

	Contrast Concentration							
	0 µL	5 µL	10 µL	15 µL	20 µL	25 µL	30 µL	50 µL
Enhancement Ratio	0	0	1.28±0.04	1.26±0.06	1.32±0.09	2.1±0.10#	1.88±0.15#	1.45±0.22

Table 3.1 *In vitro* clot enhancement ratios

We opted to use 25 µL Magnevist© in all further experiments to obtain the highest clot signal enhancement ratio while utilizing the lowest contrast agent volume.

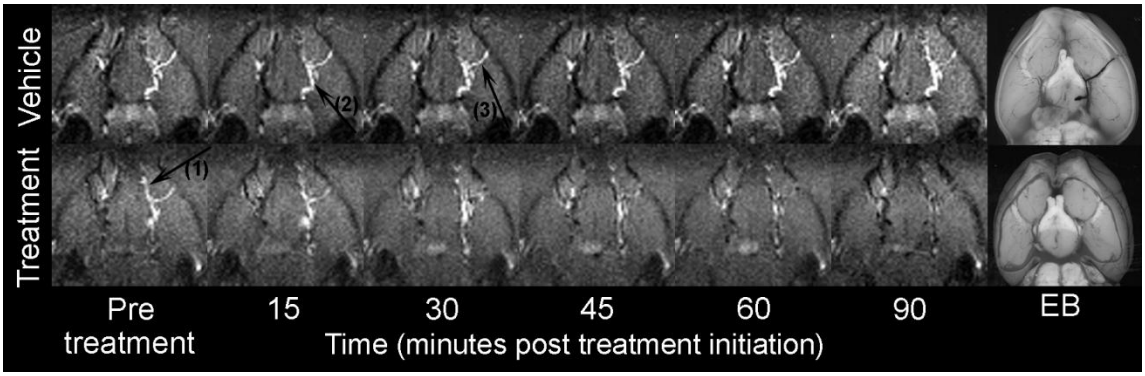

Figure 3.2 *In vivo* Maximum Intensity Projection of the clot utilizing T1-weighted imaging in a representative vehicle (top) and tPA (bottom) treated animal, respectively. Note the progressive clot lysis in the tPA-treated but not the vehicle animal. T1-weighted imaging results match well with Evans Blue (EB) stained clot found on histology 3.5 hours post embolization. Arrow 1, 2 and 3 points to clot visible in anterior cerebral artery, internal carotid artery, and middle cerebral artery respectively.

3.6.2 In vivo clot experiments

The Magnevist©/EB-modified clots were visible on MRI and histology. They produced consistent arterial occlusion and subsequent ischemic changes as assessed by T1WI, PWI, DWI and MRA in all animals. When exposed to tPA the clot slowly dissolved over 90 minutes after treatment initiation. In both the vehicle and the tPA group, T1WI results matched well with EB stained clot found in the MCA, ACA and ICA *post mortem* (Figure 3.2). T1WI-derived 180-minute clot length correlated significantly with the clot length assessed on histology ($r = 0.93$, $p < 0.05$). Figure 3.3 shows a scatter plot of histologically and MRI derived clot lengths.

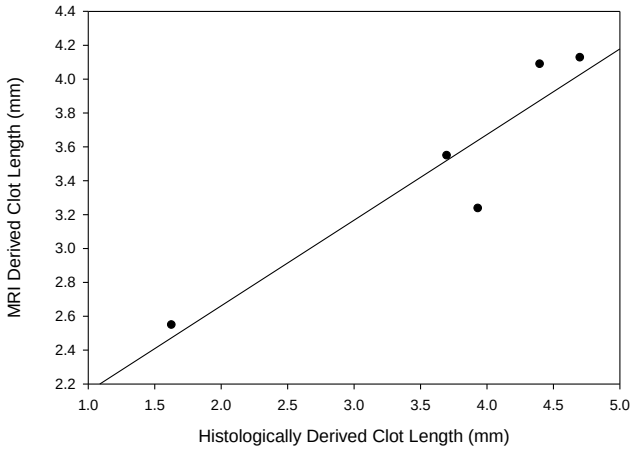

Figure 3.3 Histologically versus MRI Derived Clot Length measures. r=.93, p<.05 Note: Regression Line Shown

3.6.3 MRI experiment

Initial clot localization was determined in all animals before treatment was initiated. Clot localization was as follows: MCA + ICA + ACA (n = 13 (59%)), ICA + ACA (n = 4 (18%)), ACA + MCA (n = 3 (14%)), and ICA + MCA (n = 2 (9%)), respectively. MABP, blood gases, electrolytes, and glucose were not significantly different between groups, and values remained within physiological limits throughout the study (Appendix II).

Clot length and CBF lesion volumes were significantly smaller than vehicle at 15 minutes post-treatment initiation in the rA2+tPA group, while in the tPA group no significant reduction from vehicle was observed until 30 minutes post-treatment initiation. Beginning at 60 minutes post-treatment clot length in the rA2+tPA group was significantly smaller than in the tPA group. From 90 minutes post-treatment initiation, CBF lesion volume in the rA2+tPA group was significantly smaller than in the tPA group (see Figure 3.4).

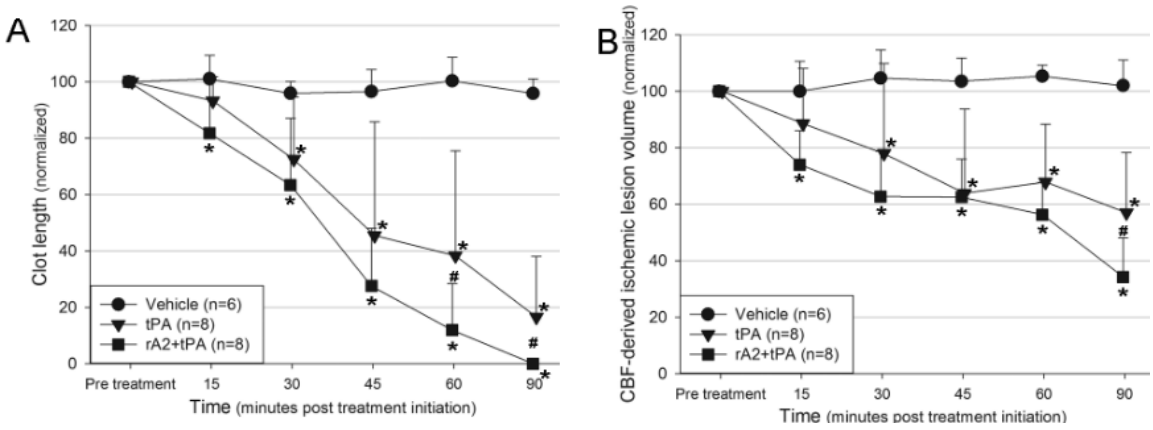

Figure 3.4 Temporal evolution of A) T1-weighted imaging derived clot length and B) perfusion lesion volume in the experimental groups. *Significant difference between treatment group and control. #Significant difference between treatment groups. $p < 0.05$. Note, $n = 5$ for the last imaging time-point in Figure B for the rA2+tPA group.

Plotting CBF lesion volume versus clot length gives the clot lysis profile for each animal over time. In the vehicle group no clot lysis was observed as indicated by consistent CBF lesion volumes and clot lengths over time (Figure 3.5A-E). Following thrombolysis all animals demonstrated a reduction in CBF lesion volumes and clot lengths with rA2+tPA animals displaying the most complete clot lysis and reperfusion.

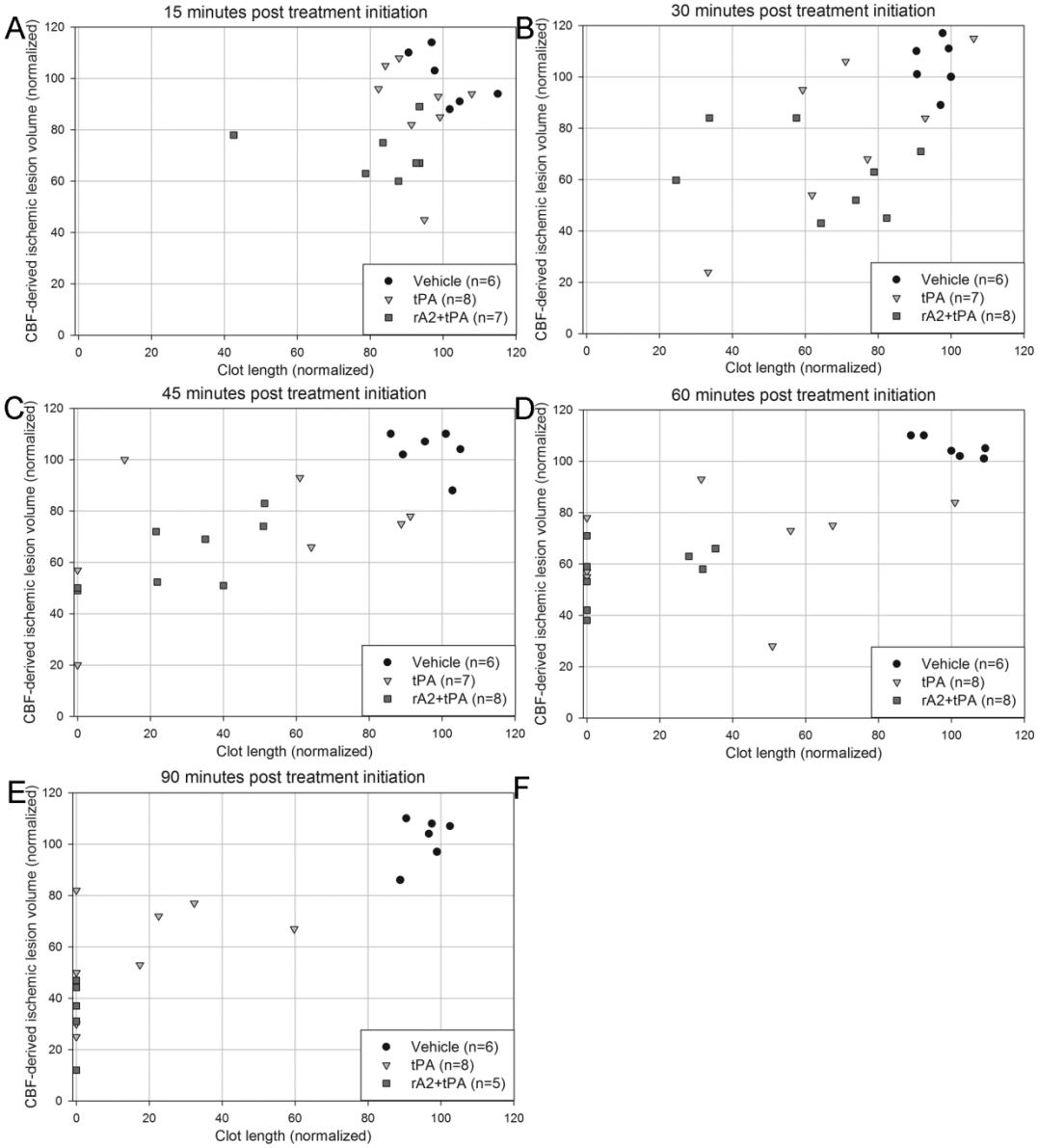

Figure 3.5(A-E) Scatter plot graphically displaying the time course of clot lysis and perfusion restoration in vehicle, tPA and rA2+tPA treated. Both treatment groups show migration toward restoration of perfusion deficit and clot lysis. All animals in the rA2+tPA group had complete clot lysis while only half of the tPA animals had complete clot lysis.

There was a non-significant reduction in the ADC lesion volumes between the two treatment groups and the vehicle groups at 150 minutes post ES (Figure 3.6).

MRAs revealed a significant effect of treatment on vessel patency ($p<.05$) but no difference between the three treatments. The results are displayed in Table 3.2.

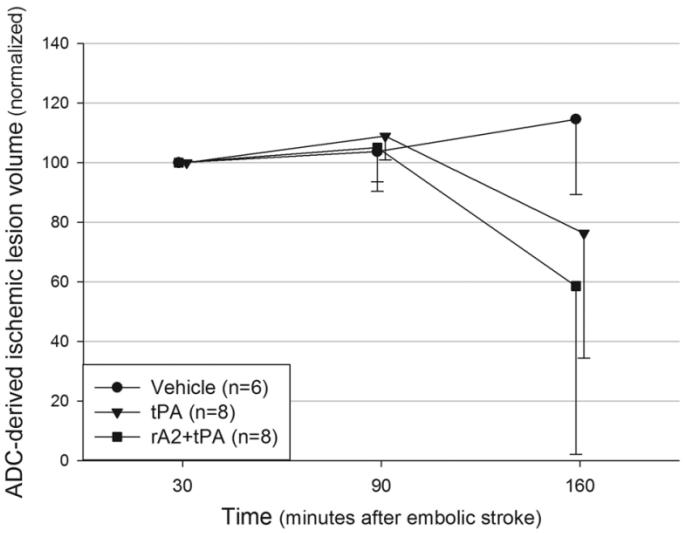

Figure 3.6 Temporal evolution of the ADC-derived ischemic lesion volumes. Values presented as % of the 30 minutes lesion.

	Treatment		
	Saline	tPA	tPA+rA2
Pre treatment	2.80±.5	3±0	3±0
Post treatment	2.60±.5	1.5±.93	1.63±.74

Table 3.2 MRA vessel patency data from the treatment groups prior to and following treatment. 3=complete occlusion, 2=partial occlusion, 1=no occlusion.

3.7 Discussion

This study describes a novel approach for MR visualization of clot and clot lysis in a rat embolic stroke model by adding Magnevist©, a widely available MR contrast agent, to the blood prior to clotting.

The utility of this approach is to compare directly the efficacy of thrombolytic agents on speed and completeness of clot lysis. Prior studies indirectly assessed thrombolytic efficacy by comparing DWI/PWI derived lesion volumes, MRA or final infarct volume on histology (37,107,115). However, directly visualizing clot integrity is especially important at late therapeutic time points in which the 'no or low reflow phenomenon' may occur (116). Complete recanalization can potentially occur with a small or non-existent response of the CBF or DWI lesion volume. Information about clot lysis enhances the overall understanding of the results of treatment and more completely answers questions about the mechanisms of success or failure of an investigational stroke treatment. Further, this methodology allows for more complete characterization of the emoblic stroke model. Our results show that a wide variety of clot configurations occur in the cerebral vasculature which may explain some of the variability seen in this model (36).

Clot length was used to determine clot lysis *in vivo*. This metric directly defines the temporal efficacy of different thrombolytic agents independent of surrogate markers such as perfusion deficit or TOF-derived blood flow. Together with perfusion and

diffusion imaging, imaging of clot lysis allows for a more thorough characterization of the efficacy of thrombolytics in an ES model.

To show the utility of this method, we compared the effects of vehicle, tPA alone, and rA2+tPA treatment. rA2+tPA more reliably produced thrombolysis relative to tPA alone. Our results show that half of all tPA animals had some clot remaining in the arteries while no animals in the rA2+tPA group had clot remaining. At the final imaging time point following treatment, rA2+tPA resulted in statistical smaller perfusion lesion volume in the rA2+tPA group then the tPA group. Further, rA2+tPA resulted in an earlier statistically significant difference in CBF deficit volume versus vehicle compared to tPA alone.

rA2 is thought to operate as a cell-surface receptor for both plasminogen (the inactive precursor of plasmin), and its activator, tPA (117,118). The rA2-tPA-plasminogen triple complex is more effective than tPA alone in converting plasminogen into plasmin (119,120). Our previous study confirmed the enhanced plasmin generation by rA2+tPA *in vitro* and demonstrated rA2+tPA improved neurological outcomes in a rat focal embolic stroke model (105). It is possible that rA2+tPA generates more plasmin at the clot site because it has been demonstrated that the plasmin precursor, plasminogen, binds to the endothelial cell surface and is enriched in the clot (120,121). Therefore, rA2+tPA may locally bind plasminogen and consequently amplify plasmin generation in the vicinity of the clot, resulting in more effective fibrinolysis.

Although we report faster and more complete clot lysis and reperfusion, there was no statistically significant difference in the final ADC lesion volume between groups. We hypothesize that this finding was due to the late initiation of treatment in this experiment. Previous findings in the rat suture model of stroke showed that after 95 minutes of ischemia, recovery of the ADC lesion was non-significant (89). Future experiments should investigate the relationship between lysis efficacy and ADC lesion resolution.

The clot imaging protocol was limited as it is only sensitive to clot localized in the bifurcation of the ICA, ACA, and MCA. Sections of the MCA distal to the M1-segment were not visible. At the current resolution, larger imaging field of views would require lengthier scans and therefore would impede the ability to do other scans and limit the temporal scanning during the acute stroke phase and at multiple time points during treatment.

To summarize, in this study we: (1) successfully developed a methodology that enables us to visualize clots using a contrast reagent Magnevist© in a focal rat embolic stroke model; (2) used this new method to characterize clot lysis dynamics during thrombolytic therapy; and (3) documented that tPA+rA2 yields faster and more consistent thrombolysis than tPA alone. This new methodology provides a novel approach to preclinically evaluate investigational thrombolytic agents.

Chapter IV: Evaluation of Oxygen Sensitivity of Hyperpolarized Helium Imaging in the Detection of Pulmonary Ischemia

Ronn P. Walvick, Austin L. Reno, Matthew J. Gounis, Mitchell S. Albert

From the Department of Radiology, University of Massachusetts Medical School,

Worcester, MA 01604

4.1 Preface

The longitudinal relaxation of hyperpolarized helium is highly dependent on the oxygen content in the gas. This sensitivity has been exploited to measure the initial partial pressure of oxygen in the pulmonary air spaces and the oxygen transfer from the airspaces to the lung which both indirectly measures pulmonary blood perfusion. In this work, we evaluate the sensitivity of this measurement to pulmonary ischemia in rats using both simulation and an experimental model of pulmonary embolism. The average initial partial pressure of oxygen and oxygen depletion rate were elucidated in a cohort of normal to determine proper parameters for simulation of ischemia. A rat model of pulmonary ischemia was utilized to examine the sensitivity of these measurements to disease. My contributions to this work include running simulations, animal handling, experimental design, collecting and analyzing MR data, and principle authorship of the manuscript.

4.2 Acknowledgements and Funding

We acknowledge the technical assistance of Joey Mansour and Jaime Kinnear. Further, we acknowledge Dr. Michael A. King for assistance with simulation, and Dr. John Roche for thoroughly reviewing and editing the manuscript.

4.3 Introduction

About six-hundred thousand new incidents of pulmonary embolism following deep vein thrombosis are reported per year in the U.S. (63). Given the high incidence of this condition, advances in diagnosing and assessing treatment for pulmonary embolism are crucial. Small mammal models of pulmonary ischemia have been found to be useful in evaluating the pathophysiological response to pulmonary embolism, and the effect of treatment on the restoration of normal lung function (65,122,123). Imaging of this process in small mammals is made difficult by physiological factors such as high heart and respiratory rate, and by technical limitations imposed by the necessity of high spatial and temporal resolution. Pulmonary MRI using hyperpolarized gas has emerged as a technique to circumvent many issues inherent to pulmonary imaging (12,79). By mapping the signal decay of hyperpolarized helium-3 (HP-He) during an extended breath hold, we can obtain information about the initial partial pressure of oxygen (p_o) and the oxygen depletion (16,124). Both parameters yield information about the efficiency of oxygen transfer from the airspaces to the blood, which is related to the local pulmonary blood perfusion.

Whereas this measure has been shown to be a sensitive and reproducible measure of pulmonary ischemia in large animal models of pulmonary embolism, no one has yet elucidated information about the sensitivity of this measure to disease in rodents (83,125). Cieślar et al. described the first measurements of the p_o and oxygen depletion rate in rats and mice, but did not measure these parameters in animals with simulated ischemia (16,84). Validating this method in small mammal models of simulated ischemia

will allow for its use in understanding pulmonary ischemia pathophysiology and treatment efficacy.

In this work, we characterize the effects of ischemia on the exchange of oxygen between the airspaces and the blood in an experimental model of rodent pulmonary embolism. As performed in previous studies, we used a single acquisition method to map both of the aforementioned parameters, as well as to account for local flip angle variations (16). We used the data to simulate varying levels of ischemia, and to ascertain the sensitivity of the HP-He-derived alveolar oxygen measurement method in small animals. We hypothesize that 1.) the measurement of the longitudinal relaxation time of hyperpolarized helium is sensitive to pulmonary embolism and 2.) moderate to high SNR images are necessary to detect changes in pulmonary ischemia by the measurement of the longitudinal relaxation time of hyperpolarized helium.

4.4 Methods

4.4.1 Animal Handling

Animal procedures were approved by the University of Massachusetts Institutional Animal Care and Use Committee. Twelve Sprauge Dawley rats were anesthetized with 5% isoflurane and maintained at 1.5–2.0% isoflurane in oxygen. Animals were separated into either a control group (n = 6) or an experimental group (n = 6). All animals received tracheotomies. No further interventions were conducted on control animals. Experimental animals were transported to an angiosurgical suite (Philips Allura FD20; Best, the Netherlands) that was adjacent to the MRI suite. Under fluoroscopic guidance, a microcatheter was advanced over the wire via a transjugular approach to the selected pulmonary branch. Correct positioning was confirmed with digitally subtracted angiography. After flushing the microcatheter with 5% dextrose solution, the branch was embolized with a 3:1 mixture of n-butyl-2-cyanoacrylate and Lipiodol, respectively (Codman Neurovascular, Raynham, MA). Once the pulmonary artery branch was embolized, we transferred the animals to a 3.0T Philips Acheiva Clinical MR scanner for imaging. Animals were connected to an anesthesia circuit that allowed for spontaneous respiration with the capability of administration of HP-He. Animals were continuously warmed with a hot air small animal heating system. We conducted physiological monitoring using an MR-compatible small animal monitoring device (SAI, Stonybrook, NY).

4.4.2 MRI Methods

MR imaging was conducted using a single-turn solenoid coil tunable to both the proton and helium frequencies. Proton localizer scans were conducted to ensure proper positioning of the animal. Twelve hours prior to imaging, helium was polarized to 10–20% on a custom-made helium polarizer. A volume of 6 ml of HP-He and 2 ml of oxygen were withdrawn and mixed in a syringe just prior to administration to the animal. The amount of oxygen was chosen based on the work by Ciéslar et al. in rats to optimize the tradeoff between SNR of the images and ascertain meaningful oxygen uptake rates (16). Once administered, a 24-second breath hold was imposed on the animal, during which we conducted helium imaging. The helium sequence was similar to that of Fisher et al., and consisted of two consecutive images acquired with no delay for radio-frequency power calibration, followed by an image every 2 seconds (125). Details of the imaging sequence were as follows: FOV = 50 mm, Recovery Time=4 ms, Echo Time=980 μs, Flip Angle = ~10°, MTX = 64x32, and slice thickness = ∞ (i.e., projection image). After acquisition, the images were zero-filled to achieve a final matrix size of 64x64.

4.4.3 Analysis of Initial Partial Pressure of Oxygen and Oxygen Depletion Rate

Analysis of initial pO_2 and oxygen depletion rate has been described in depth in other works (16,125,126). The decay rate of HP-He in the presence of oxygen (T_{1,O_2}) can be described as (16,127):

$$T_{1,O_2} = \xi(pO_2)^{-1} \quad [4.1]$$

where pO_2 is the partial pressure of oxygen, apnd ξ is a constant equal to 2.6 bar·sec. Assuming correction for RF depolarization, the time course of the signal decay can be described by (16):

$$S_m = S_0 e^{-\int_0^{m\tau} pO_2(t')dt'} \quad [4.2]$$

where S_m is the signal intensity at the m-th acquired image, S_o is the signal intensity of the first acquired image following the RF calibration in the sequence, and τ is the delay between image acquisitions. Assuming a linear uptake of pO_2 in the lungs (16):

$$pO_2(t) = p_o - Rt \quad [4.3]$$

where p_o is the initial partial pressure of oxygen and R is the rate of oxygen uptake into the blood. Substituting equation [3] into equation 2, equation 2 can be expressed as (16)

$$-\frac{\xi\left(\ln\left(\frac{S_m}{S_o}\right)\right)}{m\tau} = p_o - Rt \quad [4.4]$$

where $t = m\tau/2$. This equation can be solved by performing a linear fit using a least squares method.

The effect of RF depolarization was quantified by (17):

$$\varepsilon = S_{RF_1}/S_{RF_0} e^{\frac{p_o \Delta\tau_{RF}}{\xi}} \quad [4.5]$$

where S_{RF_0} and S_{RF_1} is the first and second RF calibration image, respectively acquired, and $\Delta\tau_{RF}$ is the time between the acquisition of the center of k-space of images S_{-1} and S_o. The flip angle can be calculated from ε by (125)

$$\alpha = \text{acos}\,(\varepsilon^{\frac{1}{N}}) \quad [4.6]$$

where N is the number of phase encodes and α is the flip angle.

Each image was divided by ε to eliminate the influence of RF depolarization on the measurement of p_o and R. Because the measurement of p_o affects the calculation of ε, which in turn affects p_o, we iteratively determined the values of R, and ε until convergence was reached.

4.4.4 Image Analysis

In control animals, two region of interests (ROIs) were placed in both the left and right lobe of the lung for quantitative measurement of p_o and R. In experimental animals, ROIs were selected in areas of ischemia as indicated by digital subtraction angiography, as well as in the contralateral side, and analyzed for p_o and R. Assuming a Gaussian noise distribution, we measured the SNR of these ROIs through the division of the signal intensity by the standard deviation of the noise.

4.4.5 Simulation

To characterize the accuracy and precision of the measurement at various SNRs, the noiseless time course of the decay of the HP-He signal is expressed as (125)

$$M_m = M_1 \cos\,(\alpha)^{mN} e^{-\frac{1}{\xi}\left[p_o m\tau - \frac{1}{2}R(m\tau)^2\right]} \quad [4.7]$$

where M_x is the simulated value of the time course of helium decay at acquired image x and M_1 is defined by (125)

$$M_1 = M_o \cos(\alpha)^N e^{\frac{p_o \Delta\tau_{RF}}{\xi}} \quad [4.8]$$

For purposes of simulation, M_o was set to 1. We used average values for p_o, R, and α of the contralateral lung in the experimental animals as starting points for simulation. To simulate the *in vivo* ROI analysis, we generated 25 noiseless curves. We varied the SNR of the curves between 12–200 through the addition of Gaussian noise by:

$$A_m = M_m + \frac{1}{SNR} n \quad [4.9]$$

where A_m is the simulated signal intensity at time *t* during the acquisition, M_m is the noise free data acquisition value derived from equations 4.7 and 4.8,' and *n* is a random number generated from a Gaussian distribution with μ=0 and σ=1. We averaged the noise modified curves together and conducted the identical *in vivo* analysis. Next, to simulate the embolism condition, we raised and lowered values of p_o and R, respectively, by 90% in increments of 15% of the original. We also determined the accuracy and precision of the measured parameters. The simulation was performed 1000 times and the average and standard deviation of the fitted values of p_o and R were determined at each SNR. We considered a particular value of p_o or R at each level of ischemia differentiable from another level of ischemia if the measured values were two standard deviations of the mean away from each other.

4.4.6 Statistics

All statistical analyses were conducted on SPSS Statistics software (SPSS, Chicago, IL). Comparisons of quantitative values of p_o, R, and flip angle in control and

experimental animals were conducted using a one-way ANOVA with a post-hoc Bonferroni multiple comparison test. Data are expressed as mean ± 1 STD.

Results

Figure 4.1 shows representative images of the results of the surgical procedure on the experimental rats. Figure 4.1a illustrates the placement of the embolic material in the pulmonary artery visualized by radiography. Figure 4.1b was obtained during the peak opacification, showing hypoperfusion in the embolized lung. The model produced focal ischemia in the anterior and middle portions of the left lung. Due to anatomical overlap of the inferior portion of the left and right lungs, it was not possible to determine the extent of ischemia in this area.

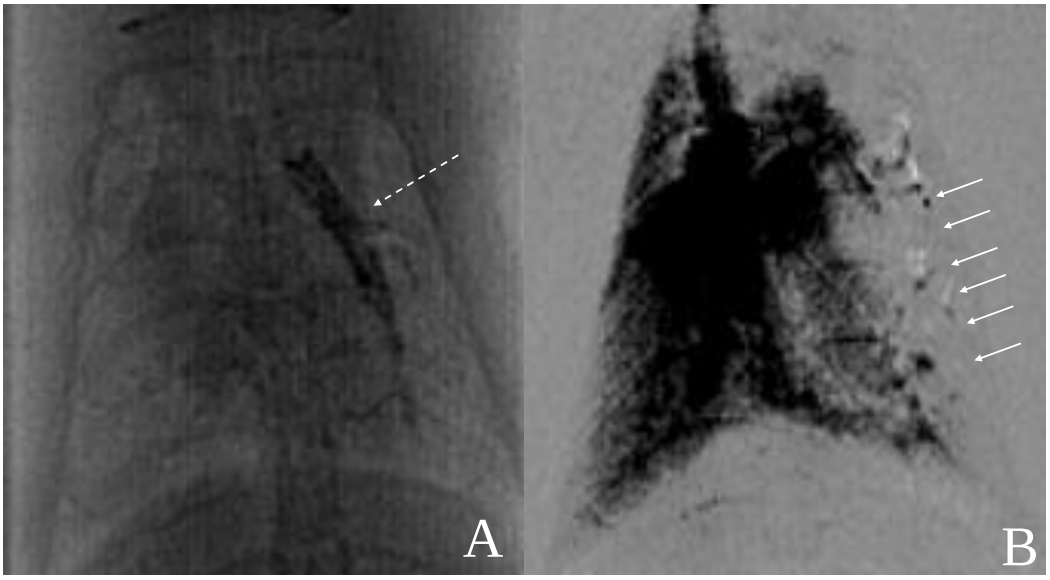

Figure 4.1 Radiographs visualizing the results of the pulmonary embolic surgery. A.) A radiograph of an experimental animal post pulmonary embolism placement. The dashed arrow points to the embolic material situated in a division of the left pulmonary artery. The material is radio-opaque of the artery. B.) Visualization of the opacification of the lung during iodinated contrast bolus transit. The solid arrows indicate areas of low perfusion as determined by minimal opacification.

Figure 4.2a-f displays two sets of HP-He images in animals with and without ischemia at 0 seconds, 10 seconds, and 24 seconds following helium administration, respectively. The partial pressure of oxygen, p_o, the oxygen depletion rate, R, and flip angle, α, were determined from an ROI analysis from the center of each lung. Figure 4.3

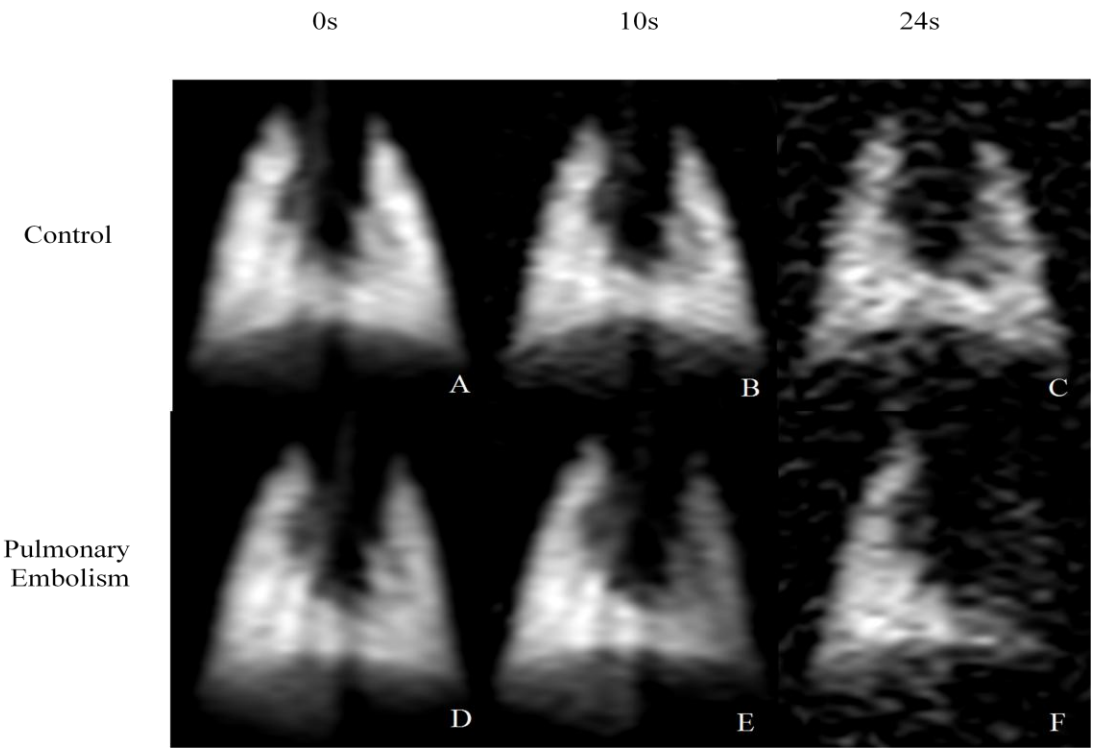

Figure 4.2 Representative images of the decay of the hyperpolarized helium signal in the lungs in normal (A-C) and embolized (D-F) animals 0 (A,D), 10 (B,E) and 24 (C,F) seconds after helium administration.

displays the time course of PO_2 in ROIs localized in the ischemic and contralateral lungs in the animals displayed in Figure 4.2.

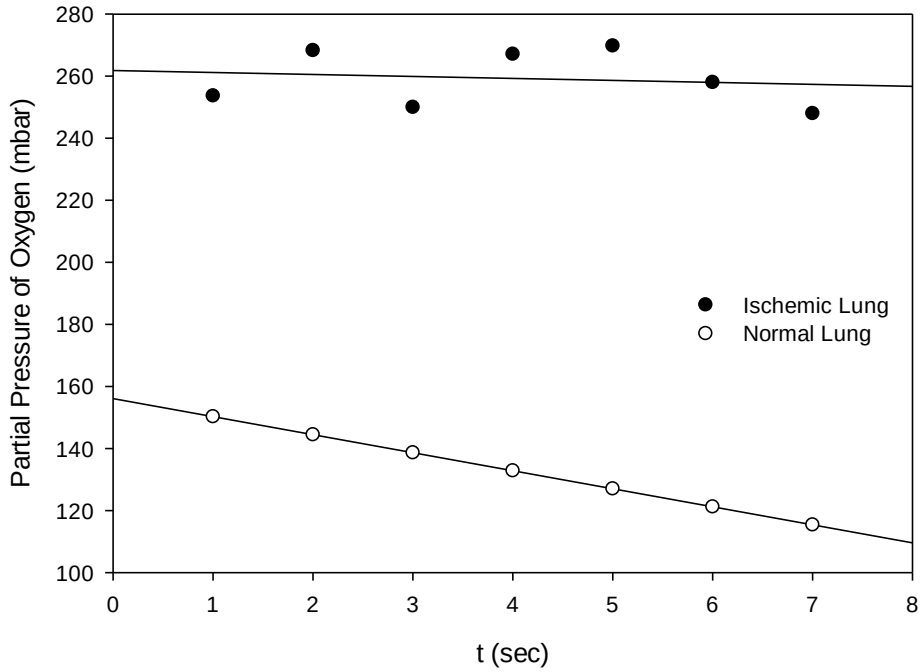

Figure 4.3 The time course of the partial pressure of oxygen in an ROI in the ischemic and normal lobe of the animal displayed in Figure 2D-F. Note: $t = m\tau/2$

Results in control animals reveal values for p_o, R, and α in the left lung of 162.13 ± 33.28 mbar, 6.40 ± 1.05 mbar/s, and 5.41 ± 1.19°, respectively, in the left lung, and 167.55 ± 43.35 mbar, 6.35 ± 1.00 mbar/s, and 5.25 ± 1.04°, respectively, in the right lung. In the experimental animals, the values of p_o, R, and α in the ischemic lung were 244.85 ± 19.28 mbar, .017 ± 0.40 mbar/s, and 5.321 ± .50°, respectively. In the contralateral normal lung, results show values for p_o, R, and α of 149.10 ± 15.54 mbar, 4.42 ± 1.07mbar/s, and 5.13 ± .74°. The statistical analysis revealed significant different values of p_o between the ischemic lung and the contralateral normal side, as well as between the ischemic lung and both sides of the control lungs. In the case of the oxygen depletion rate, R, there were statistically different values between the ischemic lung and the contralateral side. Further, we found significant differences between both control

lungs and both experimental lungs, but no differences between the left and right control lungs. We found no statistically significant differences in measurement of α between any groups.

We performed simulations to ascertain the ability of the measurement to detect varying amounts of ischemia based on the SNR of the initial imaging. Figure 4a and b plots the average and standard deviation for fits of p_o and R as a function of SNR at no ischemia (p_o = 149.10mbar, R=4.42mbar/s), 45% ischemia (p_o=216.19mbar, R=2.42mbar/s), and 90% ischemia (p_o=283.29mbar, R=0.44mbar/s). The minimum SNR required to separate p_o and R, respectively, at each level of ischemia from the normal case is summarized in Table 4.1 and 4.2.

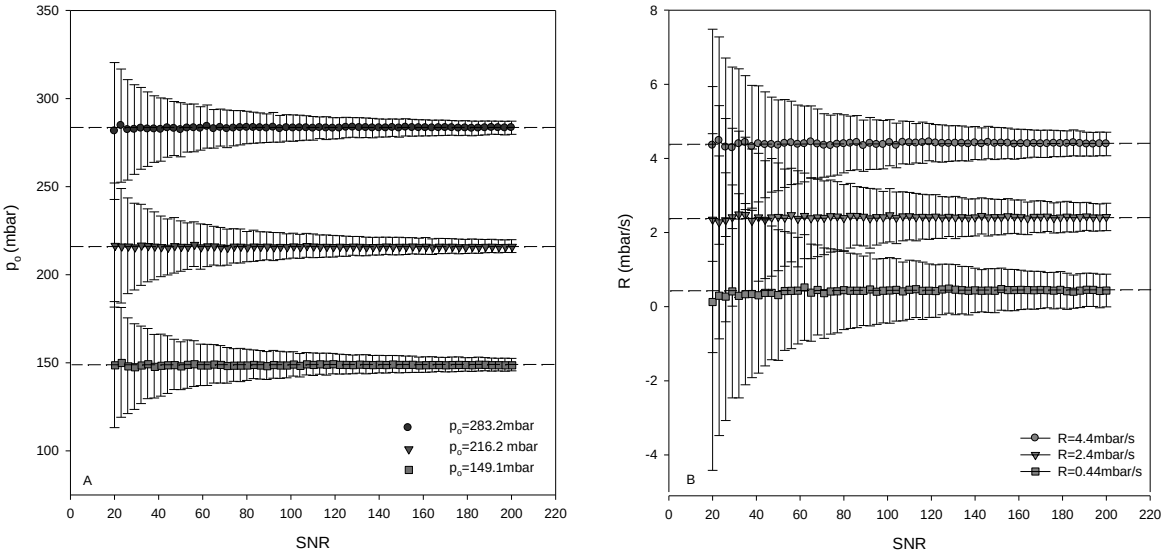

Figure 4.4 Simulated accuracy and precision of the measurement of A) p_o at 149.10 mbar, 216.19 mbar, and 283.29 mbar and R at 4.42 mbar/s, 2.42 mbar/s, and 0.44 mbar/s. Higher values of pO_2 and lower values of R are characteristic of pulmonary ischemia. Whereas both measures are accurate, p_o is considerably more precise then R. The dashed line represents the actual simulated value of p_o and R.

p_o (mbar)	p_o (mbar)						
	149.10	171.46	193.83	216.19	238.56	260.92	283.29
149.10	NA	125	65	43	32	26	23
171.46	125	NA	127	64	43	33	27
193.82	65	127	NA	128	64	44	33
216.19	43	64	128	NA	124	64	44
238.56	32	43	64	124	NA	126	66
260.92	26	33	44	64	126	NA	128
283.29	23	27	33	44	66	128	NA

Table 4.1 Minimum SNR required to separate the values of p_o indicated by the row and column. NA: Not applicable

R (mbar/s)	R (mbar/s)						
	4.42	3.74	3.08	2.42	1.76	1.1	0.44
4.42	NA	>200	196	134	104	87	75
3.74	>200	NA	>200	>200	142	110	90
3.08	196	>200	NA	>200	>200	147	117
2.42	134	>200	>200	NA	>200	>200	157
1.76	104	142	>200	>200	NA	>200	>200
1.1	87	110	147	>200	>200	NA	>200
0.44	75	90	117	157	>200	>200	NA

Table 4.2 Minimum SNR required to separate the values of R indicated by the row and column. NA: Not applicable. >200: SNR higher than 200 is required to separate the specified values of R. Simulation was not performed above SNR = 200.

4.5 Discussion

In this study, we showed that pulmonary ischemia in rats is detectable using the oxygen sensitivity of HP-He through the monitoring of signal decay. Further, we showed that both the p_o and R show large changes in areas of ischemia versus the contralateral side. To our knowledge, this represents the first demonstration of the sensitivity of the HP-He alveolar oxygen measurement conducted in a small animal model of permanent pulmonary ischemia.

Our model results in severe pulmonary ischemia that encompasses a majority of the occluded lung, as evidenced by the angiographic data. As compared to the contralateral lung, this occlusion results in both significantly elevated p_o and a reduced rate of oxygen uptake in the ischemic lung. These results further confirm the findings in other studies performed in large animal models of pulmonary ischemia. In previous small mammal models of pulmonary ischemia, investigators injected varying sized beads or homogenized clots into the venous system of rats (65,122,128). This produced a permanent and diffuse pulmonary ischemia. Crémillieux et al. infused air into rats in the decubitus position, which resulted in a one-sided, whole-lung pulmonary embolism (79). The ischemia dissipated over time, resulting in a transient insult. Our model is both focal and permanent, allowing for the study of stable ischemia.

One contradictory finding of our study is that the oxygen depletion rate in the contralateral side in experimental animals was significantly lower than that of both sides of the control animals. A possible explanation for this is that the process of catheterizing

the pulmonary artery affects cardiac function. Further, the catheterization of the superior vena cava reduced the preload on the heart which may reduce the cardiac output. Indeed, we observed a reduction in the heart rate following surgery. Indeed, Möller et al. showed a relationship between p_o and R to cardiac output (15). Nevertheless, the difference of both R and p_o between the ipsilateral and contralateral sides in experimental animals was significantly larger than those between the two sides of the control animals.

The simulation results revealed the importance of the SNR of the images in differentiating between normal and ischemic tissue in cases of mild and moderate ischemia. Simulation revealed both high accuracy and high precision of the experimental measurements of p_o at experimentally relevant SNR at all levels of ischemia. This was in contrast to the measurement of R, where a reduction in the oxygen uptake due to ischemia resulted in a decrease in measurement precision. The accuracy of the measurement of R, however, was quite robust at experimentally relevant SNR values.

According to our simulations, the SNR of the images obtained would allow for robust detection of changes in p_o and R, of at least 15% and 60% of normal, respectively. Mild, moderate, and severe ischemia can be differentiated from normal function on the basis of $p_{o,}$ whereas R can only differentiate between normal function and severe ischemia. The results suggest that p_o may be a more reliable parameter to use when attempting to differentiate between the severities of ischemia.

In order to improve the usefulness of R as a sensitive parameter of ischemia, an improvement of SNR of the images must be achieved. Higher SNR can be realized by

increasing the gas polarization, lowering the acquisition matrix, or increasing the flip angle. Increasing the flip angle of the imaging sequence will result in higher signal intensity, but may limit the number of useable images in the time course of the HP-He decay. This approach can be combined with a non-Cartesian k-space acquisition technique, such as spiral k-space mapping to lower the effect of using higher flip angles by sparsely sampling k-space (16).

The usefulness of this method in characterizing pulmonary embolism is two-fold. First, the measurements reflect the true physiology of the lung—the transfer of oxygen from the air spaces to the blood supply. Although many methods exist to measure blood perfusion to pulmonary tissue, few can assess the overall condition of lung function. Second, because this method uses no injected contrast agents, it is repeatable over the time course of the disease and following treatment. This feature will allow for comparative testing of pharmaceutical intervention on the ability to restore perfusion and normal pulmonary function following ischemia.

Other measures have been proposed to evaluate pulmonary ischemia using proton and non-proton methodology in rats. Mistry et al. suggested using multiple injections of contrast agent timed to the respiratory and cardiac cycle to obtain a bolus-contrast time curve in the lungs (81). Similarly, Dimitrov et al. suggested observing the de-phasing of the helium signal following injection of contrast agent (85). Both methods allow for mapping of the pulmonary blood flow in the lungs. Whereas it is sensitive to ischemia, the former method requires a technically challenging setup to inject contrast agent.

Further, both measures only look at blood flow to the tissue. The oxygen sensitivity measurement quantifies the actual physiology of the lung tissue (i.e., the transfer of oxygen from the airspace to the lung). To see the effect of restoration of blood flow on pulmonary function, it may be advantageous to measure blood perfusion using a contrast or arterial spin-labeling technique, and to measure pulmonary function using the oxygen sensitivity measurement in treated tissue. Pulmonary reperfusion is typically accompanied in edema, which may not allow the lungs to return to full function even though perfusion has been restored (129).

This study had limitations. Whereas our animal model of ischemia caused localized deficits, the deficits were large. Further, the ischemia was produced through the injection of non-biologic material. The model should be refined to use thrombi to cause ischemia that is treatable by thrombolytic compounds. From an imaging prospective, whole volume (projection) imaging was performed on the lung to measure the signal decay to ameliorate the diffusional motion of helium on the measurement. Future research should look at three-dimensional helium acquisitions to more finely localize the ischemic area, as suggested by Gast et al. (87). Finally, the quantitative values of p_o may be underestimated. As mentioned in the Crémillieux et al., a delay in the time between complete administration of the helium may result in the underestimation of p_o due to uptake of oxygen during this time (79). In the current study, the duration between the beginning of the breath-hold period and the start of the scan was between 4 and 5 seconds; this may have resulted in an underestimation of the p_o between 25.60 to 32.00 mbar.

In conclusion, our results demonstrate that the p_o and R, as measured by the T_1 decay of HP-He, is sensitive to pulmonary ischemia in rats. This finding can be useful in understanding the effects of pulmonary ischemia on lung function in rodents, and may eventually be used to ascertain the effect of treatment on the recovery of lung function.

Chapter V: Imaging Characterization of Pulmonary Blood Volume in Rats during a Hypoxic Challenge

Ronn P. Walvick, Austin L. Reno, Alexei A. Bogdanov Jr., Mitchell S. Albert

From the Department of Radiology, University of Massachusetts Medical School, Worcester, MA 01604

5.1 Preface

Tissue blood volume can be determined from the change in T1-weighted Magnetic Resonance (MR) signal intensity due to the injection of a strictly intravascular contrast agent. This study was designed to elucidate the optimal imaging parameters for measurement of pulmonary blood volume (PBV) in rats using simulations and utilize these parameters to measure the change in PBV during hypoxia, a well known pulmonary vasoconstriction stimuli. My contributions to this work include running simulations, animal handling, experimental design, collecting and analyzing MR data, and principle authorship of the manuscript.

5.2 Abstract

Objective: The purpose of this study was to develop a novel magnetic resonance imaging (MRI) based technique for the measurement of pulmonary blood volume. The method was evaluated via simulation and validated through animal experiments utilizing a model of pulmonary hypoxic vasoconstriction.

Methods: The proposed method consisted of acquiring images of lung parenchyma with an inversion recovery, T1 weighted spin-echo sequence before and after the injection of a long half-life, intravascular contrast agent. Simulation was performed to characterize the accuracy and precision of this methodology. Images of lung parenchyma were acquired in Sprague Dawley rats subjected to either inspiration oxygen level of 60% or 14%.

Results: Simulation revealed good accuracy and precision of the measurement at relevant signal to noise ratios. Better accuracy was obtained with shorter inversion times while the precision of the measurement was increased with higher inversion times. The results from the animal experiments revealed a significant decrease in the measured pulmonary blood volume in animals breathing gas with lower oxygen content. The measured PBV increased with increasing inversion time, in line with simulations.

Conclusion: The results presented here showed the utility of this methodology for measuring the pulmonary blood volume imaging in animal models of hypoxic pulmonary vasoconstriction. The measurement of pulmonary blood volume using MRI may have a role in both experimental and clinical imaging of pulmonary vascular function.

5.3 Introduction

Microcapillary pulmonary blood volume (PBV) is a sensitive measurement of pulmonary vascular physiology (130-132). Pulmonary blood volume constriction is thought to be a natural response to alveolar hypoxia (57). Further, PBV is regionally reduced due to ischemia as a result of pulmonary embolism (133).

Measurement of PBV can be performed in a number of ways. PBV can be measured by ascertaining the diffusing capacity of carbon monoxide (DL_{CO}) using spirometry (48). Following inhalation and breath hold of CO, the concentration of CO in the expiratory gas can be measured and compared to the inhaled concentration. The uptake of carbon monoxide is related to the PBV. This measurement offers only a global measurement of the pulmonary blood volume (48).

Spatially localized techniques utilizing imaging allows for a regional determination of PBV. Nuclear Medicine techniques such as single photon computed tomography (SPECT) has the ability to measure the distribution of an intravascular radiotracer, technetium-99m macroaggregates of albumin ([^{99m}Tc]MAA) through the pulmonary vasculature (77). The distribution of the radiotracer in the lungs is related to the PBV.

While nuclear medicine based exams offer spatially localized measurements of pulmonary blood volume, magnetic resonance imaging (MRI) may have the ability to measure PBV without the use of ionizing radiation. Steady state techniques, analogous to SPECT determination of blood volume, measure changes in the MRI relaxation properties of tissue before and after injection of an intravascular contrast agent. In one set

of techniques, a gadolinium based contrast agent is used in conjunction with a T_1 weighted inversion recovery or spoiled gradient echo sequence. These techniques have been used to measure many disease processes such as cancer and stroke (134-136).

The purpose of this study is to adapt the MRI based T_1 weighted steady state blood volume technique for the measurement of PBV. The typical implementation of these techniques, however, is not suited for measurement of pulmonary blood volume. These sequences are gradient echo based which results in low signal from the lung parenchyma due to the extremely short T_2* relaxation (134,135). Further, because of respiratory and cardiac motion, a physiological gating scheme must be implemented.

We propose the use of a T_1 weighted, inversion recovery prepared sequence with spin echo acquisition imaging to optimize the signal from the lung parenchyma. Although the lung parenchyma has a short T_2*, the T_2 of the lungs is on the order of 60-80ms, making spin echo sequences appropriate for lung imaging (137). Further we describe a gating scheme which will allow for maintenance of the steady state magnetization for accurate blood volume measurements. Simulation will be conducted to explore the tradeoff between inversion time and the effect of water exchange on measure of PBV. Also, the accuracy and precision of the exam will be determined as a function of physiological and imaging parameters. The measurement of PBV will be applied to measure the PBV in Sprauge Dawley rats breathing either 60% or 14% O_2 to explore the ability of our method to measure PBV and its changes during HPV. We hypothesize that 1.) the accuracy and precision of the PBV is dependent on inversion time and exchange

rate, 2.) the proposed MRI PBV measurement is sensitive to hypoxia, and 3.) the SNR of the lung parenchyma is adequate for the measurement of PBV.

5.4 Materials and Methods

5.5 Theory

Donahue et al. introduced the use of an inversion recovery prepared T_1 weighted pulse sequence for the measurement of capillary blood volume (138). In this technique, the authors utilized the Hazelwood model which relates the MRI signal intensity from the tissue, S_{tissue}, to inversion time, TI, the blood longitudinal relaxation time, T_{1v}, the extravascular relaxation time, T_{1ev}, water exchange rates between the intravascular and extravascular space ($\frac{1}{\tau_v}, \frac{1}{\tau_{ev}}$), the fractional intravascular and extravascular volume (f_v,f_{ev}) and longitudinal magnetization, M_o as (138,139):

$$S_{tissue}(TI) = f_v' M_o \left(1 - 2\exp\left(-\frac{TI}{T_{1v}'}\right)\right) + f_{ev}' M_o \left(1 - 2\exp\left(-\frac{TI}{T_{1ev}'}\right)\right) \quad [5.1]$$

where

$$f_v' = \frac{1}{2} - \frac{\frac{1}{4}\left[(f_{ev} - f_v)\left(\frac{1}{T_{1v}} - \frac{1}{T_{1ev}}\right) + \frac{1}{\tau_v} + \frac{1}{\tau_{ev}}\right]}{\frac{1}{2}\left[\left(\frac{1}{T_{1v}} - \frac{1}{T_{1ev}} + \frac{1}{\tau_v} - \frac{1}{\tau_{ev}}\right)^2 + \frac{4}{\tau_{ev}\tau_v}\right]^{\frac{1}{2}}}$$

$$f_{ev}' = 1 - f_v'$$

$$\frac{1}{T_{1v}'} = \left[\frac{1}{2}\left(\frac{1}{T_{1v}} + \frac{1}{T_{1ev}} + \frac{1}{\tau_v} + \frac{1}{\tau_{ev}}\right)\right] + \frac{1}{2}\left[\left(\frac{1}{T_{1v}} - \frac{1}{T_{1ev}} + \frac{1}{\tau_v} - \frac{1}{\tau_{ev}}\right)^2 + \frac{4}{\tau_{ev}\tau_v}\right]^{\frac{1}{2}}$$

$$\frac{1}{T_{1ev}'} = \left[\frac{1}{2}\left(\frac{1}{T_{1v}} + \frac{1}{T_{1ev}} + \frac{1}{\tau_v} + \frac{1}{\tau_{ev}}\right)\right] - \frac{1}{2}\left[\left(\frac{1}{T_{1v}} - \frac{1}{T_{1ev}} + \frac{1}{\tau_v} - \frac{1}{\tau_{ev}}\right)^2 + \frac{4}{\tau_{ev}\tau_v}\right]^{\frac{1}{2}}$$

In these equations, only the exchange affected parameters are measurable (T_{1ev}', T_{1v}', f_{ev}', f_v'). With estimates of the exchange rates, $\left(\frac{1}{\tau_v}, \frac{1}{\tau_{ev}}\right)$, one can obtain values for the exchange independent intra and extravascular longitudinal relaxation times and volume fractions. The terms intravascular volume and pulmonary blood volume are interchangeable in this report.

To simplify the calculation of vascular volume, assumptions can be made about the exchange rates. Donahue et al. has shown that using a model where $\frac{1}{\tau_v}, \frac{1}{\tau_{ev}} = 0$, the fractional blood volume can be determined by (138)

$$f_v = \frac{S_{tissue,post} - S_{tissue,pre}}{S_{blood,post} - S_{blood,pre}} \quad [5.2]$$

where $S_{tissue,pre}$ and $S_{tissue,\ post}$ is the signal intensity in the lung parenchyma before and after contrast injection and $S_{blood,pre}$ and $S_{blood,\ post}$ is the signal intensity from the blood before and after contrast injection.

This 'no exchange model' has been shown to produce accurate measurements of fractional blood volume even in domains of high exchange. The alternative 'fast exchange model' assumes $\frac{1}{\tau_v}, \frac{1}{\tau_{ev}} = \infty$. The calculation of f_v in this model requires the measurement of the longitudinal relaxation time prior to and following injection of a contrast agent (138). Accelerated methods of mapping the longitudinal relaxation time exist but usually require the utilization of a gradient echo readout which is difficult to implement in the lungs. Therefore, we will utilize the 'no-exchange' model in our measurement of PBV.

5.5.1 Simulation

Simulation will be used to determine the effect of inversion time, water exchange rate and SNR of the images on the accuracy and precision of the blood volume measurement. The pre and post contrast injection signal intensity will be simulated by calculating equation 5.1 using assumed values of T_1 for the intravascular space before and after contrast injection. The signal from blood will be calculated as

$$S_{blood} = M_o\left(1 - e^{\frac{-TI}{T_{1v}}}\right) \quad [5.3]$$

Table 1 lists the various parameters for simulation.

The addition of noise will be simulated by varying the signal intensity of the pre and post contrast by

$$S_{tissue,noise} = S_{tissue} + \frac{1}{SNR}n \quad [5.4]$$

where n is a random number generated from a Gaussian distribution with $\mu=0$ and $\sigma=1$. Equation 5.3 assumes the magnetization (M_o) is equal to 1. For purposes of simulation, the SNR refers to the achievable SNR if the inversion time approached 0 seconds. The fractional blood volume will be calculated by equation 5.1 using the noise adjusted signal intensities. For each set of inversion times and exchange rates, the simulation was performed 1000 times and the average and standard deviation of the simulated values were reported.

Parameter	Value
Precontrast Blood T_1 (T_{1v})	1.664s
Post Contrast Blood T1	0.215s
Extravascular Tissue T_1	0.874s
Fractional Blood Volume(f_v)	.3
Extravascular Blood volume(1-f_v)	.7
Inversion Time(TI)	.1-.6s
Exchange Rate ($1/\tau$)	1-30Hz
Initial Magnetization (M_o)	1
Lung Parenchyma SNR	20-200

Table 5.1Parameters used for blood volume imaging simulation

5.5.2 Animal Experiments

Animal procedures were approved by the University of Massachusetts Institutional Animal Care and Use Committee. 10 Sprague Dawley rats were injected subcutaneously with 5uL/g B.W. of a mixture of 100mg/ml Ketamine and 20mg/ml Xylazine. Once an acceptable plane of anesthesia was achieved, animals were fitted with a tail vein and subcutaneous catheter for administration of contrast agents and anesthetics, respectively. Following the initial anesthesia, animals were administered a maintenance dose of 1uL/g B.W. of the Ketamine and Xylazine mixture every 30-40 minutes.

Following catheter placement animals were transferred to a 3.0T Philips Acheiva Clinical MR scanner for imaging. Animals were connected to a closed anesthesia circuit that allowed for spontaneous respiration. Animals were continuously warmed with a hot air small animal heating system. Physiological monitoring was conducted using an MR-compatible small animal monitoring device (SAI, Stonybrook, NY). Animals were exposed to breathing gas of either 60% O_2 (n=5) or 14% O_2 (n=5) during imaging.

5.5.3 MRI Methods

Animals were placed in the center of a Single Turn Solenoid RF coil tuned to the ^{1}H frequency. A solution of 20% Magnevist was placed next to the animal as a signal standard. Animals were positioned in the center of the magnet and positioning was confirmed with a localizing scan. For measurement of blood volume, an inversion recovery, spin echo sequence was used with the following parameters: TI = 100, 200, or 300ms, TR = 6s, TE= 4.95ms, NSA =2, matrix Size = 128x64, slice thickness = 3mm,

and Field of View = 50mm. Images were interpolated to a matrix size of 128x128. In order to minimize physiological imaging artifacts, a simultaneous cardiac and respiratory gating scheme was implemented. To achieve image read out during mid cardiac cycle and end expiration, a trigger was administered to the scanner at a time equal to TI before image readout. The appropriate point to trigger the scanner was predicted by the recent historical heart rate and respiratory rate of the animal. Figure 1 graphically describes this process.

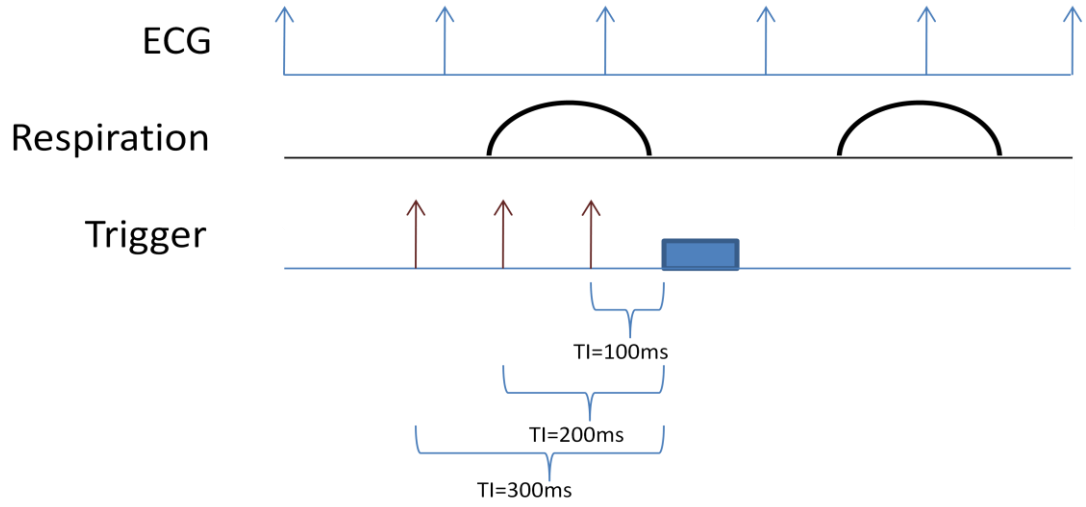

Figure 5.1Prospective gating scheme. A trigger is received by the scanner from the small animal gating device TI miliseconds before the desired signal readout. The readout occurred during the mid cardiac cycle and end expiration.

Images were recorded with different inversion times prior to injection of an intravascular contrast agent, gadolinium-labeled protected graft copolymer (PGC-Gd). The agent has a measured half life in rodents of 14 hours with a relaxivity of 10-11 $(mm \cdot s)^{-1}$ at a dose of 30umole Gd/kg. Following a five minute weighting period to allow for contrast agent circulation, the animal was reimaged with the identical imaging protocol. The effectiveness of the cardiac and respiratory gating scheme was evaluated by

subtracting images acquired at the same inversion time. Misalignment of the heart and the pulmonary space were evaluated.

5.5.4 Data Analysis

Differences in physiological parameters (heart rate, respiration rate, and Oxygen Saturation (SPO_2)) were evaluated using a one tailed Student's t-test with equal variance. Values of $p<.05$ were considered significant.

Region of Interests (ROIs) were be selected in the ventral and dorsal area of each lung. Care was taken to avoid blood vessels and airways. An ROI were placed around the pulmonary artery vessel for measurement of $S_{blood,pre}$ and $S_{blood,post}$. Finally, an ROI was placed around the phantom. The signal intensity of the ROIS from post contrast images was corrected for arbitrary changes in intensity via:

$$S_{ROI} = S_{ROI} - (S_{phantom,post} - S_{phantom,pre})$$

Where $S_{phantom,post}$ and $S_{phantom,pre}$ is the SNR before and after contrast injection. All values for signal intensity are adjusted for signal phase by comparing the sign of the intensity on images reconstructed to display real values on the post contrast images to that of pre contrast images

The corrected post and pre signal intensities will be used to calculate the PBV for each tissue ROI using equation 5.2. The blood volume measurements will be evaluated by a 3-way analysis of variance (ANOVA) to ascertain the effect of inversion time, anatomical position (ventral versus dorsal), and hypoxia on the PBV. A post-hoc Bonferroni multiple comparison analysis of the effect of inversion time on the PBV was conducted. Values of $p<.05$ was considered significant. Values of PBV are expressed as a

ratio between capillary PBV and pulmonary tissue volume (i.e., PBV + septal wall volume).

The SNR of the pre-contrast image ROIs were calculated to determine the effects of hypoxia and inversion time on signal intensity. SNR was calculated by dividing the average signal intensity within the ROI by the standard deviation of the noise. The average values of SNR were evaluated with a 2-way ANOVA with hypoxia and inversion time as factors. A post-hoc Bonferroni multiple comparison analysis of the effect of inversion time on the SNR was conducted. Values of $p<.05$ was considered significant.

5.6 Results

5.6.1 Simulation

The simulated average and standard deviation of the measurement of PBV at short and long inversion time and an SNR level of 80 as a function of water exchange rate is given in Figure 5.2. The error in the measurement of PBV is increased as the inversion time is increased. Higher water exchange between the intra and extravascular space results in an increase in the error on the measurement of the PBV independent of inversion time. The error caused by exchange exhibits asymptotic behavior as higher exchange rates are realized. With increasing inversion time, the sensitivity of the measurement of PBV to exchange rate is increasingly severe. Although the measurement error increases with increasing inversion time, the precision of the measurement of PBV increases with increasing inversion time. Table 5.2 summarizes the results of the simulation.

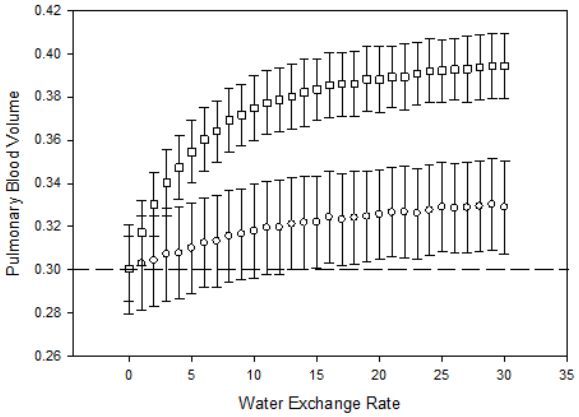

Figure 5.2 Results of simulation showing the accuracy and precision of the measurement of blood volume at inversion times of 100ms (circles) or 600ms(squares) as a function of exchange rate.

	Inversion Time		
Exchange Rate	100ms	300ms	600ms
0Hz	.30±.03	.30±.02	.30±.01
5Hz	.30±.03	.32±.02	.35±.01
10Hz	.31±.04	.33±.02	.38±.02
15Hz	.31±.04	.34±.02	.38±.01
20Hz	.31±.04	.34±.02	.39±.02
25Hz	.31±.04	.35±.02	.39±.01
30Hz	.31±.03	.35±.02	.39±.01

Table 5.2 Simulated pulmonary blood volume measurements as a function of inversion time and exchange. The actual simulated blood volume is .30. PBV is measured in units of ml of blood/ml of tissue.

In animal experiments, we chose to interrogate inversion times equal to 100, 200, and 300ms to minimize the effects of exchange on the measurement error of PBV (see discussion section).

5.6.2 Animal Experiments

All animals tolerated anesthesia and hypoxia without adverse events. Animals breathing 14% and 60% inspired O2 exhibited a blood oxygen saturation of 64.00±5.29% and 97±3.464% and a heart rate of 330±43.48 beats per minute and 284.75±29.25 beats per minute respectively. The respiration rate for animals breathing 14% and 60% O2

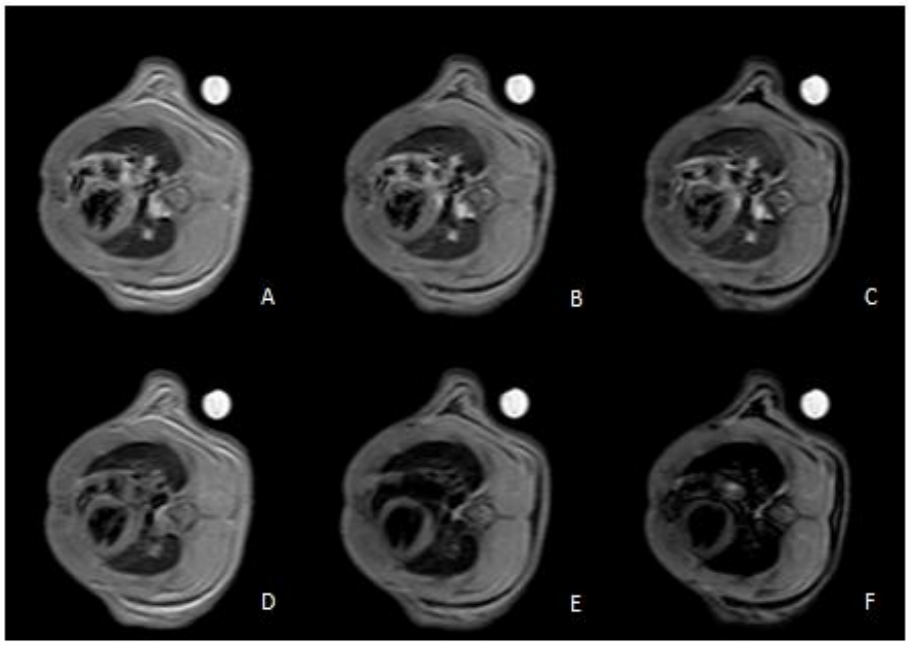

Figure 5.4Images of rat lung parenchyma at TI=100(A, D), 200(B, E) and 300 (C, F) at pre (A-C) and post (D-F) contrast administration in a normal animal.

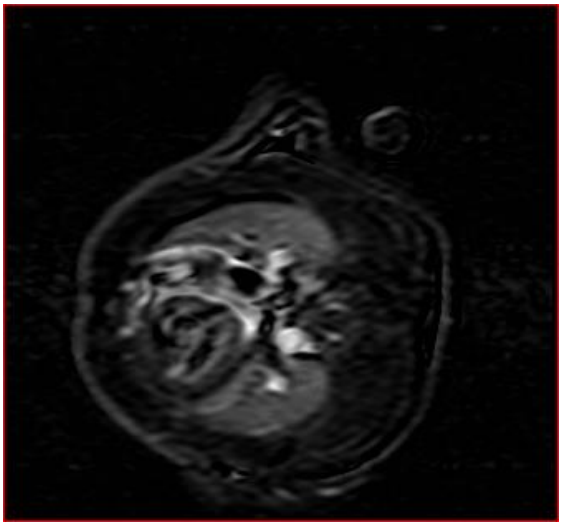

Figure 5.3Subtraction image of images shown in Fig 5.5C and F. Signal enhancement is clearly visible and no major misalignments of the images are visible.

83±4 and 73.75±21, respectively. A decrease in SPO_2 ($p < .05$) with hypoxia while no difference in heart rate ($p > .05$) or respiration rate ($p > .05$) was observed. Figure 5.3 shows typical images of an animal breathing 60% O_2 before and after contrast injection at different inversion times. Lung parenchyma was clearly visible in these images and motion artifacts were minimized. Figure 5.4 displays a typical subtraction of image from Figure 5.3C and 5.3F. No major misalignment of the images was observed.

Analysis of the PBV revealed a statistically significant reduction of PBV with hypoxia ($p < .05$). The average PBV as a function of hypoxia and inversion time is given in table 5.3. The analysis revealed a significant effect of inversion time on the measurement of blood volume ($p < .05$).

	Inversion Time		
Inspired O_2	100ms	200ms	300ms
14%	.08±.12	.16±.07	.27±.09
60%	.28±.08	.33±.085	.38±.0717

Table 5.3 Effect of inversion time and inspired O2 on pulmonary blood volume. Data is expressed as ml of blood/ml of tissue.

A post hoc analysis of the effect of inversion time on PBV reveals a significant increase in the PBV as inversion time is increased (TI=100ms vs. TI=200ms, $p < .05$, TI=200ms vs. TI=300ms, $p < .05$, TI=100ms vs. TI=300ms, $p < .05$). There was no significant interaction effect between hypoxia and inversion time. Analysis further revealed no statistical change in PBV between the ventral and dorsal PBV ($p > .05$).

The average SNR of the selected ROIs as a function of inversion time and inspired oxygen content is given in table 5.4. There was no effect of inspired oxygen concentration on the parenchymal SNR($p>.05$), however, inversion time did have an effect on SNR ($p<.05$). A post-hoc analysis revealed that only the values of SNR from TI=100ms and TI =300ms are statistically significant; however, the data indicates a trend towards decreasing SNR with increasing inversion time. There was no interaction effect of inspired oxygen concentration and inversion time on the values of SNR.

	Inversion Time		
Inspired O_2	100ms	200ms	300ms
14%	93.1876±19.54	80.93±18.79	69.52±10.05
60%	96.25±28.48	86.13±32.08	73.67±32.08

Table 5.4 Effect of inversion time and inspired O_2 on precontrast SNR

5.7 Discussion

In this report, we present results that show the feasibility of measuring microcapillary pulmonary blood volume using a T_1 weighted, inversion recovery sequence using cardiac and respiratory gating. Our results show that PBV as indicated by our measurement is restricted as a response to alveolar hypoxia. We further demonstrate through simulation the importance of the selection of inversion time in the accurate and precise measurement of PBV.

Our simulation results reveal the tradeoff between inversion time and the accuracy and precision of the PBV measurement. The accuracy of the measurement is reduced due to both exchange and increasing inversion time. Water exchange between the intravascular and extravascular compartment cause a 'blurring' of the respective T_1 relaxation times resulting in a loss of accuracy of the measurement of PBV. It is therefore necessary for accurate measurements to use minimal inversion times. In counter balance to this, the precision of the measurement is reduced with shorter inversion times. At shorter inversion times, the absolute range of the signal change expected between pre and post contrast images is low at biologically relevant tissue blood volume ratios. It should also be noted that the improvement in precision is asymptotic as inversion time is increased.

The result of reduced PBV during alveolar hypoxia in the animal experiments confirms the results of other investigations of PBV during hypoxia using both invasive and non-invasive methods. Intravital fluorescence microscopy has been utilized to visualize vessel constriction during hypoxia. In one study, the authors measured the

response of diameter of medium and small diameter arterioles in mice. The diameter of these vessels reduced in response to hypoxia, although capillary diameter response was not measured (140). Further, in a model of regional airway obstruction, Mistry et al. observed a large decrease in the regional PBV corresponding to the airway obstruction (81). Other studies have indirectly observed HPV by observing changes in pulmonary artery pressure or pulmonary vascular resistance (141).

In the animal experiments, we chose to investigate inversion times of 100, 200, and 300ms. Although the expected precision was low at these inversion times, selecting ROIs increased the number of voxels sampled and lowered the effect of measurement precision. Further, at SNR levels of the images were of sufficient level to produce an expected measurement standard deviation of between 5-15% as the inversion time increases from 100ms to 500ms according to the simulation.

The results of values for PBV in the animals breathing 60% O_2 slightly underestimate those reported in the literature. The average value for PBV in this group of rats measured at TI=100ms were used for a reference due to the minimal effect of exchange on the measurement. In a study by Burri et al., the ratio of capillary blood volume to septal volume (pulmonary tissue + capillaries) in mature rats was .357 (measure derived by experimentally measured capillary volume of (.197±.030) divided by experimentally measured tissue volume of .551±.051) as measured by autoradiography versus .282 measured by the proposed method (142). In another study by Plopper et al. the ratio of pulmonary capillary volume to pulmonary tissue volume to .303 (measure derived by experimentally measured capillary volume of (.087±.015) divided

by experimentally measured tissue volume of .287±.017) as determined by light microscopy techniques (143).

The effect of water exchange on the measurement of PBV using the proposed technique may be particularly problematic due to the nature of pulmonary capillaries. To support efficient gas exchange, both capillary and alveolar walls are very thin. The thin capillary wall may reduce the barrier to water exchange between the intravascular compartment and the alveolar interstitial space. To our knowledge, direct measurements of non-osmotic water exchange between these compartments have not been directly performed. The experimental results obtained in this study suggest the exchange rate between the compartments may be high as indicated by the response of the measurement to increasing inversion time. As shown in simulation, increasing inversion times increases the observed measurement of PBV at higher levels of exchange. In this study, progressively higher inversion time resulted in large increases of PBV in both animal groups, although the magnitude of the increase was smaller in the group breathing 60% O_2 then in the hypoxic group. This may reflect capillary wall modification during acute HPV.

Pulmonary edema, a common co-occurrence with pulmonary disease, likely did not play a role in the reduced observed values of PBV in the hypoxic group. Pulmonary edema during alveolar hypoxia would result in an increase of the T_1 in the extravascular compartment. Over the duration of the experiment, the severity of the edema may increase, resulting in a lower observed value of the PBV. Previous research in HPV

pathophysiology has shown that HPV does not result in pulmonary edema during the acute state (140).

In this study, our imaging protocol had a total imaging time of 12.8 minutes per inversion time point. In order to improve the imaging speed, a centric reordered turbo spin echo sequence (cTSE) could be utilized for readout in place of the single echo acquisition. cTSE sequences have been successfully used for lung imaging in humans and in animals. Further, in this study, we acquired a single slice. A multislice approach is feasible; however, a number of considerations must be taken into account. First, each slice must be taken at the same point in the cardiac cycle. Previous studies have shown that pulmonary blood perfusion changes during the cycle (144). Secondly, Each slice must be recorded at the same inversion time for regional comparison of PBV. One solution may be a three dimensional acquisition which would take advantage of the cTSE readout to accelerate image acquisition.

The proposed measurements of PBV may be useful in the study of a number of disease processes. Many pulmonary diseases result in vascular dysfunction. In severe cases of chronic pulmonary obstructive disease (COPD), patients experience pulmonary arterial hypertension (PAH) due to HPV (52-54). Invasive measurements of pulmonary artery pressure, commonplace in the monitoring of PAH, can be replaced with the proposed methods to evaluate the regional effect of treatment on the microcappilaries of the lungs. Further emphysema may be a promising disease to study with this protocol. Emphysema is characterized by a thinning of the alveolar wall (145). This would increase the fraction of the MR signal from the lungs associated with the intravascular space and

would be reflected as an increase in the PBV. Further, the destruction of the alveolar wall may result in an increase in the rate of water exchange between the vascular and extravascular spaces. Monitoring the PBV at progressively higher inversion times might yield information about this process.

Although this method was tested in a rodent model of alveolar hypoxia, the method is easily translatable to clinical imaging protocols. While the contrast agent used in this study is restricted to preclinical imaging, the Food and Drug administration recently approved an intravascular contrast agent, gadofosveset trisodium (Ablavar©), for use in the clinic (146). Further, in combination with accelerated image acquisition use cTSE, breath hold imaging can potentially be conducted to completely ameliorate the effects of respiratory motion.

In conclusion, we show the utility of proton based PBV measurements. The proposed methodology utilizes a cardiac and respiratory gated inversion recovery spin-echo sequence to maximize the SNR from the lung parenchyma. We used an intravascular contrast agent to ascertain the PBV without the need for fast imaging necessary for DSC or DCE PBV measurement techniques. We have demonstrated this techniques sensitivity to HPV. Steady state MRI measurement of PBV may be useful for investigations of lung vascular physiology and disease.

Chapter VI: Summary and Future Work

This dissertation characterizes MRI techniques in the measurement of the effect of experimental models of disease on the neural and pulmonary vasculature of rodents. The work presented in this thesis creates a base for future research in detailing the physiological mechanisms of disease states and the effect of administration of experimental pharmaceutical treatments on the progression of disease. The following chapter will summarize the main findings of the experiments described in this thesis and offer suggestions for future research directions.

Chapter 3 of this dissertation provides a comparison of a continuous arterial spin labeling (CASL) perfusion imaging technique with a dynamic susceptibility contrast (DSC) perfusion technique in a rat model of experimental stroke. Utilizing a combination of CASL derived cerebral blood flow mapping, apparent diffusion coefficient mapping, and histology, stroke subregions were segmented (core, penumbra, sustained reversal, and transient reversal). Measurements of DSC derived relative cerebral blood flow (rCBF) were recorded in each of the stroke subregions over a number of time points following ischemia and reperfusion. In animals with untreated stroke, the blood flow in the core and penumbra remained consistently low but constant. Following reperfusion, blood flow increased to both the core and penumbral subregion. Further areas designated as transient reversal had a higher although non-statically significant response to reperfusion then did areas of sustained reversal. Finally, the results show that blood flow during ischemia is higher in areas of penumbra and sustained reversal. Using the data obtained from the stroke subregions, a minimum threshold for rCBF derived

ischemia was derived. This threshold was used to calculate ischemic tissue volumes which were comparable to those derived from CASL.

The results presented in this work are useful to the preclinical stroke research community. We showed the utility of DSC for the determination of ischemic lesion volume in experimental rat models of stroke. While CASL based methods are advantageous in many ways, the technical challenges of implementation are high and require specialized hardware. DSC based perfusion methods are technically straightforward and require only an intravenous catheter; however, further validation was necessary to support the use of DSC perfusion measurements in experimental stroke. The derivation of a threshold for DSC based determination of ischemia may allow for standardization of the measurements of the ischemic lesion in future experimental stroke research.

Clinically, research using contrast enhanced perfusion measurements in both CT and DSC based MRI have been interpreted using the arterial input function corrected bolus time to maximum contrast concentration (t_{max}) (147). In may be interesting to use a similar technique to map the response of t_{max} to stroke subregions both during acute stroke and subsequent reperfusion in an experimental model of stroke. In combination with histology and diffusion weighted imaging, the physiological meaning of t_{max} can be more thoroughly explored.

In chapter three of this dissertation, a method of labeling clots with a T_1 contrast agent, Gd-DTPA, was demonstrated. Clots were created with different concentrations of

contrast agent and the optimal concentration for signal enhancement was determined. Following optimization, clots were injected into the cerebral vasculature of rats to induce cerebral ischemia. Clots were easily visualized in the area of the junction between the internal, anterior, and middle cerebral artery. In untreated animals, *in vivo* measurements of clot length were consistent over time. In animals treated with thrombolytic agents, clot length decreased over time. These results were confirmed using histological visualization of the clot. This method was used to compare the thrombolytic efficacy of recombinant tissue plasminogen activator (r-tPA) with a combination of r-tPA and recombinant annexin-2 (rA2). Our results show that the combination of rA2 and r-tPA resulted in more efficacious clot lysis, although this did not lead to a statistically lower final volume of infarcted tissue.

The presented method of clot visualization can be used in a number of ways for future experimentation. One interesting area of study would be to explore the rate of clot lysis as it compares to the rate of reperfusion. This would be helpful in further elucidating the physiological mechanisms of the 'no-reflow' phenomenon where recanalization of large vessels can occur without complete microcapillary reperfusion (34,35). Further, there has been a recent push to develop new thrombolytic compounds that ameliorate the risk of hemorrhage (148,149). The clot imaging methodology presented may be useful in evaluating the efficacy of novel experimental thrombolytic agents. In combination with other MRI parameters, the effect of these compounds on hemorrhage, infarct volume, and edema can also be determined.

In the second part of this dissertation, results were presented on two different methodologies for measuring pulmonary vascular function. Chapter four of this dissertation shows the results of simulation and experimentation on the use of the oxygen sensitivity of hyperpolarized ^{3}He (HP-He) to measure the efficacy of gas exchange between the lungs and the blood. We validated this method for use in monitoring the effect of ischemia on gas exchange in a rodent model of pulmonary embolism. Our results show an increase in the initial partial pressure of oxygen and a decrease in the rate of oxygen uptake from the airspaces to the capillaries in areas of ischemia. Simulation reveals that the measurement of the initial partial pressure of oxygen is a more sensitive measure of ischemia then is the rate of oxygen uptake.

The proposed methodology can be used to characterize the restoration of gas exchange following the administration of thrombolytic compounds to recanalize the pulmonary artery. As discussed in chapter one, an immune response accompanies reperfusion in an animal model of pulmonary embolism. Characterizing the temporal response of the recovery of pulmonary gas exchange in relationship to the immune reaction following reperfusion may be translatable to the clinic by providing a clearer understanding the consequences of administration of thrombolytics in cases of severe pulmonary embolism. This methodology also should be extended to research involving other experimental models of pulmonary disease. The time course and effect of treatment on gas exchange in experimental models of diseases such as emphysema or acute respiratory distress syndrome may facilitate a clearer understanding and better treatments for pulmonary disease.

In chapter five of this dissertation, we describe a novel methodology of measuring pulmonary blood volume (PBV) using proton based MRI with a cardiac and respiratory gated T_1 weighted inversion recovery spin echo sequence following the injection of an intravascular contrast agent. Results show that lung parenchyma in rats is visible using this methodology. Further, the measurement of blood volume was consistent with reports from the literature. Also, animals breathing a low concentration of oxygen have generalized reduced PBV, a result of hypoxic pulmonary vasoconstriction. Simulation reveals that imaging parameters play a role in the accuracy and precision of the measurement of PBV.

As suggested in chapter fiver, future work should focus on improving the imaging acquisition time by implementing fast spin echo sequences. Further, multislice acquisitions can be achieved using a three dimensional fast spin echo sequence. Also, the exchange sensitivity of the measurement of PBV may be useful in characterizing the integrity of the pulmonary capillary and alveolar wall. Kim et al. introduced a measure of vascular permeability, the water exchange index, to characterize vessel integrity (134). The water exchange index is calculated as the ratio of the measurement of blood volume between exchange sensitive and insensitive imaging sequences. Using our proposed methodology, calculation of the water exchange index can be achieved for the measurement of pulmonary and capillary wall integrity.

In conclusion, this dissertation presents methodology to measure rodent neural and pulmonary vascular function during normal and diseased states. In the first part of

this dissertation, the use of DSC in the measurement of experimental cerebral ischemia was validated in a model of permanent and transient ischemic stroke. Further, a method is described to visualize clot location and lysis in response to thromolytic compounds a rat model of embolic stroke. In the second part of this dissertation, the use of the oxygen sensitivity of HP-He is validated in a rat model of pulmonary embolism and through simulation. Finally, results are presented in the use of a novel lung imaging methodology for the measurement of pulmonary blood volume. The methods presented in this dissertation will aid investigators in understanding the pathophysiology are response to treatment of neural and pulmonary disease.

References

1. Bernstein MA, King KF, Zhou XJ. Advanced Pulse Sequence Techniques. In: Matt AB, Ph.D, Kevin FK, Xiaohong Joe Z, editors. Handbook of MRI Pulse Sequences. Burlington: Academic Press; 2004. p. 802-954.

2. McRobbie DW, Moore EA, Graves MJ, Prince MR. MRI from Picture to Proton: Cambridge University Press: 2007. 406 p.

3. Sotak CH. Class Notes from BME 582. Biomedical Engineering. Worcester: Worcester Polytechnic Institute; 2006.

4. Haacke E, M., Brown RW, Thompson MR, Venkatesan R. Magnetic Resonance Imaging: Physical Principles and Sequence Design: Wiley-Liss: 1999. 914 p.

5. Hornak JP. The Basics of MRI. Volume 2010: Interactive Learning Software; 2010.

6. Bloch F. Nuclear Induction. Physical Review 1946;70(7-8):460.

7. Karonen J, Nuutinen J, Kuikka J, et al. Combined SPECT and diffusion-weighted MRI as a predictor of infarct growth in acute ischemic stroke. J Nucl Med 2000;41(5):788-794.

8. Hosseinzadeh K, Schwarz SD. Endorectal diffusion-weighted imaging in prostate cancer to differentiate malignant and benign peripheral zone tissue. Journal of Magnetic Resonance Imaging 2004;20(4):654-661.

9. Schaefer PW, Grant PE, Gonzalez RG. Diffusion-weighted MR Imaging of the Brain1. Radiology 2000;217(2):331-345.

10. Kauczor H, Surkau R, Roberts T. MRI using hyperpolarized noble gases. Eur Radiol 1998;8(5):820-827.

11. Kober F, Wolf PE, Leviel JL, et al. Low-temperature polarized helium-3 for MRI applications. Magn Reson Med 1999;41(6):1084-1087.

12. Albert MS, Cates GD, Driehuys B, et al. Biological magnetic resonance imaging using laser-polarized 129Xe. Nature 1994;370(6486):199-201.

13. Walker TG. Spin-exchange optical pumping of noble-gas nuclei. Reviews of Modern Physics;69(2):629-642.

14. Johnson GA, Cofer GP, Hedlund LW, Maronpot RR, Suddarth SA. Registered ^{1}H and 3He magneti^{c} resonance microscopy of the lung. Magnetic Resonance in Medicine 2001;45(3):365-370.

15. Moller HE, Hedlund LW, Chen XJ, et al. Measurements of hyperpolarized gas properties in the lung. Part III: (3)He T(1). Magn Reson Med 2001;45(3):421-430.

16. Cieślar K, Stupar V, Canet-Soulas E, Gaillard S, Crémillieux Y. Alveolar oxygen partial pressure and oxygen depletion rate mapping in rats using 3He ventilation imaging. Magn Reson Med 2007;57(2):423-430.

17. Fischer MC, Spector ZZ, Ishii M, et al. Single-acquisition sequence for the measurement of oxygen partial pressure by hyperpolarized gas MRI. Magn Reson Med 2004;52(4):766-773.

18. Zhao L, Mulkern R, Tseng CH, et al. Gradient-Echo Imaging Considerations for Hyperpolarized 129Xe MR. J Magn Reson B 1996;113(2):179-183.

19. Deppe MH, Teh K, Parra-Robles J, Lee KJ, Wild JM. Slice profile effects in 2D slice-selective MRI of hyperpolarized nuclei. J Magn Reson 2010;202(2):180-189.

20. Tsai LL, Mair RW, Rosen MS, Patz S, Walsworth RL. An open-access, very-low-field MRI system for posture-dependent 3He human lung imaging. J Magn Reson 2008;193(2):274-285.

21. Parra-Robles J, Cross AR, Santyr GE. Theoretical signal-to-noise ratio and spatial resolution dependence on the magnetic field strength for hyperpolarized noble gas magnetic resonance imaging of human lungs. Med Phys 2005;32(1):221-229.

22. Association AH. Heart Disease & Stroke Statistics. Volume 2010; 2010.

23. Sloan MA. Thrombolysis and Stroke: Past and Future. Arch Neurol 1987;44(7):748-768.

24. Sweeney MI, Yager JY, Walz W, Juurlink BH. Cellular mechanisms involved in brain ischemia. Can J Physiol Pharmacol 1995;73(11):1525-1535.

25. Hossmann KA. Viability thresholds and the penumbra of focal ischemia. Ann Neurol 1994;36(4):557-565.

26. Paciaroni M, Caso V, Agnelli G. The concept of ischemic penumbra in acute stroke and therapeutic opportunities. Eur Neurol 2009;61(6):321-330.

27. Astrup J, Siesjo BK, Symon L. Thresholds in cerebral ischemia - the ischemic penumbra. Stroke 1981;12(6):723-725.

28. Kidwell CS, Wintermark M. The role of CT and MRI in the emergency evaluation of persons with suspected stroke. Curr Neurol Neurosci Rep 2010;10(1):21-28.

29. Murphy B, Fox A, Lee D, et al. Identification of penumbra and infarct in acute ischemic stroke using computed tomography perfusion-derived blood flow and blood volume measurements. Stroke 2006;37(7):1771-1777.

30. Bråtane B, Bouley J, Schneider A, Bastan B, Henninger N, Fisher M. Granulocyte-colony stimulating factor delays PWI/DWI mismatch evolution and reduces final infarct volume in permanent-suture and embolic focal cerebral ischemia models in the rat. Stroke 2009;40(9):3102-3106.

31. Cesarman-Maus G, Hajjar KA. Molecular mechanisms of fibrinolysis. Br J Haematol 2005;129(3):307-321.

32. Hacke W, Kaste M, Bluhmki E, et al. Thrombolysis with alteplase 3 to 4.5 hours after acute ischemic stroke. N Engl J Med 2008;359(13):1317-1329.

33. Schellinger P, Thomalla G, Fiehler J, et al. MRI-based and CT-based thrombolytic therapy in acute stroke within and beyond established time windows: an analysis of 1210 patients. Stroke 2007;38(10):2640-2645.

34. del Zoppo G, Mabuchi T. Cerebral microvessel responses to focal ischemia. J Cereb Blood Flow Metab 2003;23(8):879-894.

35. Mori E, del Zoppo G, Chambers J, Copeland B, Arfors K. Inhibition of polymorphonuclear leukocyte adherence suppresses no-reflow after focal cerebral ischemia in baboons. Stroke 1992;23(5):712-718.

36. Henninger N, Sicard K, Schmidt K, Bardutzky J, Fisher M. Comparison of ischemic lesion evolution in embolic versus mechanical middle cerebral artery occlusion in Sprague Dawley rats using diffusion and perfusion imaging. Stroke 2006;37(5):1283-1287.

37. Henninger N, Bratane B, Bastan B, Bouley J, Fisher M. Normobaric hyperoxia and delayed tPA treatment in a rat embolic stroke model. J Cereb Blood Flow Metab 2009;29(1):119-129.

38. Ding G, Jiang Q, Li L, et al. MRI of combination treatment of embolic stroke in rat with rtPA and atorvastatin. J Neurol Sci 2006;246(1-2):139-147.

39. Jiang Q, Zhang RL, Zhang ZG, Ewing JR, Divine GW, Chopp M. Diffusion-, T2-, and Perfusion-Weighted Nuclear Magnetic Resonance Imaging of Middle Cerebral Artery Embolic Stroke and Recombinant Tissue Plasminogen Activator Intervention in the Rat. J Cereb Blood Flow Metab 1998;18(7):758-767.

40. Meng X, Fisher M, Shen Q, Sotak C, Duong T. Characterizing the diffusion/perfusion mismatch in experimental focal cerebral ischemia. Ann Neurol 2004;55(2):207-212.

41. Shen Q, Meng X, Fisher M, Sotak C, Duong T. Pixel-by-pixel spatiotemporal progression of focal ischemia derived using quantitative perfusion and diffusion imaging. J Cereb Blood Flow Metab 2003;23(12):1479-1488.

42. Bardutzky J, Shen Q, Bouley J, Sotak C, Duong T, Fisher M. Perfusion and diffusion imaging in acute focal cerebral ischemia: temporal vs. spatial resolution. Brain Res 2005;1043(1-2):155-162.

43. Carano R, Li F, Irie K, et al. Multispectral analysis of the temporal evolution of cerebral ischemia in the rat brain. J Magn Reson Imaging 2000;12(6):842-858.

44. Li F, Han S, Tatlisumak T, et al. A new method to improve in-bore middle cerebral artery occlusion in rats: demonstration with diffusion- and perfusion-weighted imaging. Stroke 1998;29(8):1715-1719; discussion 1719-1720.

45. Hilger T, Niessen F, Diedenhofen M, Hossmann K, Hoehn M. Magnetic resonance angiography of thromboembolic stroke in rats: indicator of recanalization probability and tissue survival after recombinant tissue plasminogen activator treatment. J Cereb Blood Flow Metab 2002;22(6):652-662.

46. Elliott C. Pulmonary Physiology during Pulmonary Embolism — CHEST. Chest 1992;101(4):1635-1715.

47. Pulmonary Vascular Disease: Saunders: 2006. 368 p.

48. Spiro SG, Jett JR, Albert RK. Comprehensive Respiratory Medicine: C.V. Mosby: 1999. 800 p.

49. Levitzky M. Pulmonary Physiology: Mcgraw-Hill (Tx): 1995. 288 p.

50. Mark Evans A, Ward JP. Hypoxic pulmonary vasoconstriction--invited article. Adv Exp Med Biol 2009;648:351-360.

51. Fishman AP. Hypoxia on the pulmonary circulation. How and where it acts. Circ Res 1976;38(4):221-231.

52. Macnee W. Right heart function in COPD. Semin Respir Crit Care Med 2010;31(3):295-312.

53. Burger CD. Pulmonary hypertension in COPD: a review and consideration of the role of arterial vasodilators. COPD 2009;6(2):137-144.

54. Weitzenblum E, Chaouat A, Canuet M, Kessler R. Pulmonary hypertension in chronic obstructive pulmonary disease and interstitial lung diseases. Semin Respir Crit Care Med 2009;30(4):458-470.

55. Karzai W, Haberstroh J, Priebe HJ. Effects of desflurane and propofol on arterial oxygenation during one-lung ventilation in the pig. Acta Anaesthesiol Scand 1998;42(6):648-652.

56. Kellow NH, Scott AD, White SA, Feneck RO. Comparison of the effects of propofol and isoflurane anaesthesia on right ventricular function and shunt fraction during thoracic surgery. Br J Anaesth 1995;75(5):578-582.

57. Naeije R, Brimioulle S. Physiology in medicine: importance of hypoxic pulmonary vasoconstriction in maintaining arterial oxygenation during acute respiratory failure. Critical Care 2001;5(2):67 - 71.

58. Weir EK, Archer SL. The mechanism of acute hypoxic pulmonary vasoconstriction: the tale of two channels. FASEB J 1995;9(2):183-189.

59. Stelzner T, O'Brien R, Sato K, Weil J. Hypoxia-induced increases in pulmonary transvascular protein escape in rats. Modulation by glucocorticoids. J Clin Invest 1988;82(6):1840-1847.

60. Ochoa CD, Yu L, Al-Ansari E, Hales CA, Quinn DA. Thrombospondin-1 null mice are resistant to hypoxia-induced pulmonary hypertension. J Cardiothorac Surg 2010;5:32.

61. Voelkel NF, Tuder RM. Hypoxia-induced pulmonary vascular remodeling: a model for what human disease? J Clin Invest 2000;106(6):733-738.

62. Zwissler B, Welte M, Messmer K. Effects of inhaled prostacyclin as compared with inhaled nitric oxide on right ventricular performance in hypoxic pulmonary vasoconstriction. J Cardiothorac Vasc Anesth 1995;9(3):283-289.

63. Srivastava S, Eagleton M, Greenfield L. Diagnosis of pulmonary embolism with various imaging modalities. Semin Vasc Surg 2004;17(2):173-180.

64. Kostadima E, Zakynthinos E. Pulmonary embolism: pathophysiology, diagnosis, treatment. Hellenic J Cardiol 2007;48(2):94-107.

65. Watts J, Gellar M, Obraztsova M, Kline J, Zagorski J. Role of inflammation in right ventricular damage and repair following experimental pulmonary embolism in rats. Int J Exp Pathol 2008;89(5):389-399.

66. Watts JA, Gellar MA, Stuart LK, Obraztsova M, Kline JA. Proinflammatory events in right ventricular damage during pulmonary embolism: effects of treatment with ketorolac in rats. J Cardiovasc Pharmacol 2009;54(3):246-252.

67. Young T, Tang H, Hughes R. Vena caval filters for the prevention of pulmonary embolism. Cochrane Database Syst Rev 2010;2:CD006212.

68. Lankeit M, Konstantinides S. Thrombolysis for pulmonary embolism: Past, present and future. Thromb Haemost 2010;103(5):877-883.

69. Liu S, Shi HB, Gu JP, et al. Massive Pulmonary Embolism: Treatment with the Rotarex Thrombectomy System. Cardiovasc Intervent Radiol 2010.

70. Stein PD, Matta F. Acute Pulmonary Embolism. Curr Probl Cardiol 2010;35(7):314-376.

71. Estrada YMRM, Oldham SA. CTPA as the gold standard for the diagnosis of pulmonary embolism. Int J Comput Assist Radiol Surg 2010.

72. Ohno Y, Koyama H, Matsumoto K, et al. Dynamic MR perfusion imaging: capability for quantitative assessment of disease extent and prediction of outcome for patients with acute pulmonary thromboembolism. J Magn Reson Imaging 2010;31(5):1081-1090.

73. Groth M, Henes FO, Bannas P, Muellerleile K, Adam G, Regier M. Intraindividual Comparison of Contrast-Enhanced MRI and Unenhanced SSFP Sequences of Stenotic and Non-stenotic Pulmonary Artery Diameters. Rofo 2010.

74. Metscher B. MicroCT for comparative morphology: simple staining methods allow high-contrast 3D imaging of diverse non-mineralized animal tissues. BMC Physiology 2009;9(1):11.

75. Badea CT, Johnston SM, Subashi E, Qi Y, Hedlund LW, Johnson GA. Lung perfusion imaging in small animals using 4D micro-CT at heartbeat temporal resolution. Med Phys 2010;37(1):54-62.

76. Wietholt C. SPECT Imaging of Pulmonary Blood Flow in a Rat. Volume 5031. Medical Imaging 2003: SPIE; 2003. p. 252-261.

77. Wietholt C, Roerig DL, Gordon JB, Haworth ST, Molthen RC, Clough AV. Bronchial circulation angiogenesis in the rat quantified with SPECT and micro-CT. Eur J Nucl Med Mol Imaging 2008;35(6):1124-1132.

78. Bergin CJ, Glover GM, Pauly J. Magnetic resonance imaging of lung parenchyma. J Thorac Imaging 1993;8(1):12-17.

79. Crémillieux Y, Berthezène Y, Humblot H, et al. A combined 1H perfusion/3He ventilation NMR study in rat lungs. Magn Reson Med 1999;41(4):645-648.

80. Berthezene Y, Vexler V, Clement O, Muhler A, Moseley ME, Brasch RC. Contrast-enhanced MR imaging of the lung: assessments of ventilation and perfusion. Radiology 1992;183(3):667-672.

81. Mistry NN, Qi Y, Hedlund LW, Johnson GA. Ventilation/perfusion imaging in a rat model of airway obstruction. Magn Reson Med 2010;63(3):728-735.

82. Mistry NN, Pollaro J, Song J, De Lin M, Johnson GA. Pulmonary perfusion imaging in the rodent lung using dynamic contrast-enhanced MRI. Magn Reson Med 2008;59(2):289-297.

83. Yu J, Rajaei S, Ishii M, et al. Measurement of pulmonary partial pressure of oxygen and oxygen depletion rate with hyperpolarized helium-3 MRI: a preliminary reproducibility study on pig model. Acad Radiol 2008;15(6):702-712.

84. Cieslar K, Alsaid H, Stupar V, et al. Measurement of nonlinear pO2 decay in mouse lungs using 3He-MRI. NMR Biomed 2007;20(3):383-391.

85. Dimitrov IE, Insko E, Rizi R, Leigh JS. Indirect detection of lung perfusion using susceptibility-based hyperpolarized gas imaging. J Magn Reson Imaging 2005;21(2):149-155.

86. Viallon M, Berthezene Y, Decorps M, et al. Laser-polarized (3)He as a probe for dynamic regional measurements of lung perfusion and ventilation using magnetic resonance imaging. Magn Reson Med 2000;44(1):1-4.

87. Gast K, Schreiber W, Herweling A, et al. Two-dimensional and three-dimensional oxygen mapping by 3He-MRI validation in a lung phantom. Eur Radiol 2005;15(9):1915-1922.

88. Rizi RR, Baumgardner JE, Ishii M, et al. Determination of regional VA/Q by hyperpolarized 3He MRI. Magn Reson Med 2004;52(1):65-72.

89. Bardutzky J, Shen Q, Henninger N, Schwab S, Duong T, Fisher M. Characterizing tissue fate after transient cerebral ischemia of varying duration using quantitative diffusion and perfusion imaging. Stroke 2007;38(4):1336-1344.

90. Fisher M. The ischemic penumbra: a new opportunity for neuroprotection. Cerebrovasc Dis 2006;21 Suppl 2:64-70.

91. Schlaug G, Benfield A, Baird A, et al. The ischemic penumbra: operationally defined by diffusion and perfusion MRI. Neurology 1999;53(7):1528-1537.

92. Gall P, Mader I, Kiselev V. Extraction of the first bolus passage in dynamic susceptibility contrast perfusion measurements. MAGMA 2009.

93. Hofmeijer J, Schepers J, van der Worp HB, Kappelle LJ, Nicolay K. Comparison of perfusion MRI by flow-sensitive alternating inversion recovery and dynamic susceptibility contrast in rats with permanent middle cerebral artery occlusion. Nmr in Biomedicine 2005;18(6):390-394.

94. Williams D, Grandis D, Zhang W, Koretsky A. Magnetic resonance imaging of perfusion in the isolated rat heart using spin inversion of arterial water. Magn Reson Med 1993;30(3):361-365.

95. Koizumi J, Yoshida Y, Nakazawa T, Ooneda G. Experimental studies of ischemic brain edema. 1. A new experimental model of cerebral embolism in rats in which recirculation can be introduced in the ischemic area. Japanese Journal of Stroke 1986;8:1-0.

96. Laurent S, Elst L, Muller R. Comparative study of the physicochemical properties of six clinical low molecular weight gadolinium contrast agents. Contrast Media Mol Imaging 2006;1(3):128-137.

97. Corot C, Port M, Raynal I, et al. Physical, chemical, and biological evaluations of P760: a new gadolinium complex characterized by a low rate of interstitial diffusion. J Magn Reson Imaging 2000;11(2):182-191.

98. Berlex. Magnevist package insert (Berlex—US), Rev 8/89. 2005.

99. Madsen M. A SIMPLIFIED FORMULATION OF THE GAMMA VARIATE FUNCTION. PHYSICS IN MEDICINE AND BIOLOGY 1992;37(7):1597-1600.

100. Bardutzky J, Shen Q, Henninger N, Bouley J, Duong T, Fisher M. Differences in ischemic lesion evolution in different rat strains using diffusion and perfusion imaging. Stroke 2005;36(9):2000-2005.

101. Carroll T, Teneggi V, Jobin M, et al. Absolute quantification of cerebral blood flow with magnetic resonance, reproducibility of the method, and comparison with H2(15)O positron emission tomography. J Cereb Blood Flow Metab 2002;22(9):1149-1156.

102. Keston P, Murray A, Jackson A. Cerebral perfusion imaging using contrast-enhanced MRI. Clin Radiol 2003;58(7):505-513.

103. Cheong L, Koh T, Hou Z. An automatic approach for estimating bolus arrival time in dynamic contrast MRI using piecewise continuous regression models. PHYSICS IN MEDICINE AND BIOLOGY 2003;48(5):N83-N88.

104. Schepers J, Veldhuis W, Pauw R, et al. Comparison of FAIR perfusion kinetics with DSC-MRI and functional histology in a model of transient ischemia. Magn Reson Med 2004;51(2):312-320.

105. Zhu H, Fan X, Yu Z, et al. Annexin A2 combined with low-dose tPA improves thrombolytic therapy in a rat model of focal embolic stroke. J Cereb Blood Flow Metab 2010;30(6):1137-1146.

106. Fujiwara N, Murata Y, Arai K, et al. Combination therapy with normobaric oxygen (NBO) plus thrombolysis in experimental ischemic stroke. BMC Neurosci 2009;10:79.

107. Reese T, Bochelen D, Sauter A, Beckmann N, Rudin M. Magnetic resonance angiography of the rat cerebrovascular system without the use of contrast agents. NMR Biomed 1999;12(4):189-196.

108. Gralla J, Schroth G, Remonda L, et al. A dedicated animal model for mechanical thrombectomy in acute stroke. AJNR Am J Neuroradiol 2006;27(6):1357-1361.

109. Morris T, Marsh J, Chiles P, et al. Single photon emission computed tomography of pulmonary emboli and venous thrombi using anti-D-dimer. Am J Respir Crit Care Med 2004;169(9):987-993.

110. Spuentrup E, Botnar R, Wiethoff A, et al. MR imaging of thrombi using EP-2104R, a fibrin-specific contrast agent: initial results in patients. Eur Radiol 2008;18(9):1995-2005.

111. Prasad S, Kashyap R, Deopujari J, Purohit H, Taori G, Daginawala H. Development of an in vitro model to study clot lysis activity of thrombolytic drugs. Thromb J 2006;4:14.

112. Henninger N, Bouley J, Bråtane B, Bastan B, Shea M, Fisher M. Laser Doppler flowmetry predicts occlusion but not tPA-mediated reperfusion success after rat embolic stroke. Exp Neurol 2009;215(2):290-297.

113. Ishii H, Yoshida M, Hiraoka M, et al. Recombinant annexin II modulates impaired fibrinolytic activity in vitro and in rat carotid artery. Circ Res 2001;89(12):1240-1245.

114. Schmidt K, Ziu M, Schmidt N, et al. Volume reconstruction techniques improve the correlation between histological and in vivo tumor volume measurements in mouse models of human gliomas. J Neurooncol 2004;68(3):207-215.

115. Tanaka Y, Ishii H, Hiraoka M, et al. Efficacy of recombinant annexin 2 for fibrinolytic therapy in a rat embolic stroke model: a magnetic resonance imaging study. Brain Res 2007;1165:135-143.

116. Liu S, Connor J, Peterson S, Shuttleworth C, Liu K. Direct visualization of trapped erythrocytes in rat brain after focal ischemia and reperfusion. J Cereb Blood Flow Metab 2002;22(10):1222-1230.

117. Kim J, Hajjar KA. Annexin II: a plasminogen-plasminogen activator co-receptor. Front Biosci 2002;7:d341-348.

118. Hajjar KA, Menell JS. Annexin II: a novel mediator of cell surface plasmin generation. Ann N Y Acad Sci 1997;811:337-349.

119. Hajjar KA, Acharya SS. Annexin II and regulation of cell surface fibrinolysis. Ann N Y Acad Sci 2000;902:265-271.

120. Hajjar KA, Krishnan S. Annexin II: a mediator of the plasmin/plasminogen activator system. Trends Cardiovasc Med 1999;9(5):128-138.

121. Sakharov DV, Rijken DC. Superficial accumulation of plasminogen during plasma clot lysis. Circulation 1995;92(7):1883-1890.

122. Zagorski J, Gellar M, Obraztsova M, Kline J, Watts J. Inhibition of CINC-1 decreases right ventricular damage caused by experimental pulmonary embolism in rats. J Immunol 2007;179(11):7820-7826.

123. Souza-Costa D, Figueiredo-Lopes L, Alves-Filho J, et al. Protective effects of atorvastatin in rat models of acute pulmonary embolism: involvement of matrix metalloproteinase-9. Crit Care Med 2007;35(1):239-245.

124. Deninger A, Eberle B, Bermuth J, et al. Assessment of a single-acquisition imaging sequence for oxygen-sensitive (3)He-MRI. Magn Reson Med 2002;47(1):105-114.

125. Fischer M, Spector Z, Ishii M, et al. Single-acquisition sequence for the measurement of oxygen partial pressure by hyperpolarized gas MRI. Magn Reson Med 2004;52(4):766-773.

126. Deninger AJ, Eberle B, Bermuth J, et al. Assessment of a single-acquisition imaging sequence for oxygen-sensitive (3)He-MRI. Magn Reson Med 2002;47(1):105-114.

127. Saam B, Happer W, Middleton H. Nuclear relaxation of 3He in the presence of O2. Phys Rev A 1995;52(1):862-865.

128. Watts JA, Marchick MR, Kline JA. Right ventricular heart failure from pulmonary embolism: key distinctions from chronic pulmonary hypertension. J Card Fail 2010;16(3):250-259.

129. Khimenko P, Barnard J, Moore T, Wilson P, Ballard S, Taylor A. Vascular permeability and epithelial transport effects on lung edema formation in ischemia and reperfusion. J Appl Physiol 1994;77(3):1116-1121.

130. Chance W, Rhee C, Yilmaz C, et al. Diminished alveolar microvascular reserves in type 2 diabetes reflect systemic microangiopathy. Diabetes Care 2008;31(8):1596-1601.

131. López-Herce J, Rupérez M, Sánchez C, García C, García E. Haemodynamic response to acute hypovolaemia, rapid blood volume expansion and adrenaline administration in an infant animal model. Resuscitation 2006;68(2):259-265.

132. Oppenheimer B, Berger K, Hadjiangelis N, Norman R, Rapoport D, Goldring R. Membrane diffusion in diseases of the pulmonary vasculature. Respir Med 2006;100(7):1247-1253.

133. Zhang L, Yang G, Zhao Y, Zhou C, Lu G. Detection of pulmonary embolism using dual-energy computed tomography and correlation with cardiovascular measurements: a preliminary study. Acta Radiol 2009;50(8):892-901.

134. Kim Y, Tejima E, Huang S, et al. In vivo quantification of transvascular water exchange during the acute phase of permanent stroke. Magn Reson Med 2008;60(4):813-821.

135. Kim Y, Rebro K, Schmainda K. Water exchange and inflow affect the accuracy of T1-GRE blood volume measurements: implications for the evaluation of tumor angiogenesis. Magn Reson Med 2002;47(6):1110-1120.

136. Raman V, Artemov D, Pathak AP, et al. Characterizing vascular parameters in hypoxic regions: a combined magnetic resonance and optical imaging study of a human prostate cancer model. Cancer Res 2006;66(20):9929-9936.

137. Hatabu H, Gaa J, Tadamura E, et al. MR imaging of pulmonary parenchyma with a half-Fourier single-shot turbo spin-echo (HASTE) sequence. Eur J Radiol 1999;29(2):152-159.

138. Donahue K, Weisskoff R, Chesler D, et al. Improving MR quantification of regional blood volume with intravascular T1 contrast agents: accuracy, precision, and water exchange. Magn Reson Med 1996;36(6):858-867.

139. Hazlewood C, Nichols B, Chang D, Brown B. On the state of water in developing muscle: a study of the major phase of ordered water in skeletal muscle and its relationship to sodium concentration. Johns Hopkins Med J 1971;128(3):117-131.

140. Tabuchi A, Mertens M, Kuppe H, Pries A, Kuebler W. Intravital microscopy of the murine pulmonary microcirculation. J Appl Physiol 2008;104(2):338-346.

141. Fallon M, Abrams G, Abdel-Razek T, et al. Garlic prevents hypoxic pulmonary hypertension in rats. Am J Physiol 1998;275(2 Pt 1):L283-287.

142. Burri P. Postnatal growth and maturation of the lung. Chest 1975;67(2 Suppl):2S-3S.

143. Plopper C, Dungworth D, Tyler W. Morphometric evaluation of pulmonary lesions in rats exposed to ozone. Am J Pathol 1973;71(3):395-408.

144. Ohno Y, Hatabu H. Basics concepts and clinical applications of oxygen-enhanced MR imaging. Eur J Radiol 2007;64(3):320-328.

145. Galvin J, Franks T. Smoking-related lung disease. J Thorac Imaging 2009;24(4):274-284.

146. Hansch A, Betge S, Poehlmann G, et al. Combined magnetic resonance imaging of deep venous thrombosis and pulmonary arteries after a single injection of a blood pool contrast agent. Eur Radiol 2010.

147. Calamante F, Christensen S, Desmond P, Ostergaard L, Davis S, Connelly A. The physiological significance of the time-to-maximum (Tmax) parameter in perfusion MRI. Stroke 2010;41(6):1169-1174.

148. Zafar M, Ibáñez B, Choi B, et al. A new oral antiplatelet agent with potent antithrombotic properties: comparison of DZ-697b with clopidogrel a randomised phase I study. Thromb Haemost 2010;103(1):205-212.

149. Shibata K, Hashimoto T, Nobe K, Hasumi K, Honda K. A novel finding of a low-molecular-weight compound, SMTP-7, having thrombolytic and anti-inflammatory effects in cerebral infarction of mice. Naunyn Schmiedebergs Arch Pharmacol 2010.

Appendix I

Physiological Data from Experiments Conducted in Chapter II

	Permanent Model-Baseline	Permanent Model- Four Hours Post Stroke	Transient Model-Baseline	Transient Model- Four Hours Post Stroke
Mean Arterial Blood Pressure (mmHg)	No Data (Blood Chemistry Only)	108.33±11.25	No Data (Blood Chemistry Only)	103.33±9.83
pH	7.46±0.04	7.43±0.02	7.43±0.04	7.41±0.03
pCO_2 (mmHg)	36.50±5.02	37.14±2.00	42.24±6.13	40.23±7.86
PO_2 (mmHg)	61.22±6.26	73.86±9.25	66.50±10.10	62.67±12.58
BE ecf	2.25±3.06	0.00±2.45	2.90±1.85	0.83±2.40
HCO_3 (mmol/L)	26.33±2.98	24.70±2.11	27.37±2.07	24.30±4.88
TCO_2 (mmol/L)	27.22±2.86	25.71±2.14	28.80±2.25	26.17±5.27
sO_2 (%)	92.00±2.78	94.57±2.23	92.50±3.03	90.50±4.42
Na (mmol/L)	135.75±2.87	136.17±1.17	137.30±2.11	142.17±5.12
K (mmol/L)	4.48±0.30	4.27±0.22	4.05±0.37	3.97±0.75
iCa (mmol/L)	1.30±0.08	1.31±0.02	1.31±0.07	1.22±0.13
Glu (mg/dL)	201.00±24.07	179.00±14.86	208.90±71.19	176.83±60.66
Hct (%Packed Cell Volume)	38.63±2.62	40.50±1.52	38.40±2.88	35.67±3.78
Hb (g/dL)	13.11±0.89	13.77±0.53	13.05±0.97	11.88±1.92

pCO_2:partial pressure of CO_2, pO_2: partial pressure of oxygen, BE ecf: base excess of the extra cellular fluid (mmol/L), HCO_3:bicarbonate, TCO_2: total carbon dioxide content, sO_2: oxygen saturation, Na: sodium, K: potassium, iCa: ionized calcium, Glu: glucose, Hct: hematocrit,Hb: hemoglobin

Appendix II

Physiological Data from Experiments Conducted in Chapter III Prior to Stroke

	Saline	tPA	tPA+rA2
Mean Arterial Blood Pressure (mmHg)	No Data (Blood Chemistry Only)	No Data (Blood Chemistry Only)	No Data (Blood Chemistry Only)
pH	7.43±.02	7.43±.03	7.42±.03
pCO_2 (mmHg)	46.06±3.03	44.66±4.64	45.70±4.10
PO_2 (mmHg)	64.33±7.66	69.20±7.40	66.0±7.54
BE ecf	6.40±1.67	5.20±1.79	5.00±1.26
HCO_3 (mmol/L)	30.56±1.62	29.56±1.98	29.55±1.33
TCO_2 (mmol/L)	32.00±1.58	31.00±1.87	31.00±1.41
sO_2 (%)	91.80±3.42	93.60±2.30	92.50±2.51
Na (mmol/L)	135.67±1.51	135.20±2.28	135.83±1.83
K (mmol/L)	4.45±.39	4.72±.31	4.38±.31
iCa (mmol/L)	1.35±.04	1.33±.03	1.34±.03
Glu (mg/dL)	274.33±53.25	240.80±40.54	272.33±67.19
Hct (%Packed Cell Volume)	39.17±1.33	37.60±1.67	38.67±1.03
Hb (g/dL)	13.30±0.45	12.80±.58	13.17±.36

pCO_2:partial pressure of CO_2, pO_2: partial pressure of oxygen, BE ecf: base excess of the extra cellular fluid (mmol/L), HCO_3:bicarbonate, TCO_2: total carbon dioxide content, sO_2: oxygen saturation, Na: sodium, K: potassium, iCa: ionized calcium, Glu: glucose, Hct: hematocrit,Hb: hemoglobin

Physiological Data from Experiments Conducted in Chapter III Following Treatment

	Saline	tPA	tPA+rA2
Mean Arterial Blood Pressure (mmHg)	101.11±4.082	100.00±7.07	98.333±4.08
pH	7.33±.10	7.34±.05	7.32±.05
pCO_2 (mmHg)	53.45±12.15	52.96±6.43	51.12±7.50
PO_2 (mmHg)	48.83±6.59	42.20±9.01	56.67±14.08
BE ecf	2.00±3.35	2.60±1.14	-0.17±1.16
HCO_3 (mmol/L)	27.83±2.37	28.44±1.04	25.87±1.06
TCO_2 (mmol/L)	29.67±2.34	29.80±1.10	27.33±1.37
sO_2 (%)	78.67±11.78	71.60±12.50	83.00±10.81
Na (mmol/L)	137.17±2.32	136.20±2.17	140.00±1.41
K (mmol/L)	4.80±.60	5.40±.48	4.15±.23
iCa (mmol/L)	1.35±.04	1.24±.06	1.16±.04
Glu (mg/dL)	287.67±132.66	249.40±81.17	238.00±38.69
Hct (%Packed Cell Volume)	37.00±1.41	37.60±1.14	37.83±1.94
Hb (g/dL)	12.58±.50	12.78±.41	12.87±.68

pCO_2:partial pressure of CO_2, pO_2: partial pressure of oxygen, BE ecf: base excess of the extra cellular fluid (mmol/L), HCO_3:bicarbonate, TCO_2: total carbon dioxide content, sO_2: oxygen saturation, Na: sodium, K: potassium, iCa: ionized calcium, Glu: glucose, Hct: hematocrit, Hb: hemoglobin